CONSTRAINED LEAST-SQUARES SPECTRAL ANALYSIS:

APPLICATION TO SEISMIC DATA

A Dissertation

Presented to

the Faculty of the Department of Earth and Atmospheric Sciences

University of Houston

In Partial Fulfillment

of the Requirements for the Degree

Doctor of Philosophy

By

Charles Ian Cecil Puryear

May, 2012

Constrained Least Squares Spectral Analysis: Application to Seismic Data

_____

Charles Ian Cecil Puryear

APPROVED:

_____

Dr. John Castagna, Chairman

_____

Dr. Oleg Portniaguine

_____

Dr. Robert Stewart

_____

Dr. Aibing Li

_____

Dean, College of Natural Sciences and Mathematics

ACKNOWLEDGEMENTS

My sincerest thanks go to my advisor Dr. John Castagna for sharing his expertise in spectral analysis, for guidance and for encouragement. I thank Dr. Oleg Portniaguine for teaching me inverse theory and computational science. I thank Dr. Robert Stewart and Dr. Aibing Li for their very helpful suggestions in further refining the manuscript and testing the method. My special appreciation goes to Dr. John Casey for his advice and assistance in the successful completion of my studies. Thanks to ExxonMobil and Marathon for the use of 3D seismic data donated to the University of Houston. Last, but not least, thanks to my family for support in achieving this milestone.

CONSTRAINED LEAST-SQUARES SPECTRAL ANALYSIS:
APPLICATION TO SEISMIC DATA

An Abstract of a Dissertation

Presented to

the Faculty of the Department of Earth and Atmospheric Sciences

University of Houston

In Partial Fulfillment

of the Requirements for the Degree

Doctor of Philosophy

By

Charles Ian Cecil Puryear

May, 2012

ABSTRACT

This dissertation describes a new method called Constrained Least-Squares Spectral Analysis (CLSSA), an inversion-based algorithm for computing the time-frequency analysis of reflection seismograms. CLSSA is formulated and applied to modeled seismic waveforms and real seismic data. The Fourier Series coefficients are computed as a function of time directly by inverting a basis of truncated sinusoidal kernels for a moving time window. The method results in spectra that have reduced window smearing for a given window length relative to the Discrete Fourier Transform irrespective of window shape, and a time-frequency analysis with a combination of time and frequency resolution that is superior to both the Short-time Fourier Transform and the Continuous Wavelet Transform. The reduction in spectral smoothing enables better determination of the spectral characteristics of interfering reflections within a short window. The degree of resolution improvement relative to the Short-time Fourier Transform increases as window length decreases. As compared to the Continuous Wavelet Transform, the method has greatly improved temporal resolution, particularly at low frequencies.

TABLE OF CONTENTS

1. INTRODUCTION

1.1. Motivation for spectral analysis

Seismic spectral decomposition (e.g., Partyka, et al., 1999) transforms each reflection seismogram into a time-frequency space that represents localized frequency content as a function of seismic record time. Thus, individual seismic volumes are transformed into multiple frequency volumes that preferentially highlight geophysical responses that appear within particular frequency bands. Commonly used spectral decomposition methods, such as the Fourier Transform and the Continuous Wavelet Transform generally require a tradeoff between time and frequency resolution that may render them ineffective in particular cases for certain interpretation applications, such as layer thickness determination and direct hydrocarbon detection. The objective of this paper is to introduce and evaluate the effectiveness of Constrained Least Squares Spectral Analysis (CLSSA) as a seismic spectral decomposition method and show that it has resolution advantages over the conventional approaches.

Fourier-based spectral decomposition uses a sliding temporal window, which limits both temporal and frequency resolutions. In spectral analysis of seismic events that are near in time to other arrivals, it is often necessary to sacrifice frequency resolution by using a short time window to isolate the event of interest. Figure 1 illustrates this fundamental problem in spectral decomposition: a pair of reflection coefficients from the top and base of a thin layer is bracketed by nearby strong reflection coefficients. When convolved with a wavelet, the reflection event from the

thin layer has interference at its fringes with side-lobes from the bracketing reflections. The correct spectral response for the thin layer (a cosine function times the Ricker spectrum) should have a notch at 50 Hz corresponding to the first spectral notch of the even impulse pair. As emphasized by Partyka (1999), the frequency at which this notch occurs could be used to determine the layer time thickness, which is of great potential utility for pre-drill estimates of reservoir volumetrics. In order to make use of the notch occurrence, the window chosen for spectral analysis must be short enough to avoid interference with nearby reflectors, but long enough so that the window smearing effect on the spectrum does not change the notch location. Unfortunately, as illustrated in Figure 1, this may not be achievable in practice. A Hann window short enough to avoid interference (40 ms in this case) results in a Fourier spectrum that is dominated by the window spectrum, and the notch and peak frequencies do not directly reflect the layer characteristics – which would thereby yield an incorrect reservoir thickness estimate. Longer windows yield spectral estimates that are corrupted by the interfering energy, and again yield misleading spectral notch frequencies that would result in incorrect thickness estimates. In such a situation, it would be advantageous to be able to use a short window without the corresponding loss of frequency resolution inherent in the use of the Fourier Transform.

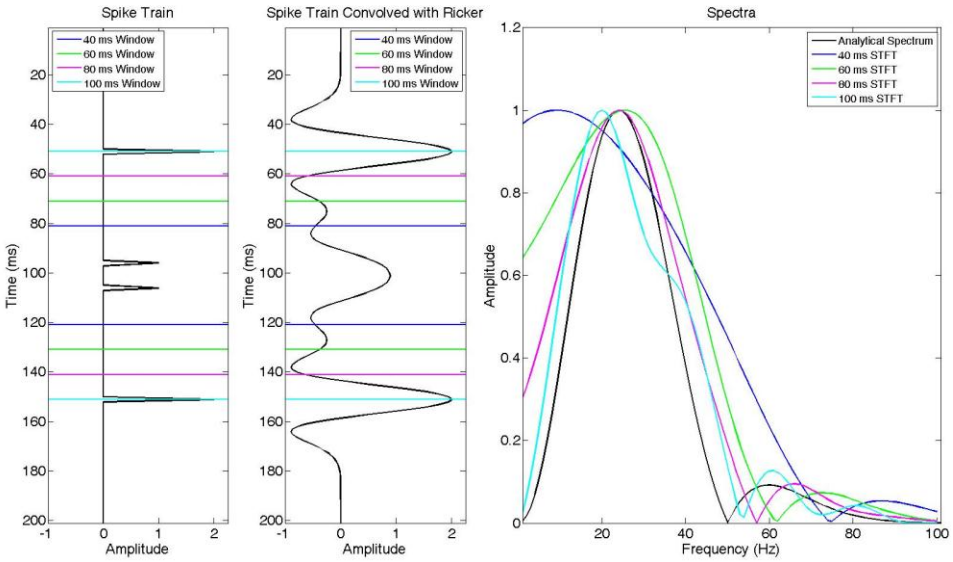

Figure 1). Windowed spectral analysis of an even reflection coefficient pair contained within a thicker even reflection coefficient pair. Horizontal lines represent windows of different lengths used to compute the spectra. Plots show (a) an even reflection coefficient pair (10 ms thick) within a series of Hann window limits with a thicker even reflection coefficient pair (100 ms thick) falling just at the limits of the longest DFT window, (b) the convolution of the reflectivity series with a 30 Hz Ricker wavelet, and (c) the Fourier Transform computed using the series of Hann windows and the analytical spectrum (black).

Short windows are desirable for the temporal isolation of particular portions of seismic traces in order to obtain spectra and spectral attributes (such as peak frequency and amplitude at peak frequency) that are relevant to the characteristics of a given layer. However, the Fourier Similarity Theorem (e.g., Bracewell, 1986) requires that shorter windows of a given shape have poorer frequency resolution which can mask and modify spectral characteristics. Using a given window shape, better frequency resolution can only be achieved with the Fourier Transform at the expense of poorer

time resolution by increasing the window length. Reducing the window effect in seismic time-frequency analysis is, thus, of great potential practical significance.

One approach towards reducing the window effect is to circumvent the Fourier Transform, and solve directly for the Fourier Series coefficients using least-squares analysis within a window (Vaníček, 1969). The Fourier Transform is indeed the least-squares solution for the Fourier Series coefficients, only when the sinusoidal basis functions are orthogonal. When seismic data are windowed, this definition is violated for those frequencies for which the window length is not an integer number of periods. The well-known consequence is smearing of the data spectrum computed with the Fourier Transform by the window transfer function. However, this effect is a result of the definition of the Fourier Transform requiring that the sinusoidal bases are uncorrelated, not a necessary consequence of Fourier Analysis (which is the determination of the Fourier Series coefficients). The Fourier Transform is only one of many possible means of solving for those coefficients. From the point of view of determining the Fourier Series coefficients of a time series within a window, the window smearing effect arises from what can be considered the implicit requirement of the windowed Fourier Transform that the sinusoidal bases are orthogonal over the window length. This results in the Fourier Transform yielding the spectrum of the windowed data rather than the spectrum of the data within the window. Seismic time-frequency analysis by direct solution of the normal equations for the Fourier Series coefficients when the sinusoidal bases are not orthogonal has, perhaps surprisingly, not been

reported upon in the seismic spectral decomposition literature. Such an approach is complicated by the fact that the inversion for these coefficients is non-unique, and constraints are thus required.

We refer to the application of constraints to the solution of the normal equations for the Fourier Series coefficients as Constrained Least-Squares Spectral Analysis (CLSSA). We can expect the results of CLSSA to be very dependent on the constraints applied, the assumptions made, and the parameters chosen. Nevertheless, as time-frequency analysis is generally non-unique, this should not deter us from investigating the potential benefits of such a method.

For our purpose of investigating possible improvements in seismic spectral decomposition that will allow the use of shorter windows than are practicable with the ordinary Fourier Transform, we formulate and apply an algorithm that applies model and data constraints in a particular manner using well known numerical methods that have been commonly used for other applications. Use of other algorithms and other constraints to invert the normal equations are certainly feasible. Our objective is only to show the potential value of the general CLSSA approach for time-frequency analysis of reflection seismograms. In particular, we will assess the temporal and frequency resolution that can be achieved with our CLSSA algorithm, and compare results to the Short-Time Fourier Transform (STFT) and the Continuous Wavelet Transform (CWT) for synthetic and real seismic data, as these are presently the two most commonly used spectral decomposition methods in exploration geophysics practice.

1.2 Historical background

Spectral decomposition of reflection seismograms was introduced as a seismic interpretation technique by Partyka (1999). He recognized that seismic frequency spectra using short windows were greatly affected by local reflectivity spectra, and thus carried information about layer characteristics. He showed that simple layers of certain thicknesses exhibit notched spectra, and that the pattern of frequencies at which these notches occur can sometimes be used to infer layer thickness. He also showed that, for this reason, seismic images at different frequencies preferentially illuminate, or respond to, geological variations differently. Spectral time-frequency analysis has since become an important practical seismic interpretation tool that has achieved widespread use.

Early spectral decomposition work primarily used (1) the Short-time Fourier Transform (STFT), which is equivalent to the cross-correlation of the seismic trace with a sinusoidal basis over a moving time window, (2) the Continuous Wavelet Transform (CWT), which is the cross-correlation of the seismic trace against a wavelet dictionary, and (3) Matching Pursuit Decomposition (MPD), which is the decomposition of the seismic trace into basis atoms. The use of these methods for seismic time-frequency analysis is discussed by Chakraborty and Okaya (1995).

The literature is rich in papers discussing geological applications of seismic spectral decomposition, a few of which are mentioned here. The STFT has been successfully applied for stratigraphic and structural visualization (e.g., Partyka, et al., 1999; Marfurt and Kirlin, 2001). Marfurt and Kirlin (2001) derive a suite of attributes,

including peak frequency, from spectral decomposition volumes in order to efficiently map stratigraphic features, particularly fluvial channels. These frequency attributes are further described and applied by Liu and Marfurt (2007). Sinha et al. (2005) apply the CWT for stratigraphic visualization and direct hydrocarbon indication. Matos et al. (2010) compute CWT spectral decomposition phase residues as an attribute for stratigraphic interpretation. Castagna et al. (2003) and Fahmy (2008) use MPD for direct hydrocarbon detection. Partyka (2005) and Puryear and Castagna (2008) [Appendix A] describe the use of spectral decomposition as a driver for thin-layer reflectivity inversion.

Higher resolution seismic spectral decomposition methods would assist in the interpretation of geological features masked by spectral smearing (when the STFT is used) or poor temporal resolution at low frequencies (when the CWT is used). Toward this end, we revisit Fourier theory and then formulate an alternative approach to seismic spectral decomposition using Constrained Least Squares Spectral Analysis, which potentially has advantages over conventional methods such as the STFT and CWT in terms of improved temporal and/or frequency resolution of seismic reflection data.

2. METHODS

2.1. Fourier Transform

The Fourier Transform is the mathematical basis of the STFT used in spectral decomposition. The Fourier Transform projects infinite sinusoidal bases on the signal

and is thus the Least Mean Square Error (LMSE) solution for the Fourier Series coefficients:

$$G(f) = \int_{-\infty}^{+\infty} g(t) e^{-i2\pi ft} dt \quad , \tag{1}$$

where t is time, f is frequency, $g(t)$ is the continuous time signal, and $G(f)$ is the continuous complex spectrum. This simple projection of the bases onto the time series is applicable because the bases are infinite and thus orthogonal. The Fourier Transform spectrum is continuous and aperiodic in time and frequency (i.e. there are no periodic frequency wrapping effects in the limit $dt \rightarrow 0$). In digital applications, however, use of the Discrete Fourier Transform (DFT) assumes discretely sampled and periodic series in both the time and frequency domains.

The DFT is the modification of the Fourier Transform for application to discrete signals. In computing the DFT, the sinusoidal basis functions are orthogonal only when their periods are integer fractions of the period of the fundamental frequency. Such an orthogonal basis comprises the "DFT frequencies" (see Figure 2).

The DFT is defined as follows:

$$G(k\Delta f) = \sum_{n=0}^{N-1} g(n\Delta t) e^{-\frac{2\pi i}{N} k\Delta f n\Delta t} \quad , \quad k = 0, \ldots, N-1, \tag{2}$$

where N is the number of time samples, n is the time sample index, Δt is the time increment, k is the frequency sample index, Δf is the frequency increment, $g(n\Delta t)$ is

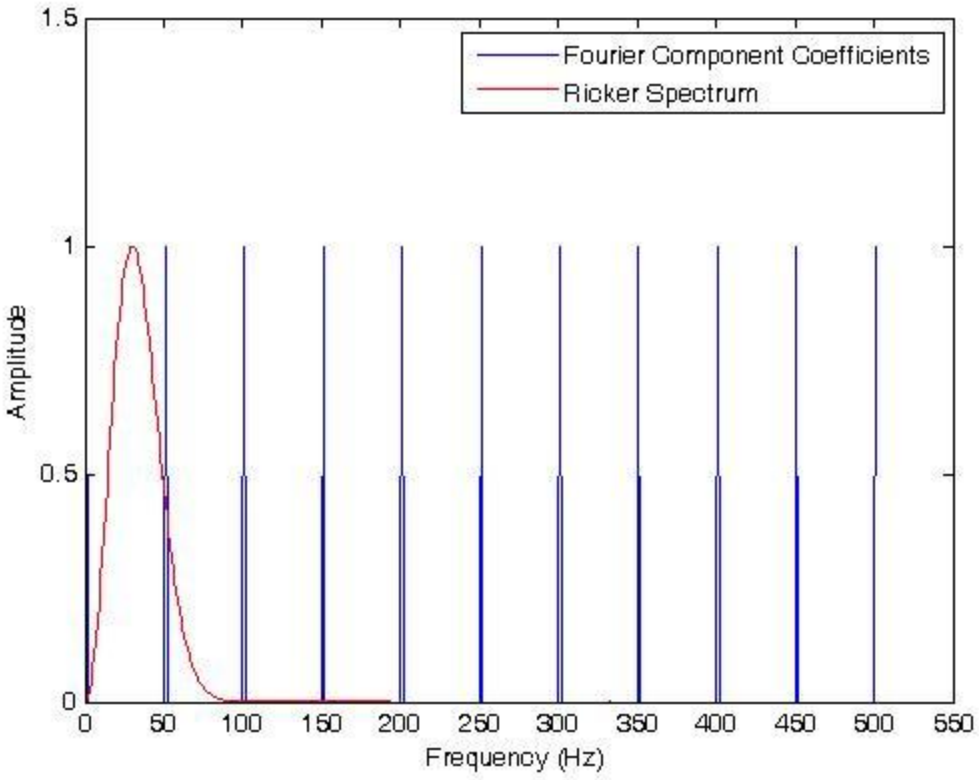

Figure 2). Fourier frequency components for a 20 ms window plotted together with a Ricker wavelet spectrum. df=1/20ms=50 Hz. Signal energy analyzed using the STFT must be projected onto the extremely sparse components that exist within the wavelet band. Clearly, the frequency resolution is not sufficient to produce any meaningful spectral information for this typical seismic band. The need arises to develop a transform that is not limited by the STFT definition.

the discretely-sampled time signal, and $G(k\Delta f)$ is the discretely-sampled complex spectrum.

While the DFT yields integrated information about the entire trace, seismic signals typically contain variations in frequency content as a function of time. In order to capture local anomalies related to stratigraphy, structure, and fluid content, we must apply a time-frequency transform that maximizes time-localization of spectral features.

The STFT is the DFT applied as a function of time using a sliding time window (that is usually tapered to have a desired transfer function). This amounts to cross-correlation of orthogonal sinusoidal basis functions with a windowed segment of the signal. First the time-time panel, g_w, is derived from the windowed signal and expressed as a function of window center and window sample:

$$\begin{gathered} g_w(n\Delta t, m\Delta t) = w(m\Delta t)g((n+m)\Delta t) \\ n = 0,\ldots,N-1 \text{ and } m = -(M-1)/2\ ,...,(M-1)/2\ , \end{gathered} \tag{3}$$

where n is analysis time sample (center of the window), m is the window sample index, M is the number of samples in the window, $w(m\Delta t)$ is the window function (usually tapered towards zero at the endpoints in order to minimize the Gibbs Effect) and $g_w(n\Delta t, m\Delta t)$ is the windowed time-time panel as a function of window position and window sample. Second, the forward STFT is defined as the DFT of a time-time panel over the dimension of the window sample model. This results in a time-frequency panel:

$$G(n\Delta t, k\Delta f) = \sum_{m=-(M-1)/2}^{(M-1)/2} g_w(n\Delta t, m\Delta t)e^{-\frac{2\pi i}{M}k\Delta f m\Delta t}\ . \tag{4}$$

The projection of the infinite sinusoidal bases onto the windowed portion of the time series by the DFT occurs only over the length of the window. This is equivalent to truncating the bases to the window length; the sinusoidal kernels are then no longer generally orthogonal with the exception of those that have an integer number of cycles

within the window length. Thus, the windowed DFT does not give the spectrum of the data within the window but the spectrum of the windowed time series that has data (perhaps tapered) within the window and zeros outside the window. By the Fourier Convolution Theorem, this results in a spectrum that is the convolution of the true spectrum of the data with the spectrum of the window. This spectral smoothing causes a loss of frequency resolution and an increase in the bandwidth of the spectrum. Thus, for real time series, the standard deviation about the mean of the positive frequencies of the spectrum of the windowed data will always be greater than the standard deviation of the positive frequencies of the true spectrum.

When the data are windowed, the sinusoidal uncorrelated bases are spaced at a frequency increment of $df >= 1/T$, where T is the window time length $M\Delta t$. When the orthogonality condition is not met, the DFT can be thought of as "leaking" energy among frequencies. For an extensive treatment of the subject of Fourier Transform windowing and associated spectral leakage, see Bracewell (1986).

However, the reduced frequency resolution of the STFT is not a fundamental limitation of Fourier theory. It is a consequence of the STFT definition (i.e. the use of orthogonal basis functions inside a short time window). For very short windows, the resulting spectrum may bear little resemblance to the spectrum of the data. To compute the spectrum of the data within the window, rather than the spectrum of the windowed data, we must invert the normal equations with non-zero off diagonal terms and, thus, properly solve for the Fourier Series coefficients. We shall see that such proper

application of Fourier theory can significantly increase the resolvability of frequency components, particularly when appropriate constraints are applied.

2.2. Continuous Wavelet Transform

The CWT is a narrowband filter applied to the signal in the time domain using stretched versions of a mother wavelet; it decomposes the seismic data into octave or sub-octave scales of the original data. The CWT is described by Grossman et al. (1989) and Mallat (1999). Chakraborty and Okaya (1995) apply CWT spectral decomposition to seismic data. For seismic applications, the semi-orthogonal Morlet wavelet is commonly preferred. The forward CWT for a real wavelet dictionary is as follows:

$$W_{(a,b)} = \frac{1}{\sqrt{a}} \int \Psi(\frac{t-b}{a}) s(t) dt \,, \tag{5}$$

where a is a scaling parameter, b is a translation parameter, Ψ is the mother wavelet, $s(t)$ is the signal, and $W_{(a,b)}$ is the CWT scale decomposition. As typically applied, the CWT produces scales of the data. A scale corresponds to a more or less narrow frequency band, and one could view the center frequency of these bands as output frequencies. In order to compute frequencies instead of scales, Sinha et al. (2005) define a time-frequency CWT, which is the DFT of the inverse CWT. In this paper, we use the standard CWT process described by equation 5 above, with the frequency axis representing the center frequency of Morlet atoms, as this is a commonly employed method.

CWT solutions suffer from resolution limitations that are similar to the DFT, although CWT resolution varies with scale or frequency; the resulting decomposition has low time resolution/high frequency resolution at low frequencies and high time resolution/low frequency resolution at high frequencies (e.g., Sinha, et al., 2005; Puryear, et al., 2008 [Appendix B]).

2.3. Inversion-based spectral decomposition

Seismic spectral decomposition is a trace-by-trace operation. Because each 1-dimensional seismic trace is converted to a 2-dimensional time-frequency panel, the process expands the dimensions of the original data via a non-unique transformation, suggesting an inversion-based approach to the problem. Several investigators have used different empirical criteria in order to define inversion-based spectral analysis methods.

Vaníček (1969) iteratively finds the best least squares fit coefficients for sines and cosines, subtracts and repeats the process on the residual until the algorithm converges. Oldenburg (1976) uses the first Dirichlet criterion of the Backus-Gilbert linear inverse in order to compute the DFT of potential field data, while minimizing the effects of recording gaps and noise. Sacchi and Ulrych (1996) derive a similar functional using a Bayesian inversion approach to estimate the 2d spectral signature of a limited linear array of receivers. The results show minimal side lobe artifacts, resulting in significant extrapolation of the wavefield aperture beyond the original receiver array. In a method related to the Vaníček method, Xu et al. (2005) derive an algorithm for

reducing leakage of spatial spectra by iteratively solving for and subtracting the most energetic wavenumber components from the signal. This is similar to matching pursuit decomposition with non-orthogonal wavelets, which can be unstable. None of these methods have been applied to time-frequency analysis of reflection seismograms for interpretation of, or inversion for, layer characteristics.

Daubechies et al. (2008) describe the general mathematical convergence of L_p norm functionals, including the minimum support functional, for computationally cumbersome problems. Although Daubechies et al. (2008) do not explicitly apply their method to the problem of time-frequency analysis of signals, we use a similar approach for application to the problem of seismic spectral decomposition. Unlike Daubechies et al. (2008), in the particular implementation we use in this study, we apply Tikhonov regularization to the functional and, because our matrices are not computationally large, solve the problem analytically by Lagrange multipliers as described in the following section.

2.4. CLSSA description

Following the Portniaguine and Castagna (2004) approach to seismic wavelet decomposition and reflectivity inversion, we invert the normal equations by applying an iteratively re-weighted least squares regularization algorithm to the complex spectral decomposition inverse problem using a minimum support functional, which is defined by Last and Kubik (1983) and Portniaguine and Zhdanov (1998). This regularization scheme incorporates *a priori* constraints, differing from post-inversion weighting

schemes that impose constraints on the solution after the inversion process. Prior publications do not describe the application of such a method to direct solution of the normal equations for the Fourier Series coefficients. The following inversion formulation is applied to the data *within each window* centered at a time sample, then looped over each sample of a trace.

We start with the definition of the forward problem:

$$\boldsymbol{Fm} = \boldsymbol{d}\,, \tag{6}$$

where $\boldsymbol{F}$ is the kernel matrix with real or complex sinusoidal basis, $\boldsymbol{m}$ is the model parameter vector (unknown frequency coefficients), and $\boldsymbol{d}$ is the windowed seismic data. For the problem of spectral decomposition of reflection seismograms, the data are real. However, in the CLSSA algorithm we present here, we can take **d** to be a segment of a complex seismic trace,

$$\boldsymbol{d} = \boldsymbol{d}_r + i\boldsymbol{d}_i\,, \tag{6a}$$

where $\boldsymbol{d}_r$ is the windowed segment of the real seismic trace, and $\boldsymbol{d}_i$ is the windowed segment of the Hilbert Transform of the seismic trace. This is not a requirement of the CLSSA approach, but is a way of applying additional constraint to further stabilize the solution for short window lengths. We further define d_0 as the trace sample at the center of the window.

The solution to (6) is achieved using well-known normal equations:

$$\boldsymbol{F}^*\boldsymbol{Fm} = \boldsymbol{F}^*\boldsymbol{d}\,. \tag{7}$$

We choose the columns of matrix ***F*** to consist of complex sinusoidal signals truncated by the endpoints of the window in the time domain:

$$\boldsymbol{F}(t, f) = \cos\left(2\pi k \Delta f m \Delta t\right) + i\sin\left(2\pi k \Delta f m \Delta t\right). \tag{8}$$

The number of columns in ***F*** is the number of frequencies, and the number of rows in ***F*** is the number of samples in the time window. Unless otherwise stated, the complex form of ***F*** is used for the examples in this dissertation (in some examples, only the real part is used). The inverse problem objective is to compute ***m*** given ***F*** and ***d***. The ordinary LMSE solution to equation 6 from the normal equations is

$$\boldsymbol{m} = (\boldsymbol{F}^{*}\boldsymbol{F})^{-1}\boldsymbol{F}^{*}\boldsymbol{d}\,, \tag{9}$$

where * denotes the complex conjugate transpose. When the sinusoids are (or are assumed to be) uncorrelated, $\boldsymbol{F}^{*}\boldsymbol{F} = \boldsymbol{I}$ and (9) reduces to

$$\boldsymbol{m} = \boldsymbol{F}^{*}\boldsymbol{d}\,, \tag{10}$$

which is equivalent to the DFT of the trace segment.

When the data are windowed, however, the elements of ***F*** are generally correlated, and constraints are required to achieve a unique solution. In order to constrain the inversion of equation 6, we introduce diagonal matrices $\boldsymbol{W}_m$ and $\boldsymbol{W}_d$, which are respectively model and data weights. $\boldsymbol{W}_m$ changes iteratively. The initial model weighting matrix on the first iteration is:

$$\boldsymbol{W}_m = I\,, \tag{11}$$

$\boldsymbol{W}_d$ remains constant throughout the iterations. For a Hann taper:

$$\boldsymbol{W}_d = \mathrm{Diag}(0.5 + 0.5\cos(\frac{2\pi n\Delta t}{l}))abs(d_0)\,. \tag{12}$$

where l is window length, $n\Delta t$ is time relative to the window center, $abs(d_0)$ is the data envelope value (instantaneous amplitude) at the center of the window, which scales the sinusoids to the data, and the operator $\mathrm{Diag}()$ transforms a vector to a diagonal matrix containing the argument vector on the main diagonal. Applying $\boldsymbol{W}_d$ and $\boldsymbol{W}_m$ to equation 6, we obtain

$$\boldsymbol{W}_d\boldsymbol{F}\boldsymbol{W}_m(\boldsymbol{W}_m)^{-1}\boldsymbol{m} = \boldsymbol{W}_d\boldsymbol{d}\,. \tag{13}$$

We introduce the weighted quantities

$$\boldsymbol{F}_w = \boldsymbol{W}_d\boldsymbol{F}\boldsymbol{W}_m \text{ and} \tag{14a}$$

$$\boldsymbol{m}_w = \boldsymbol{W}_m^{-1}\boldsymbol{m}; \tag{14b}$$

and recast equation 13 as a model and data weighted ill-posed inverse problem:

$$\boldsymbol{F}_w\boldsymbol{m}_w = \boldsymbol{W}_d\boldsymbol{d}\,. \tag{15}$$

To solve equation 15, we apply Tikhonov regularization, which is similar to the method of Marquardt (1963). Following Tikhonov and Arsenin (1977), we reformulate ill-posed equation 15 by replacing it with a well-posed minimization problem. This is accomplished by defining the Tikhonov parametric functional in the space of weighted model parameters (Portniaguine and Zhdanov, 1998):

$$\left\|\boldsymbol{F}_w\boldsymbol{m}_w - \boldsymbol{W}_d\boldsymbol{d}\right\|^2 + \alpha\left\|\boldsymbol{m}_w\right\|^2 = \min\,, \tag{16}$$

where α is a regularization parameter that can be varied to control the sparsity and stability of the solution. We set α to a fraction of the maximum value along the diagonal of the weighted Gram matrix

$$\alpha = \alpha_F \, (\max(\mathrm{diag} \, (\boldsymbol{F}_w \boldsymbol{F}_w^*))), \tag{17}$$

where α_F is a fractional multiplier and the operator diag takes the diagonal of a matrix. Thus, α varies with each iteration step. We choose the α_F value empirically to allow from .1% to 1% misfit to the data. As shown below, our selection of α_F is chosen so that the method is robust to noise present in the data.

Writing the analytical Lagrange solution to equation 16 (Portniaguine, 1999),

$$\boldsymbol{m}_w = \boldsymbol{F}_w^* (\boldsymbol{F}_w \boldsymbol{F}_w^* + \alpha I)^{-1} \boldsymbol{W}_d \boldsymbol{d} \, . \tag{18}$$

The matrix inversion in equation 18 is computed by Gaussian elimination. The model parameters are reconstructed by

$$\boldsymbol{m} = \boldsymbol{W}_m \boldsymbol{m}_w \, , \tag{19}$$

where $\boldsymbol{m}$ is the computed frequency spectrum of the data.

This is the first step of an iteratively re-weighted least squares regularization algorithm (N_i =1, were N_i is the number of iterations). When the window is a boxcar, N_i =1 and α = 0, and $\boldsymbol{d}_i$ is taken to be zero, $\boldsymbol{m}$ is equivalent to the DFT of the data if the frequencies selected are the DFT frequencies. Otherwise, in this first step, when $\alpha \neq 0$ and is small, $\boldsymbol{m}$ is a smooth spectrum that is tighter than the DFT. Figure 3 shows spectra for a 30 Hz Ricker Wavelet windowed with a 40 ms Hann tapered window

centered on the waveform. The full CLSSA solution, ***m***, using N_i =1 and α_F =.001 closely approximates the analytical spectrum of the Ricker wavelet while the Fourier Transform is much broader and exhibits the wrong peak frequency. The CLSSA result without utilizing the imaginary part, is not quite as good, but far better than the Fourier Transform. This is significant because, as no Hilbert operator is applied, CLSSA using only the real waveform has precisely the same temporal resolution as the Fourier Transform while having greatly improved frequency resolution. This indicates that, for a given window, CLSSA has a better Heisenberg Uncertainty Product (standard deviation of the waveform in time multiplied by the standard deviation of the spectrum) than does the Fourier Transform. Thus far, we have not found a window for which this is not the case.

Figure 3 does illustrate an issue at near zero frequencies. The Ricker Wavelet is zero mean and thus should have zero amplitude at zero frequency. However, the mean value over a short window is non-zero and time variant. In fact, it is unclear what is meant by time localization at zero frequency. Let us assume that we have a short time window over which the signal is a constant value. This could be a windowed square wave, box car, step function, constant DC value etc. All have different analytical spectra but no windowed spectral analysis method would have the ability to locally recognize the true spectrum in this case. As a practical matter, the shorter the window, the less meaningful the low frequency values will be.

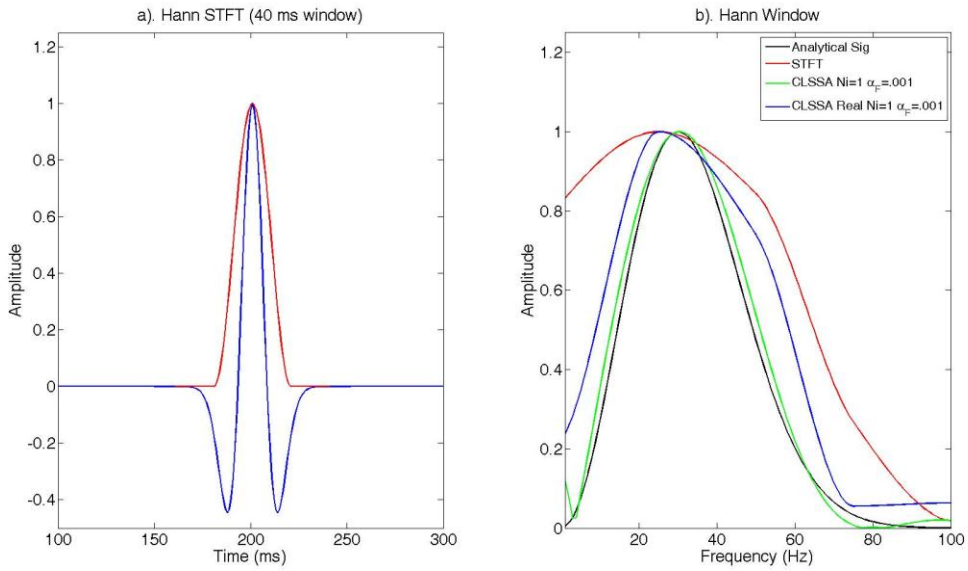

Figure 3). Comparison of results for STFT, CLSSA (Ni=1, α_F=.001) and real valued CLSSA (Ni=1, α_F=.001) applied to a 30 Hz Ricker wavelet using a 40 ms Hann window function. Plots show: the Ricker wavelet with Hann window function and b) comparison of the analytical Ricker spectrum to STFT and CLSSA. CLSSA closely matches the analytical spectrum, while the STFT strongly broadens the spectrum. The real CLSSA solution is intermediate to the CLSSA and STFT.

If more compact spectra are desired (as would be the case for known sparse spectra, or simply to sharpen frequency peaks for attribute analysis) additional iterations can be performed. The model weights are updated by

$$\boldsymbol{W}_m = \mathrm{Diag}(\mathrm{abs}(\boldsymbol{m}))\,. \tag{20}$$

Equation sequence (18)-(19)-(20) is iterated N_i times according to the desired compaction of the model space. Useful rules of thumb seem to be N_i = 1 for least compactness, N_i = 3 for intermediate compactness, and N_i = 10 for most compactness

(sparsest solution). In general, the shorter the window, the greater the number of iterations needed to compact the spectrum.

Figure 4 shows Ricker Wavelet spectra for a very short (20 ms) Hann window. In this case, 2 iterations with α_F =.001 were required for a close match to the analytical spectrum. This illustrates the need for synthetic modeling to empirically select CLSSA parameters.

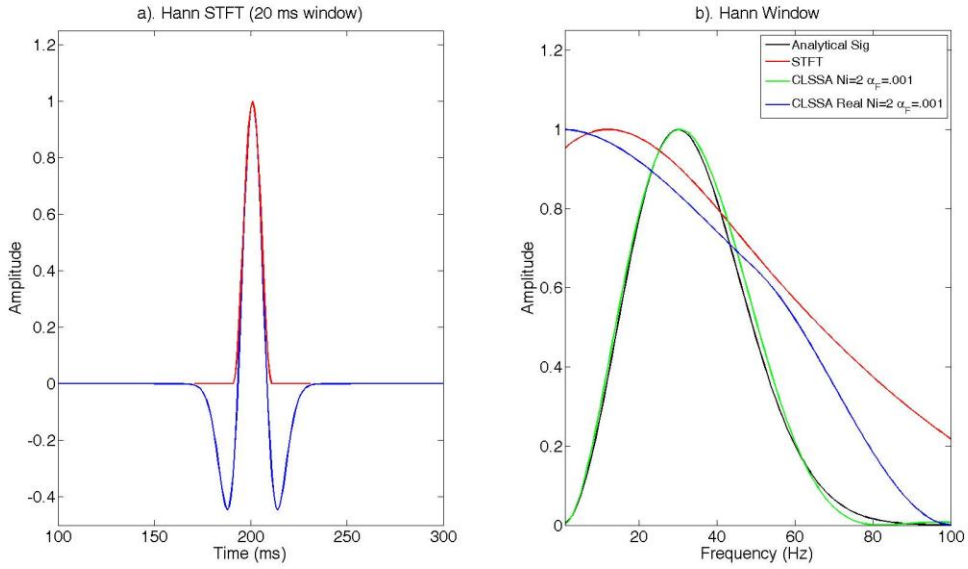

Figure 4). Comparison of results for STFT, CLSSA (Ni=2, α_F=.001) and real valued CLSSA (Ni=2, α_F=.001) applied to a 30 Hz Ricker wavelet using a 20 ms Hann window function. Plots show: the Ricker wavelet with Hann window function and b) comparison of the analytical Ricker spectrum to STFT and CLSSA. CLSSA closely matches the analytical spectrum, while the STFT strongly broadens the spectrum. The real CLSSA solution frequency resolution is slightly better than the STFT.

The values of $\boldsymbol{m}$ at iteration N_i comprise the frequency spectrum of the data at the center of the given time analysis window. For time-frequency analysis, the window is shifted along the seismic trace, and $\boldsymbol{m}_w$ is computed at each time sample in order to

generate a complete 2D time-frequency panel. Because only the data within the short window are inverted at any given computational step, the Gram matrix $\boldsymbol{F}_w\boldsymbol{F}_w^*$ is small and memory limitations are not significant.

The sequence described here is presented as only one representative means of constraining the least-squares spectral analysis. Other constraints, analysis window types, or numerical methods can potentially be applied. Our main objective is to demonstrate the improvements in resolution that can be obtained by solving directly for the Fourier coefficients using constrained least-squares.

2.5. Data and model resolution matrices

In order to study the properties of the inversion formulation, we plot the data and model resolution matrices in Figures 5 and 6. The relationship between the observed and predicted data is given by:

$$\boldsymbol{d}^{pre} = \boldsymbol{F}\boldsymbol{m}^{est} = \boldsymbol{F}[\boldsymbol{F}^{-g}\boldsymbol{d}^{obs}] = [\boldsymbol{F}\boldsymbol{F}^{-g}]\boldsymbol{d}^{obs} = \boldsymbol{N}\boldsymbol{d}^{obs}, \tag{21}$$

where $\boldsymbol{F}$ is the kernel matrix, $\boldsymbol{F}^{-g}$ is the generalized inverse of the kernel matrix, $\boldsymbol{d}^{obs}$ is the observed data, $\boldsymbol{d}^{pre}$ is the predicted data, and $\boldsymbol{N}$ is the data resolution matrix. For our problem (equation 18),

$$\boldsymbol{N} = \boldsymbol{F}_w\boldsymbol{F}_w^*(\boldsymbol{F}_w\boldsymbol{F}_w^* + \alpha I)^{-1}. \tag{22}$$

$\boldsymbol{N}$ is independent of the data and determines how well the data are resolved by the inverse operator. The relationship between the estimated and true model parameters vector is:

$$\boldsymbol{m}^{est} = \boldsymbol{F}^{-g}\boldsymbol{d}^{obs} = \boldsymbol{F}^{-g}[\boldsymbol{F}\boldsymbol{m}^{true}] = [\boldsymbol{F}^{-g}\boldsymbol{F}]\boldsymbol{m}^{true} = \boldsymbol{R}\boldsymbol{m}^{true}, \tag{23}$$

where $\boldsymbol{m}^{est}$ and $\boldsymbol{m}^{true}$ are the estimated and true model parameter vectors. For equation 18, the model resolution matrix is then

$$\boldsymbol{R} = \boldsymbol{F}_w^*(\boldsymbol{F}_w\boldsymbol{F}_w^* + \alpha I)^{-1}\boldsymbol{F}_w . \quad (24)$$

Analogous to $\boldsymbol{N}$, $\boldsymbol{R}$ is independent of the model and determines how well the model parameters are resolved by the inverse operator.

Figure 5 contains plots of the data resolution matrices for relatively short (20 ms) and long (80 ms) windows using a complex sinusoidal kernel basis function. These matrix operators are equivalent to averaging functions applied to the data. Hence, smooth data are influenced less. As is predicted by inverse theory, the data are better resolved for the 20 ms window than the 80 ms window along the diagonal. Conversely, the model resolution is better for the 80 ms window than the 20 ms window (Figure 6).

4. MODELING RESULTS

4.1. Thin layer example

Figure 7 shows the application of CLSSA to the interfering thin layer example shown in Figure 1 where the Fourier Transform was unable to characterize the thin layer spectrum properly with any window length. It can be seen that for the 40 ms window (which is the largest window without interference effects), CLSSA closely approximates the desired spectrum, locates the notch almost exactly, and yields a slightly wrong peak frequency. This is in contrast to the Fourier Transform result with the same window length, which exhibits very misleading notch and peak frequencies.

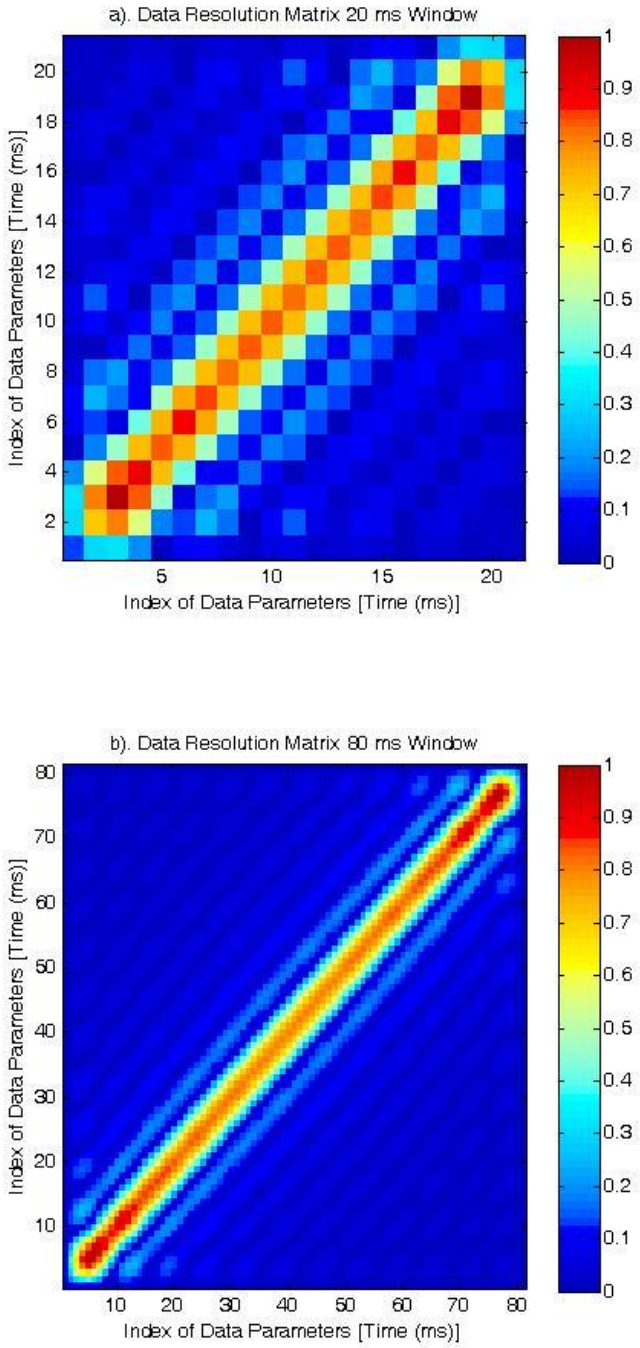

Figure 5). Data resolution matrices of sinusoidal basis ***F*** for (a) 20 ms and (b) 80 ms signals. The sharpness of the diagonal indicates data resolution. The data are better resolved for short windows and smoothed for longer windows.

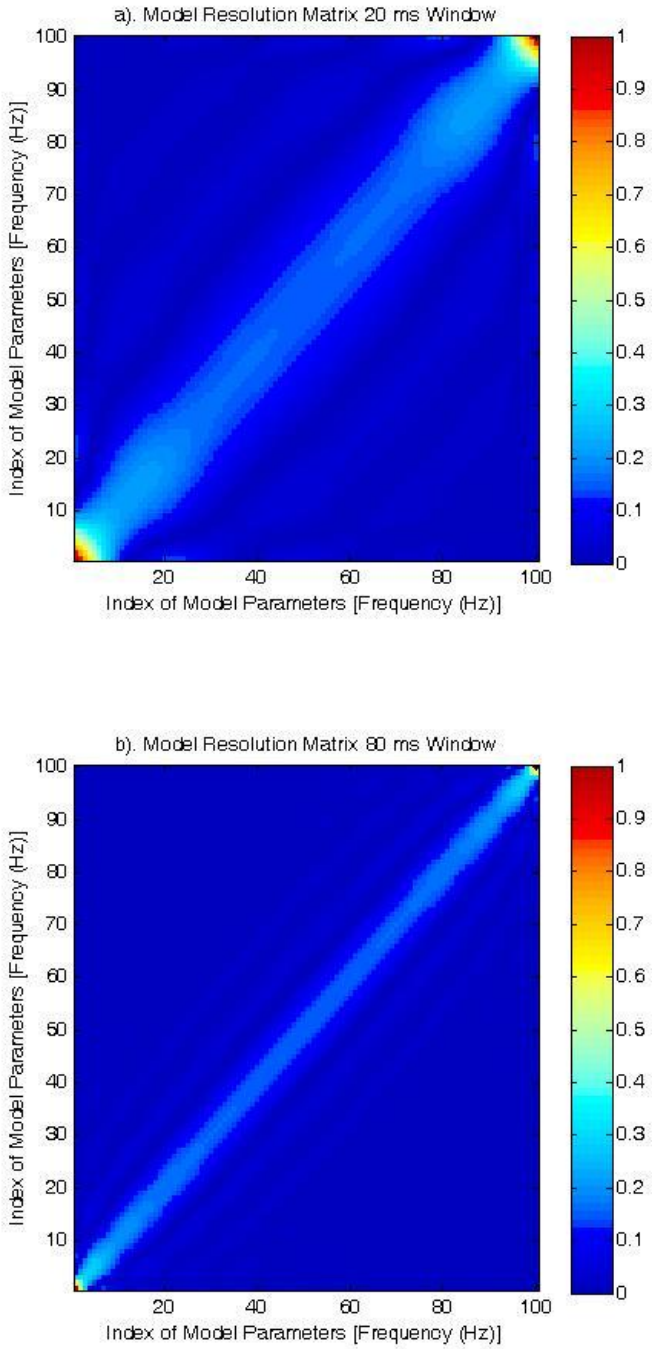

Figure 6). Model resolution matrices of sinusoidal basis ***F*** for (a) 20 ms and (b) 80 ms signals. The sharpness of the diagonal indicates data resolution. The data are better resolved for short windows and smoothed for longer windows.

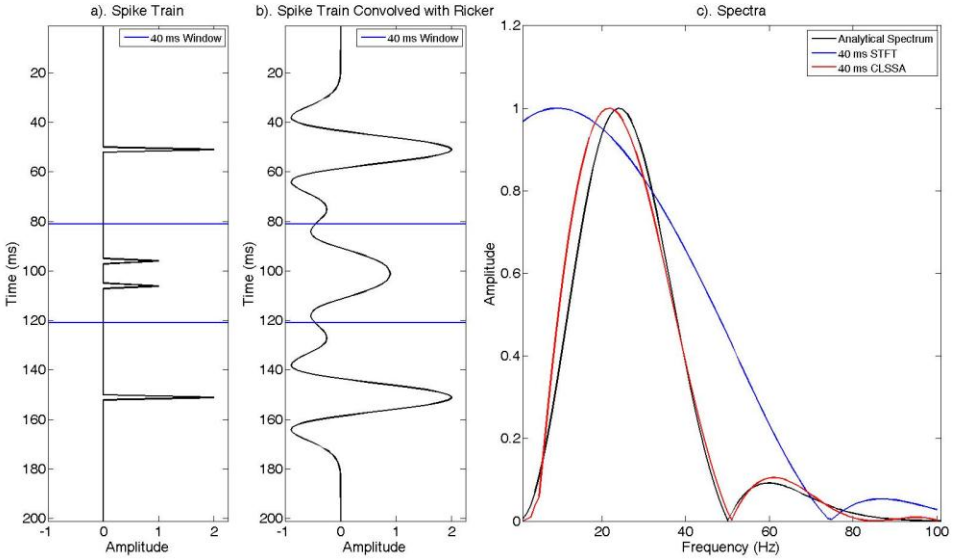

Figure 7). Windowed spectral analysis of an even dipole reflection pair contained within a thick even reflection coefficient (rc) pair. Plots show (a) an even reflection coefficient pair (10 ms thick) with a thicker even rc pair (100 ms thick) falling outside the window, (b) the convolution of the reflection coefficient series with a 30 Hz Ricker wavelet and (c) the spectrum computed using a 40 ms Hann windowed STFT (blue) and CLSSA [Ni=1, α_F=.001] (red) together with the analytical spectrum (black). CLSSA locates the spectral notch much more accurately than the equivalent-window STFT.

4.2. **Application to analytical waveforms (amplitude)**

Analytical waveforms with known frequency spectra are used to compare CLSSA to the STFT and CWT (see Figure 8). Waveforms tested include six cases: (a) a single 20 Hz sinusoid, (b) a pair of 20 Hz and 50 Hz beating sinusoids, (c) a 20 Hz to 50 Hz chirp signal, (d) a single 30 Hz Ricker wavelet, (e) an even pair of interfering Ricker wavelets, each with 30 Hz peak frequency and 10 ms spacing, and (f) an odd pair of interfering Ricker wavelets, each with 30 Hz peak frequency and 10 ms spacing. The trace length is

200 ms, and the sample rate is 1 ms. We computed the STFT and CLSSA of these models using a 40 ms Hann window (the CWT basis function length varies with frequency).

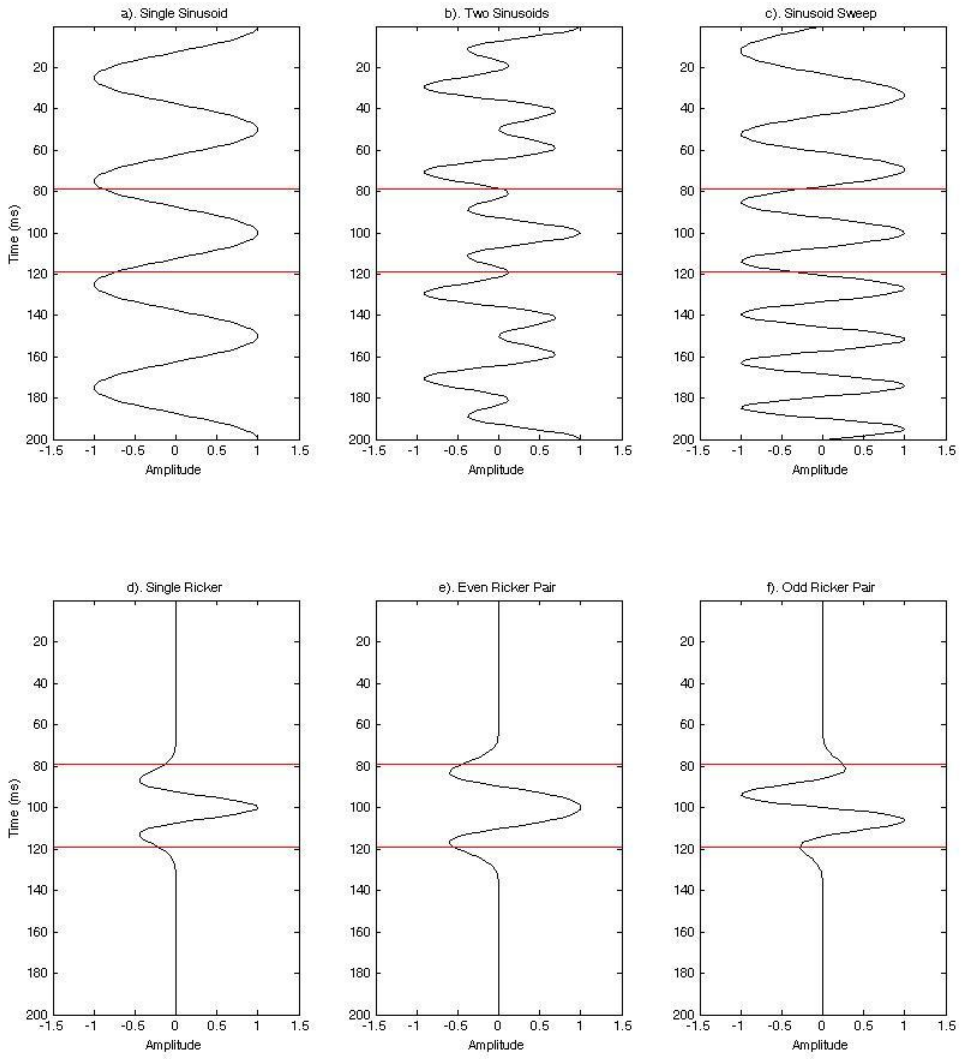

Figure 8). Six trace models with length 200 ms and sampling rate 1 ms. Plots show (a) a single sinusoid at 20 Hz, (b) a pair of sinusoids 20 Hz and 50 Hz superimposed, (c) a chirp frequency sweep between 20 Hz and 50 Hz, (d) a single Ricker wavelet with a peak frequency of 30 Hz, (e) an even pair of 2 interfering Ricker wavelets with peak frequencies of 30 Hz and 10 ms spacing, and (f) an odd pair of 2 interfering Ricker wavelets with peak frequencies of 30 Hz and 10 ms spacing. The horizontal red lines represent a 40 ms time window centered at 101 ms.

Figure 9 shows the time-frequency panels from the application of the STFT to the six analytical waveforms shown in Figure 8. On the sinusoid waveform frequency panels, we observe that the independent frequencies are poorly resolved due to frequency smearing. This smearing is caused by the convolution of the data spectrum with the window transfer function. The STFT results for all model waveforms have notches in time. The time notch period in Figure 9a is inversely related to frequency:

$$T_{sin} = 1/\left(2^{*}\ F_{sin}\right) = 1/\left(2^{*}20\text{Hz}\right) = 25\ \text{ms}, \tag{25}$$

where F_{sin} is the sinusoid frequency and T_{sin} is the time notch period. For multiple sinusoids (Figure 9b), we observe superposition of notches in time. The STFT of the chirp signal (Figure 9c) also shows frequency smearing around the smoothly varying peak frequency within the window and temporal notching. For the Ricker wavelet models, note the smearing of sidelobe energy to zero frequency (referred to as DC). Even and odd dipole pairs have characteristic notch periods in the frequency domain (Marfurt and Kirlin, 2001; Puryear and Castagna, 2008 [Appendix A]) that are determined by layer time thickness. These notches are important interpretive features (Partyka, 1999) and also drive spectral inversion for layer thickness (Puryear and Castagna, 2008 [Appendix A]). If the notches are misplaced, serious interpretation errors can result. The frequency notch period (F_{bed}) of an even dipole with thickness T_{bed} = 10 ms is:

$$F_{bed} = 1/T_{bed} = 1/.01\text{s} = 100\ \text{Hz}. \tag{26}$$

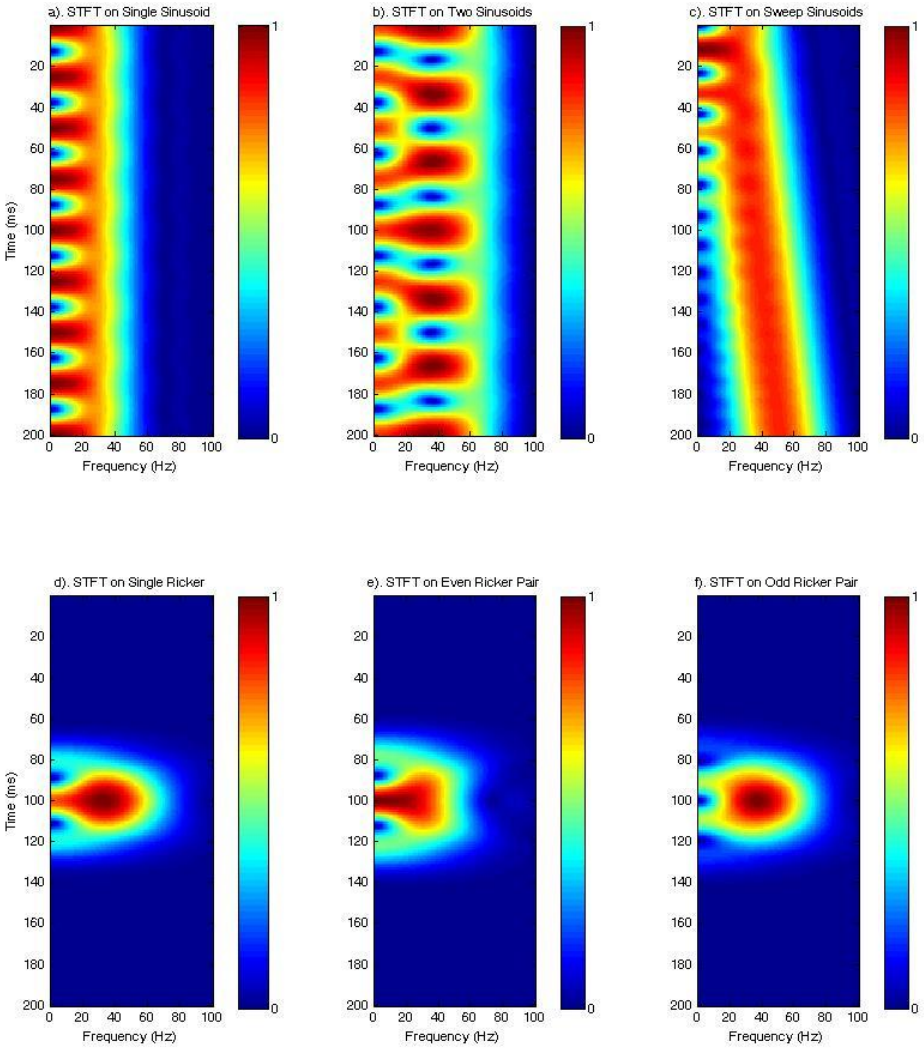

Figure 9). Six amplitude panels illustrating application of the STFT using a window length of 40 ms to the six trace models with length 200 ms and sampling rate 1 ms shown in Figure 6. Figures show (a) a single sinusoid at 20 Hz, (b) a pair of sinusoids at 20 Hz and 50 Hz superimposed, (c) a chirp frequency sweep between 20 Hz and 50 Hz, (d) a single Ricker wavelet with a peak frequency of 30 Hz, (e) an even pair of 2 interfering Ricker wavelets with peak frequencies of 30 Hz and 10 ms spacing, and (f) an odd pair of 2 interfering Ricker wavelets with peak frequencies of 30 Hz and 10 ms spacing.

For the analytical spectrum of the even pair, a peak occurs at 0 Hz and a notch occurs at $F_{bed}/2 = 50$ Hz. On the STFT panel, we observe the notch at approximately 75 Hz due to spectral smearing. In a conventional spectral decomposition analysis, this would result in a large error in layer thickness determination. An analytical odd dipole pair has notches at 0 Hz and 100 Hz, which are not readily observable in these models due to limited wavelet bandwidth. In general, on application of the STFT to real seismic data traces, we expect to observe time notching, frequency smearing, and artificial translation of reflectivity notches to other misleading frequencies.

Figure 10 shows the time-frequency panels from the application of the CWT to the six analytical waveforms shown in Figure 8. The CWT was computed with a Morlet wavelet dictionary. On the sinusoid waveform frequency panels, we observe that the CWT has better low frequency spectral resolution than does the STFT (Figure 10a). Furthermore, the CWT has better spectral resolution at 20 Hz than at 50 Hz (Figure 10b). In Figure 10c, we observe a smooth decrease in frequency resolution as a function of increasing frequency and decreasing Morlet basis independence. However, for the CWT, higher frequency resolution is achieved at the cost of time resolution. The Ricker panels show very significant smoothing across time at low frequencies; this smoothing effect diminishes as frequency increases. For the even dipole pair CWT (Figure 10e), the reflectivity notch occurs at approximately 60 Hz compared to the analytical notch at 50 Hz. On application of the CWT to real seismic data traces, we expect poor time

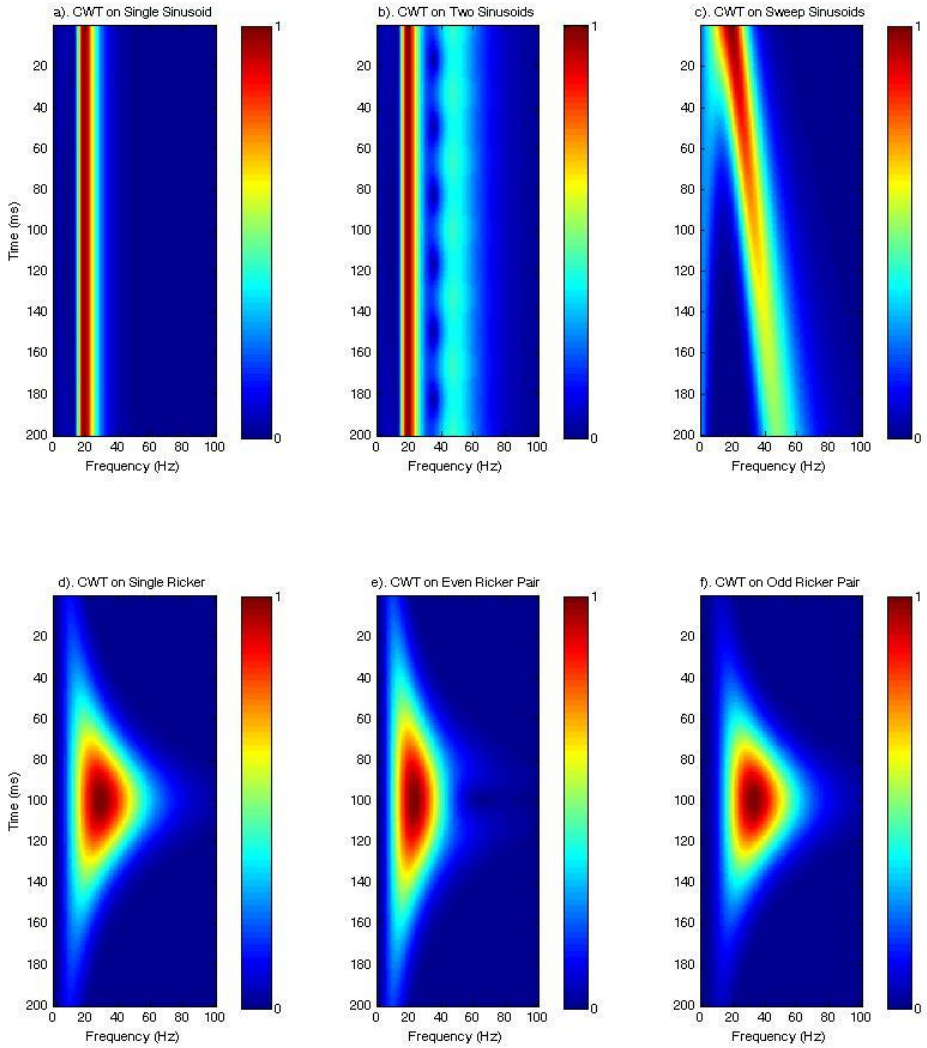

Figure 10). Six amplitude panels illustrating application of the CWT with a Morlet wavelet dictionary to the six trace models with length 200 ms and sampling rate 1 ms shown in Figure 6. Figures show (a) a single sinusoid at 20 Hz, (b) a pair of sinusoids 20 Hz and 50 Hz superimposed, (c) a chirp frequency sweep between 20 Hz and 50 Hz, (d) a single Ricker wavelet with a peak frequency of 30 Hz, (e) an even pair of 2 interfering Ricker wavelets with peak frequencies of 30 Hz and 10 ms spacing, and (f) an odd pair of 2 interfering Ricker wavelets with peak frequencies of 30 Hz and 10 ms spacing.

resolution and high frequency resolution at low frequencies and high time resolution and poor frequency resolution at high frequencies.

Figure 11 shows the time-frequency panels from the application of the CLSSA to the six analytical waveforms shown in Figure 8. For models a-c, N_i = 10; and for models d-f, N_i = 1. On the sinusoid waveform frequency panels, we observe nearly perfect resolution of frequency content. The frequency coefficients are not smeared into their neighbors (i.e. there is no significant window smearing effect or spectral leakage). This observation is significant in that the neighboring frequency components are not well separated by the STFT. The CLSSA Ricker wavelet results also show obvious improvement in low-frequency time-resolution relative to the CWT and frequency resolution relative to both the STFT and CWT. The CLSSA Ricker spectra are more compact because they are not broadened by windowing effects. In Figure 11e, the expected thin-bed notch appears close to the correct location (50 Hz) within the wavelet band. On application to real seismic data traces, we expect significant improvement in frequency resolution and the time-frequency resolution product over the STFT and CWT.

In order to further illustrate differences among the STFT, CWT, and CLSSA, we extract line spectra at the time midpoint of the analytical waveform traces and compare them to their respective analytical spectra (Figure 12). In Figures 12a and 12b, the STFT has a very strong DC component that is more representative of the spectrum of the Hann taper than of the data themselves. The CWT produces a spectrum that is more

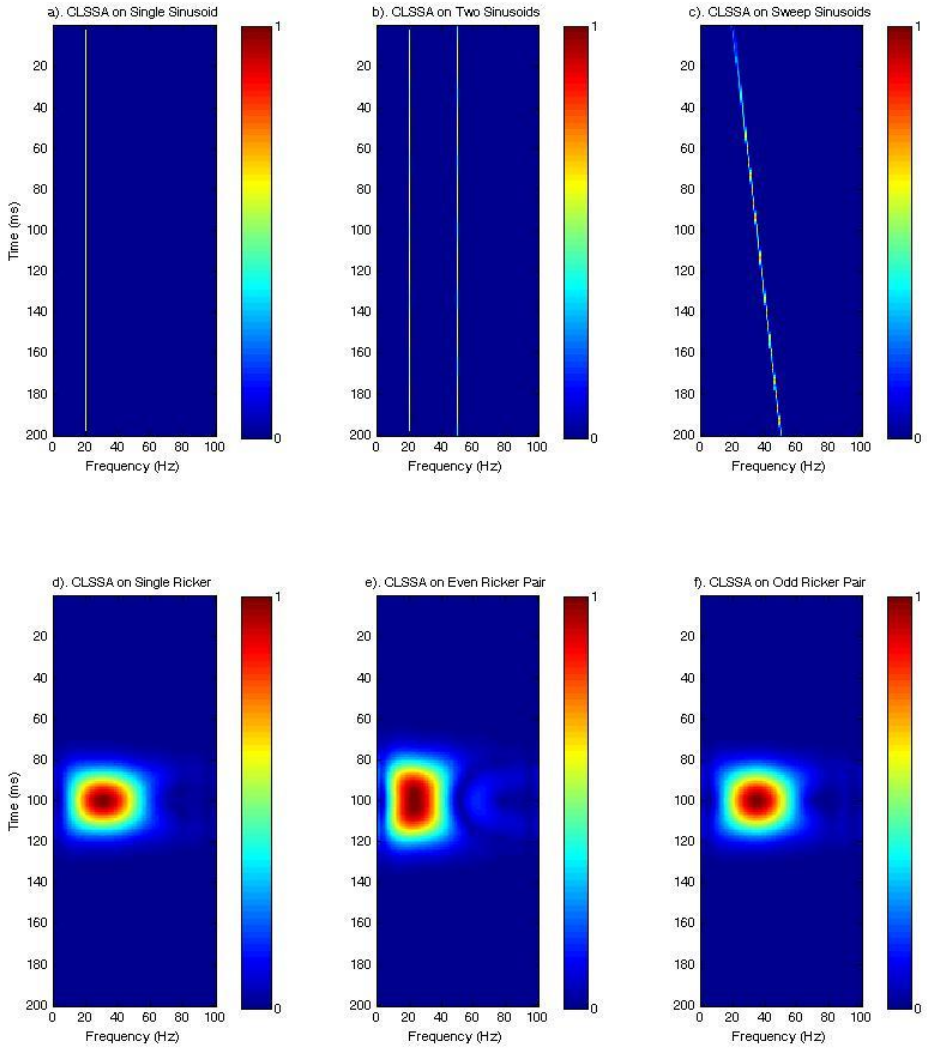

Figure 11). Six amplitude panels illustrating application of the CLSSA using a window length of 40 ms to the six trace models with length 200 ms and sampling rate 1 ms shown in Figure 6. Figures show (a) a single sinusoid at 20 Hz, (b) a pair of sinusoids 20 Hz and 50 Hz superimposed, (c) a chirp frequency sweep between 20 Hz and 50 Hz, (d) a single Ricker wavelet with a peak frequency of 30 Hz, (e) an even pair of 2 interfering Ricker wavelets with peak frequencies of 30 Hz and 10 ms spacing, and (f) an odd pair of 2 interfering Ricker wavelets with peak frequencies of 30 Hz and 10 ms spacing. For models a-c, $N_i = 10$; and for models d-f, $N_i = 1$.

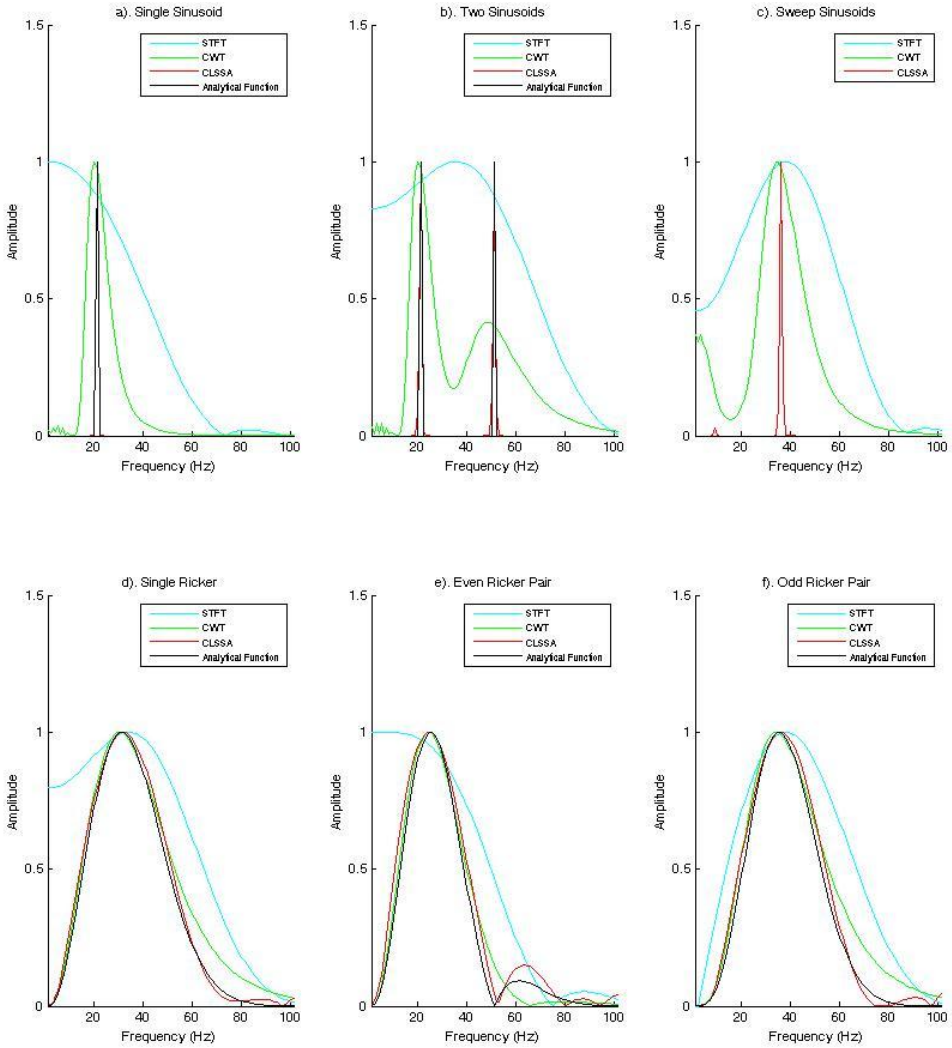

Figure 12). Six amplitude plots comparing the STFT, CWT, CLSSA, and the analytical spectra of the six trace models shown in Figure 6 at the center of the trace (t = 101 ms). The STFT and CLSSA used a window length of 40 ms. Figures show the comparison for (a) a single sinusoid at 20 Hz, (b) a pair of sinusoids 20 Hz and 50 Hz superimposed, (c) a chirp frequency sweep between 20 Hz and 50 Hz, (d) a single Ricker wavelet with a peak frequency of 30 Hz, (e) an even pair of 2 interfering Ricker wavelets with peak frequencies of 30 Hz and 10 ms spacing, and (f) an odd pair of 2 interfering Ricker wavelets with peak frequencies of 30 Hz and 10 ms spacing. For models a-c, N_i = 10; and for models d-f, N_i = 1. Reflectivity notching patterns obscured by the DFT and CWT are apparent in the CLSSA 2D spectral panel result.

narrowly centered on the model sinusoid frequencies, although frequency resolution is still imperfect. The CLSSA closely matches the exact analytical solution. The waveform illustrated in Figure 12c has no analytical solution since frequency varies continuously with time. However, the average frequency within the centrally located window is approximately 35 Hz. In applying the 40 ms window, the window smearing effect renders the STFT ineffective for spectral analysis of the waveform. The CLSSA computed spectra of the Ricker wavelet waveforms are narrower than those computed using the DFT and CWT and closer to the analytical spectrum. Note the accurate position of the notch in Figure 12e.

4.3. **Application to analytical waveforms (phase)**

We compute cosine of the phase from STFT, CWT, and CLSSA on the models shown in Figure 8 d-f using the same parameters defined in the previous section, and plot the results in Figures 13-15 respectively. We study cosine of the phase instead of the unmodified phase output in order to eliminate phase wrapping effects. In general, although the single Ricker and even Ricker models are zero phase, phase changes occur as the analysis point slides through the model due to the location of moving window. For all single Ricker plots and even Ricker models, zero phase occurs at the center of the models; and, for the odd Ricker pair, a phase polarity reversal occurs as the window slides across the center lobe because the waveform is anti-symmetric. The CWT and CLSSA have longer phase tails at low frequency due to the frequency dependent window

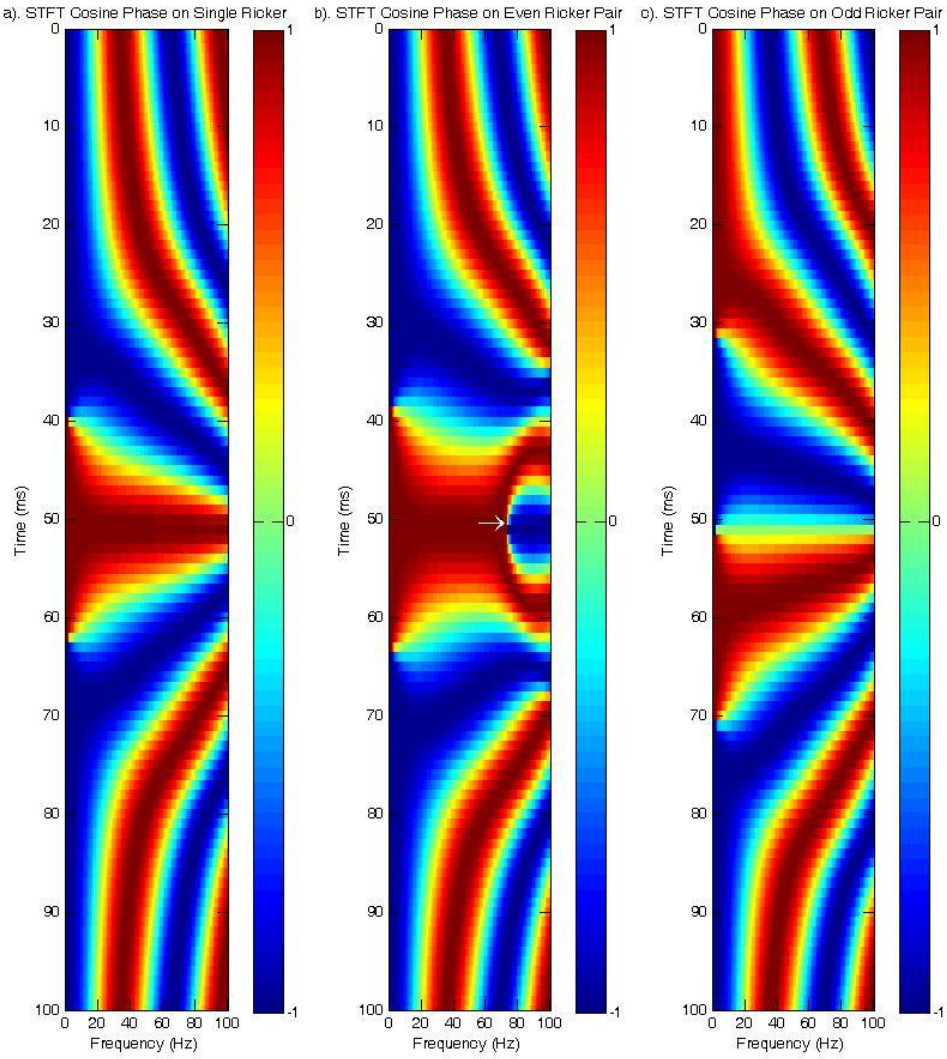

Figure 13). Six phase panels illustrating application of the STFT using a window length of 40 ms to the six trace models with length 200 ms and sampling rate 1 ms shown in Figure 6. Figures show (a) a single Ricker wavelet with a peak frequency of 30 Hz, (b) an even pair of 2 interfering Ricker wavelets with peak frequencies of 30 Hz and 10 ms spacing, and (c) an odd pair of 2 interfering Ricker wavelets with peak frequencies of 30 Hz and 10 ms spacing.

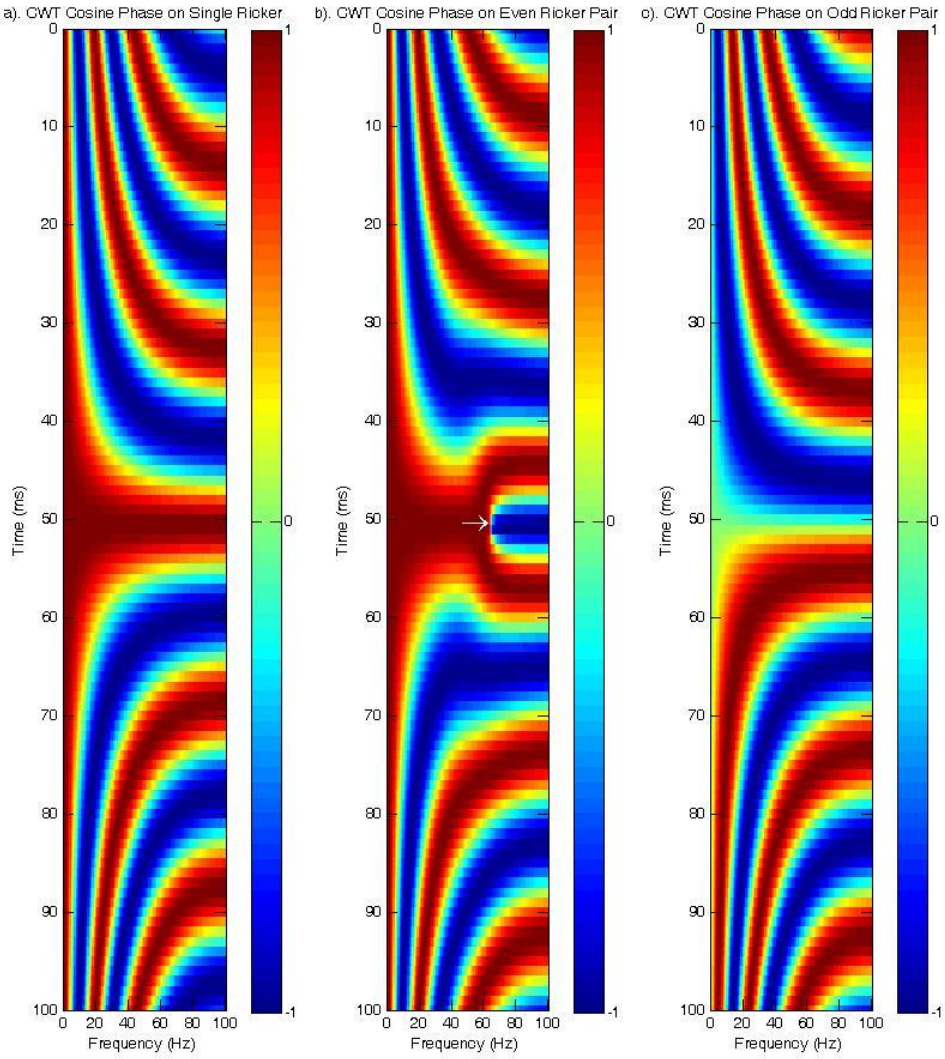

Figure 14). Six phase panels illustrating application of the CWT using a window length of 40 ms to the six trace models with length 200 ms and sampling rate 1 ms shown in Figure 6. Figures show (a) a single Ricker wavelet with a peak frequency of 30 Hz, (b) an even pair of 2 interfering Ricker wavelets with peak frequencies of 30 Hz and 10 ms spacing, and (c) an odd pair of 2 interfering Ricker wavelets with peak frequencies of 30 Hz and 10 ms spacing.

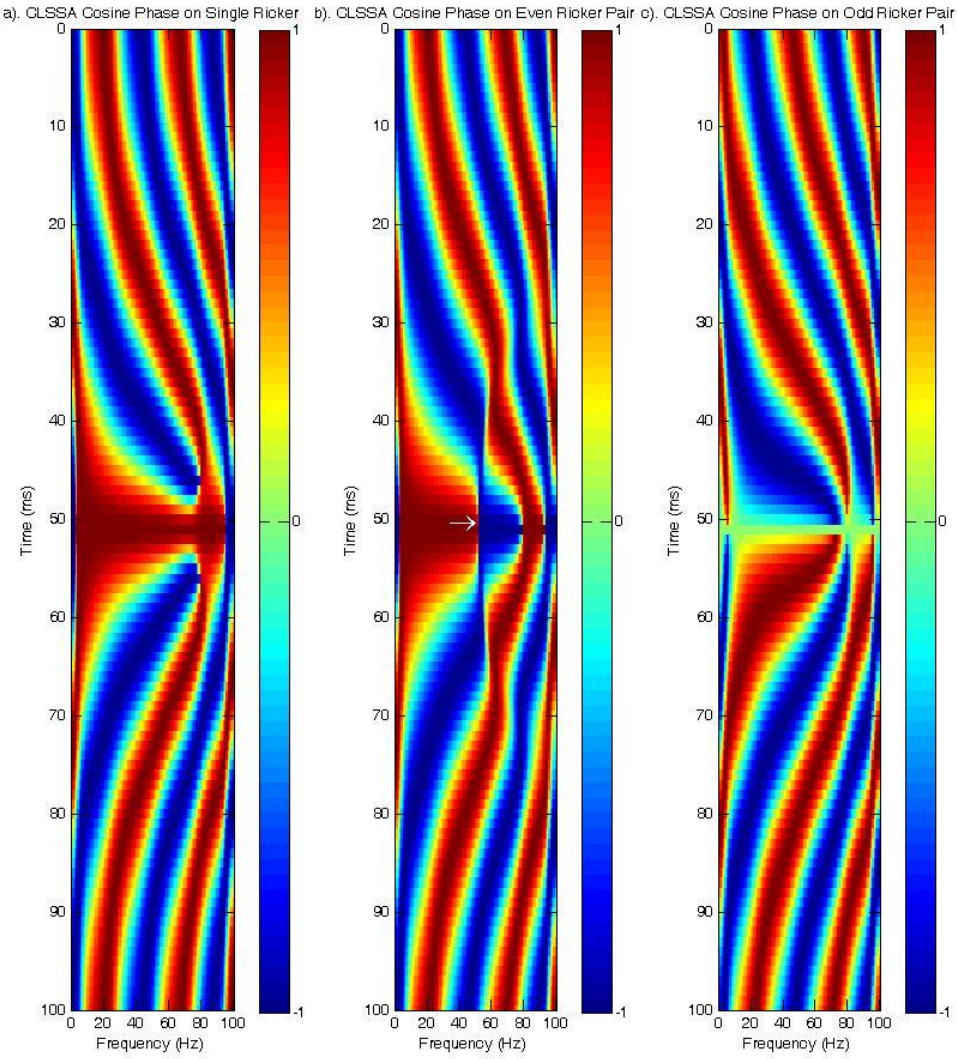

Figure 15). Six phase panels illustrating application of the CLSSA using a window length of 40 ms to the six trace models with length 200 ms and sampling rate 1 ms shown in Figure 6. Figures show (a) a single Ricker wavelet with a peak frequency of 30 Hz, (b) an even pair of 2 interfering Ricker wavelets with peak frequencies of 30 Hz and 10 ms spacing, and (c) an odd pair of 2 interfering Ricker wavelets with peak frequencies of 30 Hz and 10 ms spacing.

and Hilbert Transform respectively. A feature of interest is the analytical amplitude notch location previously computed for the even Ricker model. This notch should occur at 50 Hz. On phase plots, the notch corresponds to the location of a phase reversal on the frequency axis, which is particularly prominent in plots. In the even Ricker pair models for each transform, white arrows show the location of the phase reversal. We observe that the reversal approaches 50 Hz sequentially for STFT, CWT, and CLSSA respectively. Thus, the accuracy interpretation of layering characteristics using phase can be improved by using CLSSA.

4.4. **Effect of varying α_F**

The variation of parameter α_F creates a tradeoff between stability and goodness of fit. For a linear problem, increasing α_F is equivalent to increasing the energy on the diagonal, thereby stabilizing the inversion. Figure 16 illustrates the loss of accuracy in terms of residual as a percent of total amplitude that results from increasing α_F for a 40 ms Hann window centered on a Ricker wavelet signal. As α_F is increased to .1, the residual grows to a significant percentage of the total amplitude. Thus, inversion accuracy is compromised by introducing a large α_F. As previously stated, we set α_F=.001 as default in our implementation. This generally produces solutions that are robust to noise without significantly sacrificing accuracy.

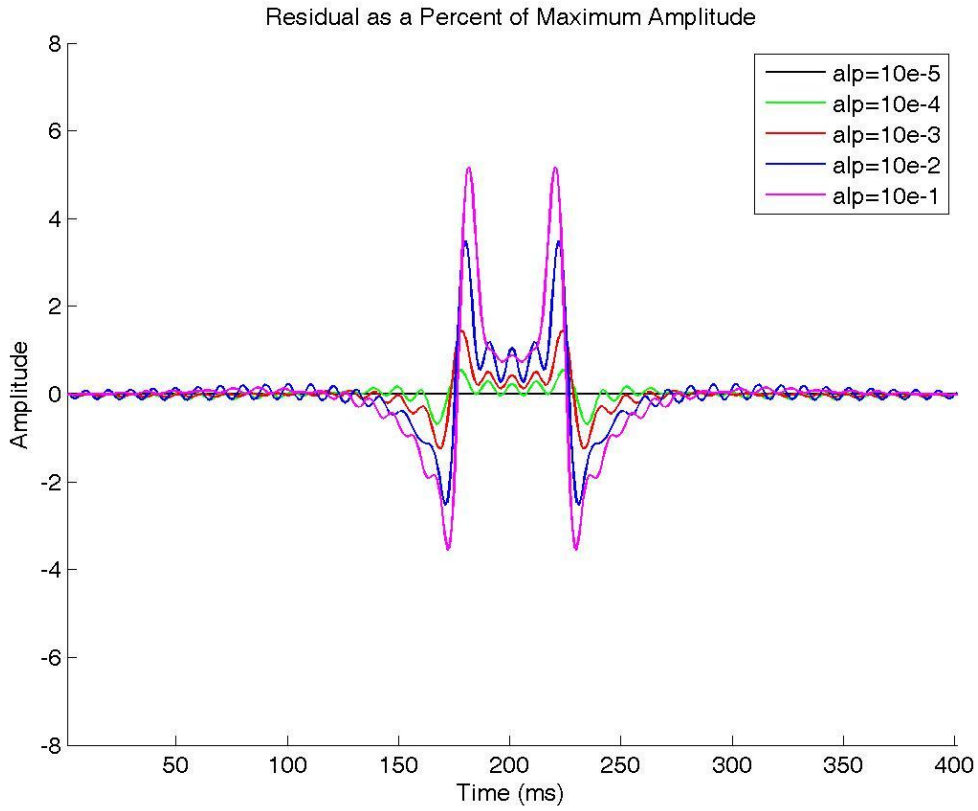

Figure 16). Illustration of varying α in computing the 40 ms Hann window CLSSA (Ni=1, α_F=.001) spectrum centered on a Ricker wavelet. As α is increased, the goodness of fit decreases, while the stability of the solution increases.

4.5. **Effect of varying N_i**

In order to assess the impact of varying the number of iterations N_i of the method, we plot solutions for different N_i values applied to a 30 Hz Ricker wavelet within a 40 ms window in Figure 17. It is clear that while the CLSSA result for N_i =1 closely approximates the true Ricker spectrum, increasing the number of iterations generates progressively sparser solutions. In the limit, these solutions tend toward a 3-sinusoid model as N_i increases. Thus, the Ricker wavelet within the windowed portion

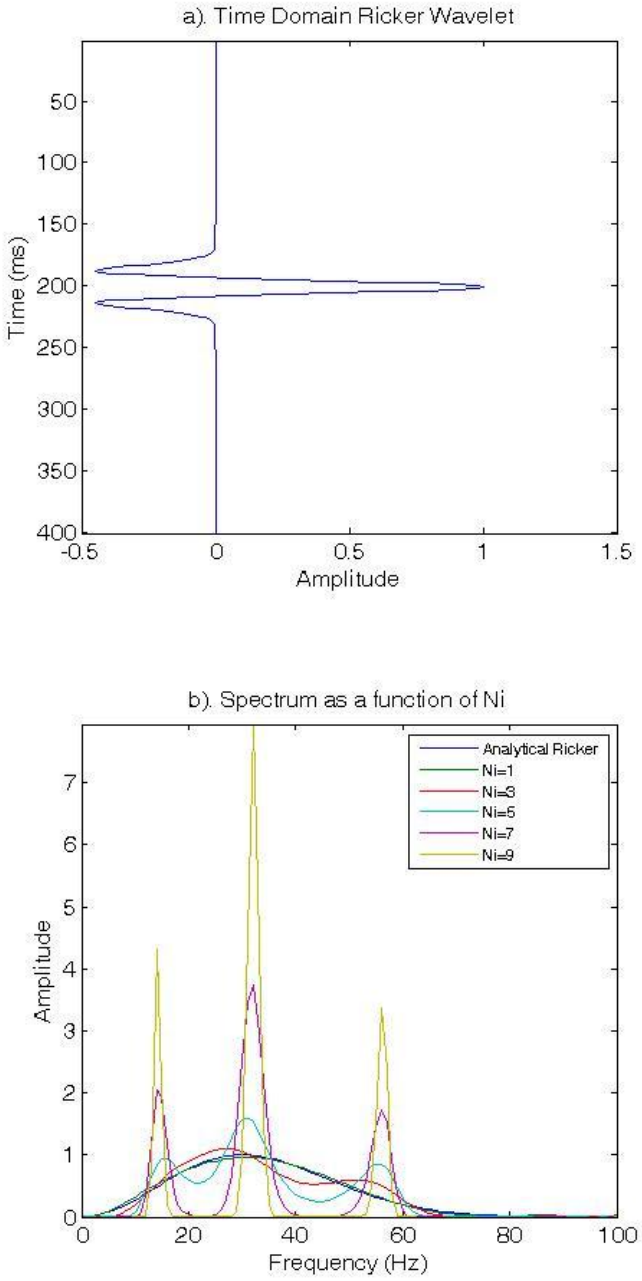

Figure 17). Solutions for different Ni values applied to a 30 Hz Ricker wavelet within a 40 ms window. While Ni=1 closely approximates the true Ricker spectrum, increasing the number of iterations generates progressively sparser solutions. In the limit, these solutions tend toward a 3-sinusoid model as Ni increases (i.e. Ni=9). Thus, the Ricker wavelet within the windowed portion of the data could be accurately modeled as 3 beating sinusoids.

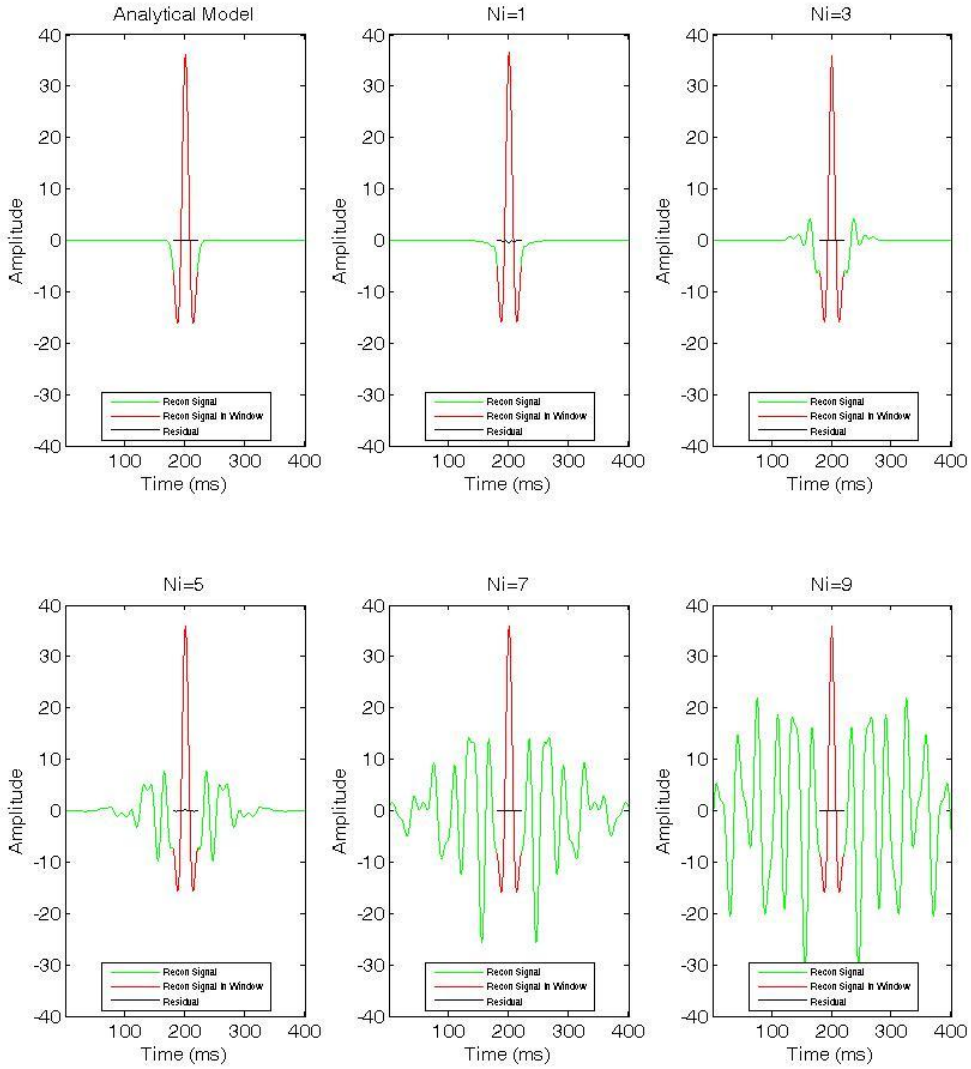

Figure 18). Time-domain reconstruction of the Ricker wavelets within the window for the suite of Ni values. Note that, while all values of Ni closely match the signal within the window, the smooth Ni=1 spectrum produces the best match outside the window and most compact time domain representation of the signal. As further iterations (i.e. Ni>1) drive more frequency compactness, one observes increasing energy outside of the analysis window because the signal is approximated by fewer sinusoidal waveforms. However, note that notched spectra dominated by reflectivity might be better modeled by Ni>1.

of the data can be modeled well as 3 beating sinusoids. Figure 18 shows the time-domain reconstruction of the Ricker wavelets within the window for the suite of N_i values. Note that, while results for different N_i closely match the signal within the window, the smooth N_i =1 spectrum produces the best match outside the window and the most compact time domain representation of the signal. As further iterations (i.e. Ni>1) drive more frequency compactness, one observes increasing energy outside of the analysis window because the signal is approximated by fewer sinusoidal waveforms.

4.6. **Application to layered synthetic traces**

We constructed layered blocky impedance synthetic models comprised of even and odd reflectivity dipoles in series. Time thicknesses are varied from 0 ms to 32 ms with a layer center spacing of 100 ms. The wavelet, reflectivity models, and resulting convolutional synthetic models are illustrated in Figures 19 a-c and 20 a-c. We applied the STFT, CWT, and CLSSA (N_i = 1) to the even and odd synthetic events (Figures 19 d-f and 20 d-f). The STFT artifacts obscure the systematic reflectivity patterns and event identification in the frequency domain. The CWT suffers from the use of low frequency wavelets to analyze the low frequency components. These wavelets are temporally non-localized, and mix information from disparate reflectors. Hence, interferences between not only the bounding surfaces of individual thin layers but also interferences between nearby layers themselves are observed in the time-frequency panels as low frequency streaking artifacts. This effect can lead to false inferences about local

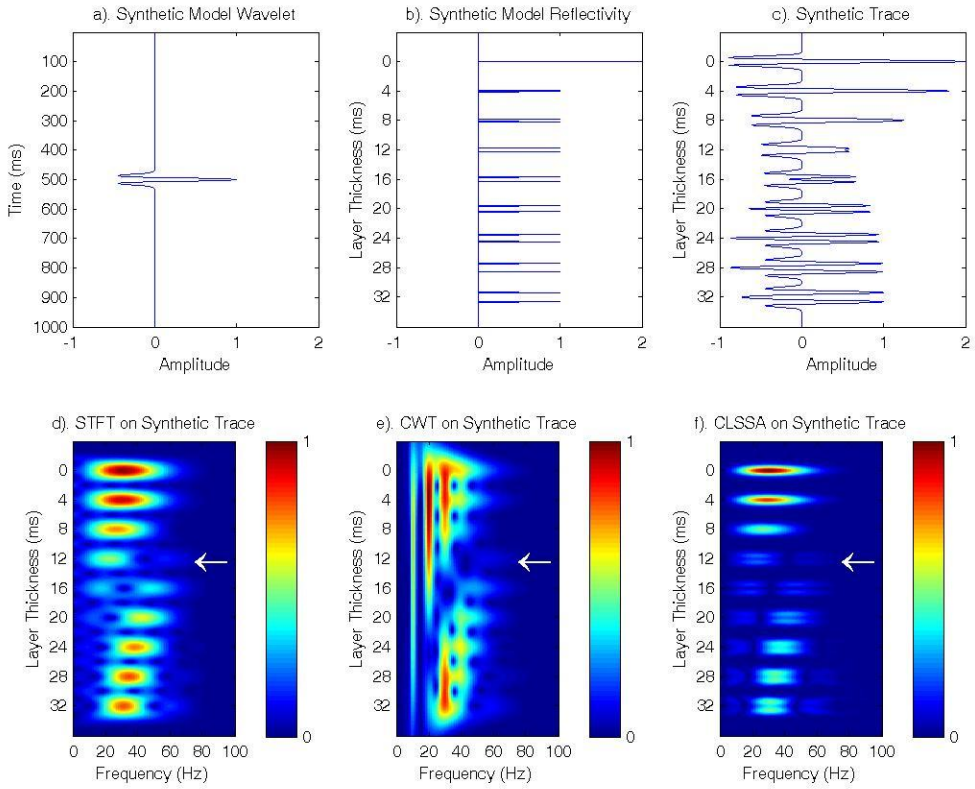

Figure 19). Even dipole pair synthetic reflectivity model with increasing thickness as a function of time. In order to demonstrate robustness in the presence of noise, we added noise having an L2-norm equal to .1 times the L2-norm of the signal. Figures show (a) reflectivity model, (b) Ricker wavelet with center frequency = 30 Hz, (c) synthetic model trace, (d) STFT applied to the synthetic trace using a window length of 40 ms, (e) CWT using a Morlet wavelet dictionary applied to the synthetic trace, and (f) CLSSA (N_i =1) applied to synthetic trace using a window length of 40 ms. The three methods show comparable robustness in the presence of noise. Reflectivity notching patterns related to thickness are obscured by the DFT and CWT, and apparent in the CLSSA spectral panel result. Temporal separation of events is better for the CLSSA result, which resolves layers as thin as approximately 12 ms at high frequencies (arrow). For beds thinner than this threshold, the events merge.

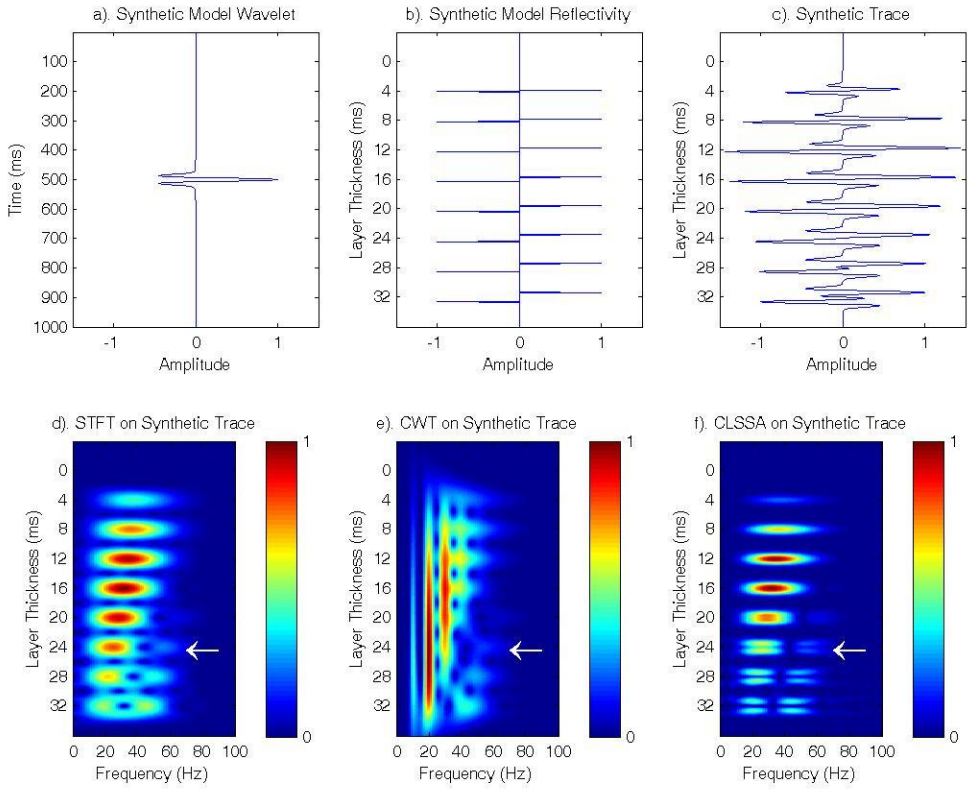

Figure 20). Odd dipole pair synthetic reflectivity model with increasing thickness as a function of time. In order to demonstrate robustness in the presence of noise, we added noise having an L2-norm equal to .1 times the L2-norm of the signal. Figures show (a) reflectivity model, (b) Ricker wavelet with center frequency = 30 Hz, (c) synthetic model trace, (d) STFT applied to the synthetic trace using a window length of 40 ms, (e) CWT applied to synthetic trace, and (f) CLSSA (N_i = 1) applied to synthetic trace using a window length of 40 ms. The three methods show comparable robustness in the presence of noise. None of the events are resolved by the STFT and CWT. Reflectivity notching patterns obscured by the CWT are apparent in the STFT and CLSSA spectral panels. CLSSA exhibits sharper spectral notches defining thin bed dipoles in the time domain. Temporal separation of events is observed for layers as thin as approximately 24 ms at high frequencies (arrow). For layers thinner than this threshold, the notching, observed at high frequencies, moves outside the data. The three methods show robustness in the presence of noise.

reflectivity. The CWT spectrum is not instantaneous; and, therefore, cannot quantify localized reflectivity spectra. In contrast, the CLSSA resolves the systematic shift in reflectivity notches (decreasing notch frequency with increasing thickness) and resolves top and base events 12 ms thick and greater for the even pair and 24 ms thick and greater for the odd pair. This difference in apparent resolution is due to the fact that a perfectly odd dipole conforms to the classical Widess (1973) resolution limit while the even impulse pair does not (see Puryear and Castagna, 2008). Also, the odd dipole pair notch occurs at higher frequencies than the even dipole notch (and can be outside the band of the data), thereby obscuring high frequency expressions of temporal thickness.

In order to assess robustness in the presence of noise, we added different types of noise to the CLSSA models and plotted the results in Appendix C. Furthermore, examples of Matlab CLSSA code to produce Figures 19 c and f and 20 c and f are given in Appendix D.

4.7. **Resolution analysis**

In order to better understand the time and frequency resolution characteristics of the STFT and the CLSSA (N_i = 1), we applied the transforms using a range of window lengths centered on a Hann tapered Ricker Wavelet, and quantified the results using the standard deviation from the peak frequency of the spectrum as a measure of frequency resolution. This analysis would not be meaningful on the CWT because the effective window length is a function of frequency. In Figure 21, we plot the frequency standard deviation around peak frequency normalized by peak frequency vs. the window length

normalized by the period of the peak frequency. The normalization is therefore scale independent.

As windowing always broadens the Fourier spectrum, the standard deviation is traditionally used to measure frequency resolution (see discussion of Heisenberg's Uncertainty Principle in Bracewell, 1986). We used CLSSA both with and without the Hilbert operator. When using only the real waveform, CLSSA has exactly the same window length as the Fourier Transform; the plot thus proves that real CLSSA has better frequency resolution and Heisenberg uncertainty product than the Fourier Transform. For full CLSSA, the Hilbert operator senses data somewhat outside of the analysis window, so the comparison to Fourier is less exact. Nevertheless, the improvement in frequency resolution is clear, particularly for window lengths greater than twice the period corresponding to the peak frequency, where real and full CLSSA converge in resolution. As window length is reduced towards the period of the peak frequency, resolution of real CLSSA approaches that of the Fourier Transform. Below the period of the peak frequency, real CLSSA becomes unreliable and the comparison is less meaningful. It can be seen that for short windows, the stabilizing influence of using the Hilbert operator results in superior frequency resolution.

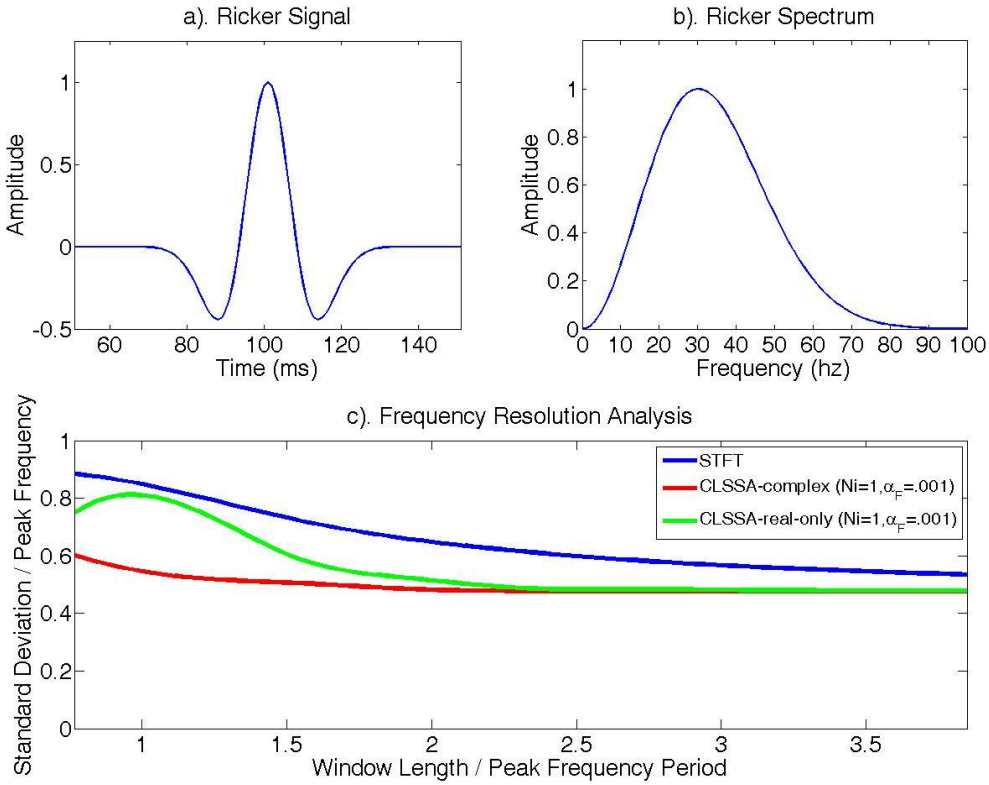

Figure 21). Frequency Resolution test for Hann windowed STFT and CLSSA (Ni=1, α_F=.001) spectra of a Ricker wavelet. We compute standard deviation from the peak frequency. Plots show: (a) a 30 Hz Ricker wavelet signal, (b) the true Ricker wavelet spectrum and equivalent Gaussian function plotted to one standard deviation (c) weighted standard deviation computed on the STFT, CLSSA (Ni=1, α_F=.001), and real CLSSA (Ni=1, α_F=.001) frequency spectra (normalized by the peak frequency) for Hann windows ranging from 20 ms to 100 ms (normalized by the dominant period in the plot) applied to the Ricker wavelet. CLSSA has a significantly smaller weighted standard deviation than the STFT (i.e. the computed spectra are narrower for all window lengths within this standard use range). Real CLSSA shows similar advantages for longer windows (Window Length/Dominant Period>2). For very long windows, the standard deviation results of all methods converge.

4. REAL DATA RESULTS

4.1. Real data trace frequency panels

We compare the STFT, CWT, and CLSSA using frequency panels for a seismic data set with a bright spot associated with a known hydrocarbon accumulation. If well control is available, Ni should be chosen based on synthetic modeling. In the absence of well control, we chose Ni=3 because it reveals high-resolution peak frequency trends in the up-dip and down-dip example traces. In Figures 22 and 23, we display frequency panels through the formation at the bright spot (t = 350 ms) and correlative down-dip (t = 365 ms) sand locations. Displayed are the original trace, time-frequency gathers for the STFT, CWT, and CLSSA, peak frequency for each method, and standard deviation in frequency for each method. In order to fix the time resolution while studying frequency resolution, we applied the STFT and CLSSA using identical 20 ms Hann tapered windows.

The CWT has very poor time resolution at low frequencies, and is dominated by the mixing of low frequency energy from nearby reflectors in the temporal vicinity of the bright spot (Figure 22c). The STFT result includes the doublet artifact of the trough over peak reservoir event, resulting from a strong DC bias when the short window predominantly isolates a single positive or negative waveform loop. Although the STFT and CLSSA show comparable time resolution fixed by the choice of window length, the CLSSA frequency section yields superior detail of the frequency characteristics of the bright spot sand. The STFT frequency energy is smeared across the spectrum and outside the bandwidth of the data, yielding poor frequency resolution and shifting the

peak frequency to the high end of the spectrum. CLSSA spectral energy is not smeared outside the actual data bandwidth at the upper limit, although a local DC component appears at the side-lobes due to the short window. It is noteworthy that the CLSSA yields high frequency resolution and accuracy using such a short window, while spectral distortion from the STFT renders it unsuitable for spectral analysis using the same short window.

We computed peak frequencies and standard deviations where trace sample amplitudes were greater than 2 percent of the maximum amplitude, excluding DC peak frequencies (an artifact of the short window). Peak frequency vs. time for the up-dip sand is shown in Figure 22e. Note the significantly higher STFT peak frequencies at the reservoir and the correlative down-dip sand due to spectral smearing. In general, the CLSSA yields higher peak frequency estimates than the CWT, which is biased toward low frequency energy. Mean peak frequencies are 40.56 for the STFT, 16.67 for the CWT, and 25.95 for CLSSA. Standard deviation vs. time for the up-dip sand is plotted in Figure 22f. Like peak frequencies, standard deviations about the mean frequency of the STFT are consistently and significantly higher than those of the CWT and CLSSA. CLSSA generally has lower standard deviation values than the CWT (it has better frequency resolution). Mean standard deviations are 4.98 for the STFT, 2.02 for the CWT, and 1.59 for CLSSA.

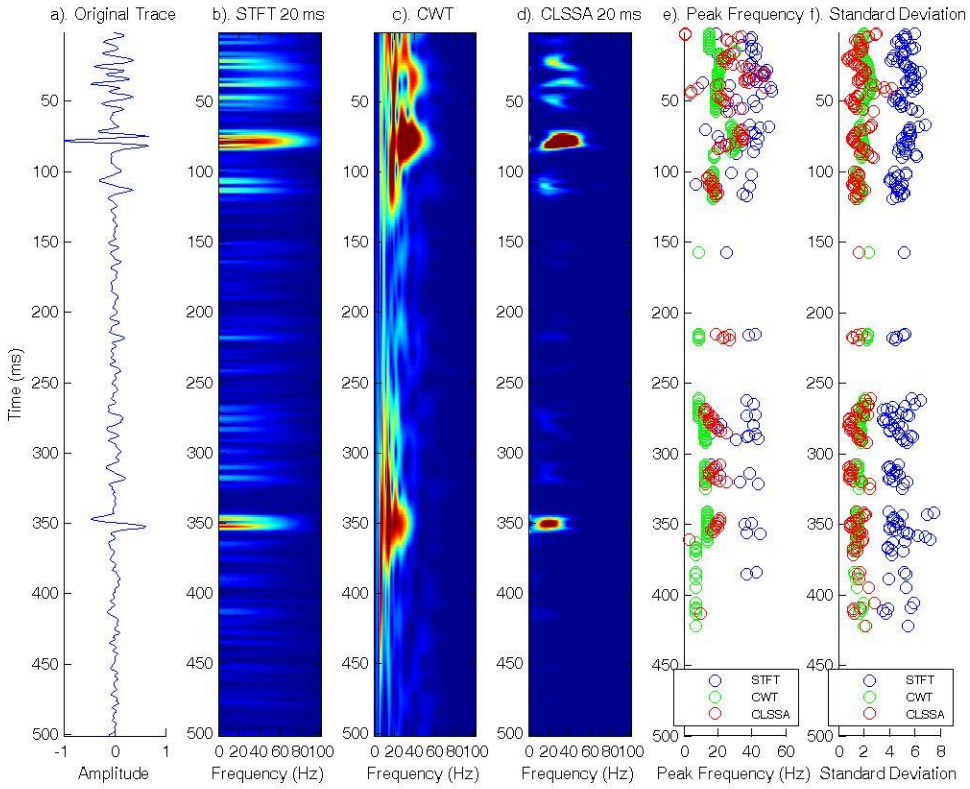

Figure 22). Up-dip real data trace with spectral decomposition and associated attributes (reservoir is at approximately t = 350 ms). Plots show (a) the original synthetic trace, (b) the 20 ms window STFT result, (c) the CWT result, (d) the 20 ms window single iteration CLSSA (N_i = 3) result, (e) thresholded peak frequencies where amplitude is greater than 2 percent of maximum amplitude and DC peak frequencies are excluded, and (f) thresholded amplitude-weighted standard deviations where amplitude is greater than 2 percent of maximum amplitude.

On the down-dip trace (Figure 23), it is also clear that CLSSA is more sensitive to local peak frequency variation than STFT and CWT and that its standard deviations are lower. We anticipate that CLSSA will produce better stratigraphic resolution on frequency attribute maps. While amplitudes are dimmer on the down-dip section, peak frequencies are lower, indicating possible changes in the reflectivity spectrum.

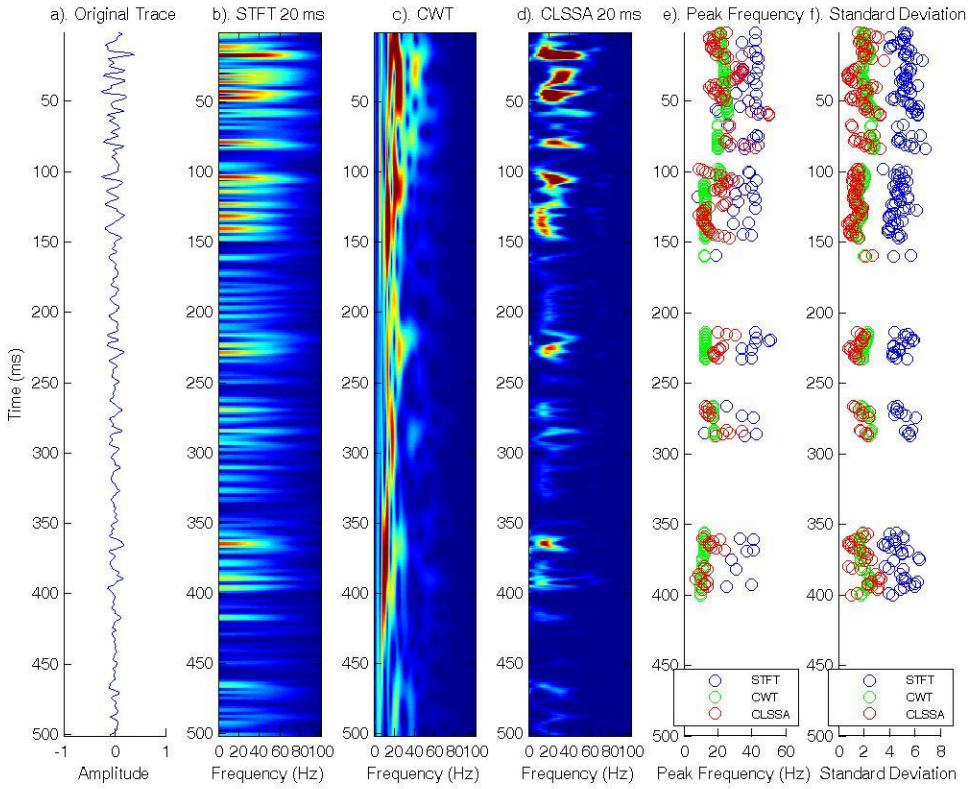

Figure 23). Down-dip real data trace with spectral decomposition and associated attributes (down-dip brine is at approximately t = 365 ms). Plots show (a) the original synthetic trace, (b) the 20 ms window STFT result, (c) the CWT result, (d) the 20 ms window single iteration CLSSA (N_i = 3) result, (e) thresholded peak frequencies where amplitude is greater than 2 percent of maximum amplitude and DC peak frequencies are excluded, and (f) thresholded amplitude-weighted standard deviations where amplitude is greater than 2 percent of maximum amplitude.

4.2. Turbidite bright spot 3D example

We apply the methods studied in this paper to a Gulf of Mexico seismic dataset that images a leveed turbidite channel. The data show a shale-filled turbidite with bright spot overbank deposits that are producing reservoirs. An amplitude extraction on the turbidite horizon is shown in Figure 24. The large-scale stratigraphic feature masks many smaller features that can potentially be revealed using spectral decomposition.

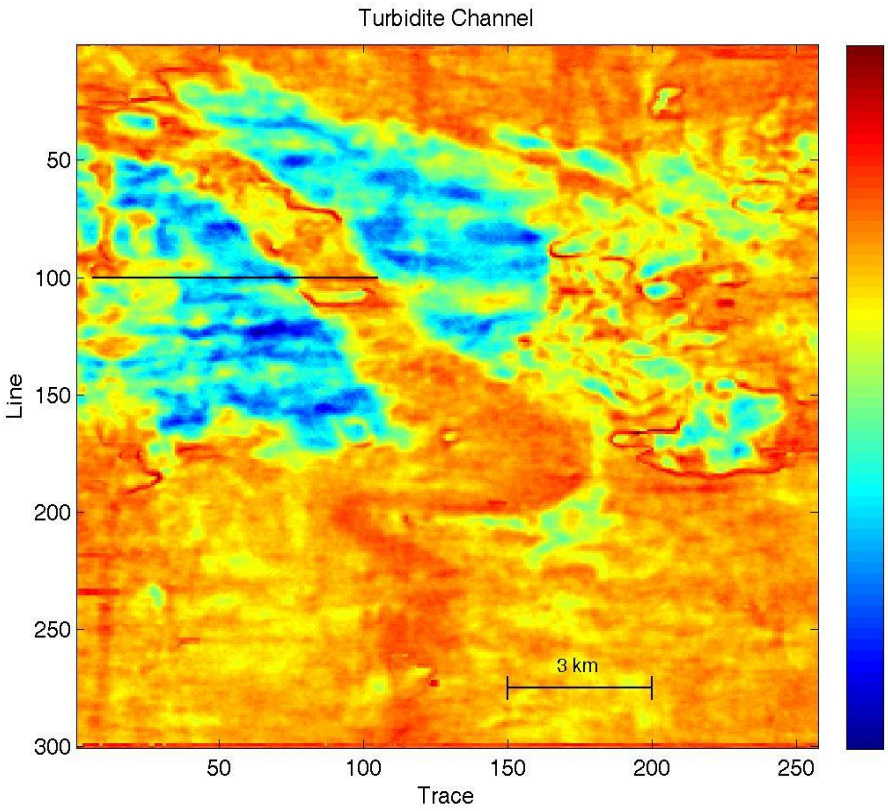

Figure 24). Amplitude on horizon of a leveed turbidite channel system from a Gulf of Mexico dataset. Black line shows the location of vertical sections in figures 25-34.

Figure 25 shows the original data with a prominent brightspot overbank deposit and CWT isofrequency vertical sections along the black section line shown in Figure 24. To illustrate variability in the spectrum, we display spectral components from 5 to 35 Hz with a 10 Hz frequency increment. The CWT shows major variation in temporal resolution across the spectrum as expected. Because window length is directly proportional to frequency for the CWT, a step from 5 Hz to 15 Hz imples a 3 fold shift in temporal resolution. This effect is observed in the plots. Furthermore, as frequency increases, progressively thinner sections of the overbank deposit are highlighted by the

CWT. Figure 26 yields another look at the channel response. We pick a horizon (Figure 26a) across a trough of the channel in order to further understand the local response relative to adjacent strata. The spectrum is computed at each location along the horizon and plotted in the trace number vs frequency panel (Figure 26b). Again, lower frequencies highlight thicker parts of the overbank deposit, and the spectral response migrates outward with increasing frequency. Figure 26c shows a plot of correlations among frequency components, and illustrates the strength of the CWT in terms of frequency discrimination. Low frequencies are strongly independent, and frequency discrimination gradually deteriorates to the upper limits of the spectrum. Overall, the CWT is a good tool for interpreting the frequency (but not temporal) characteristics of the channel response.

Figures 27-28 show the result computed with the 20 ms STFT. In Figure 27, Amplitude energy is spread across the spectrum and outside the wavelet band, and the frequency components show markedly less variability than the CWT from the low to high end of the spectrum. We infer that this lack of discrimination is related to the low frequency resolution of the very short STFT (df=1/20 ms=50 Hz). In order to further study this phenomenon, we look to Figure 28. Visually, we note strong homogeneity across the spectrum on the trace number-frequency panel, which is further quantified in the component correlation plot (Figure 28c). Clearly, frequency components are highly correlated across the spectrum, and the very short 20 ms window does not provide adequate spectral resolution for any type of quantitative interpretation.

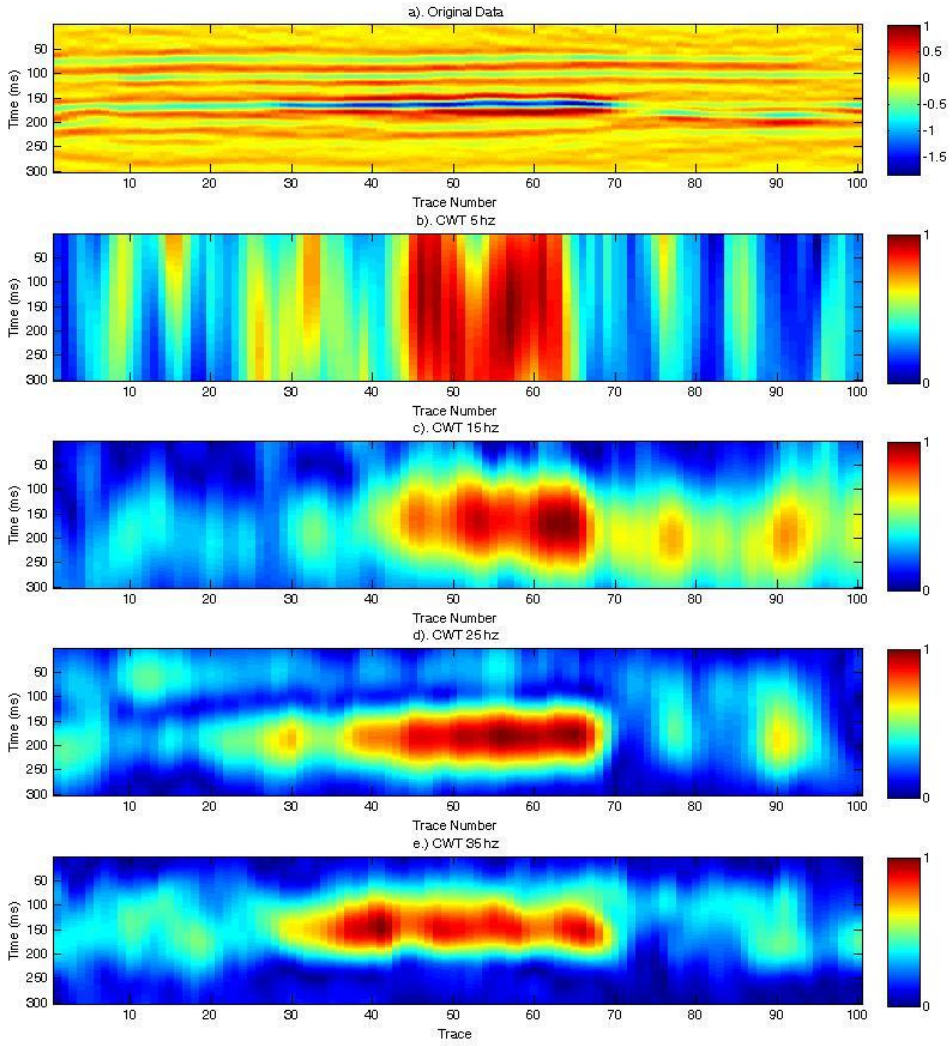

Figure 25). Original seismic data and CWT vertical isofrequency sections through the black section line show in Figure 24. Plots show the (a) vertical seismic section, (b) 5 Hz section output, (c) 15 Hz section output, (d) 25 Hz section output , and (e) 35 Hz section output. At low frequencies, the CWT simply integrates the channel with surrounding amplitude information and the thicker section of the overbank deposit is preferentially highlighted. Higher frequencies emphasize progressively thinner sections of the overbank deposit.

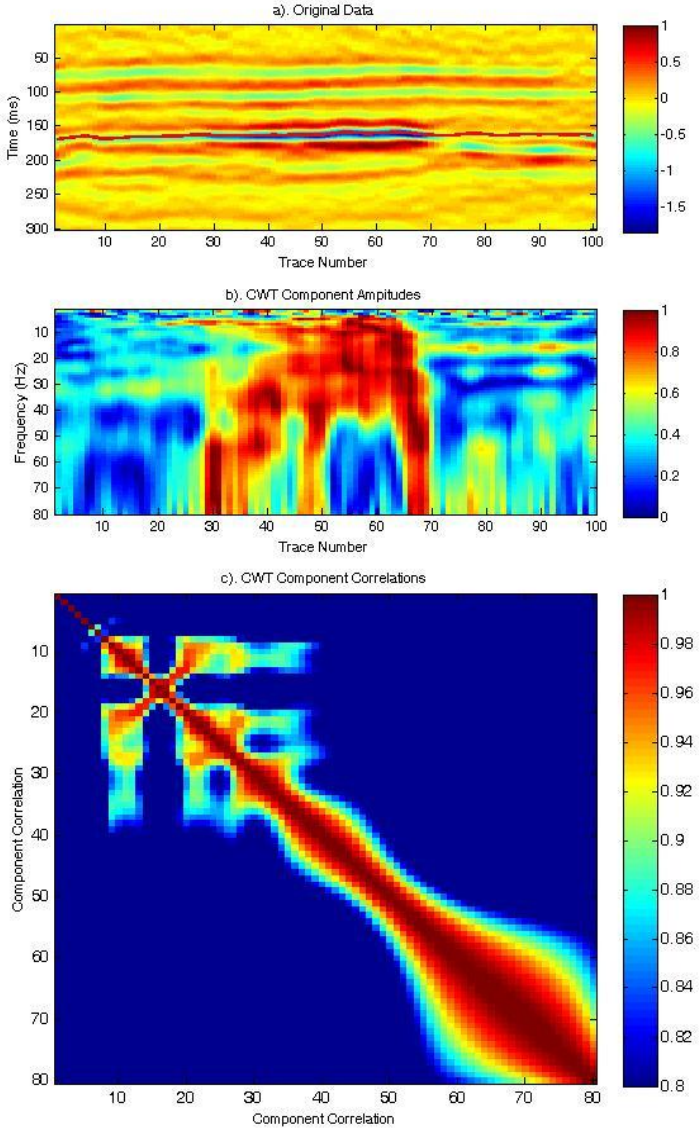

Figure 26). Seismic data section and CWT spectrum through the black section line shown in Figure 24. Plots show the (a) vertical seismic section with picked horizon, (b) frequency panel up to 60 Hz (high limit of the seismic data band) on the horizon, and (c) component correlation matrix for the CWT components plotted in (b). The horizon is picked along a trough, and the frequency panel is extracted on the horizon. Amplitude energy is largely restricted to the wavelet band for the CWT. Frequency components are well-resolved (low correlation) at low frequencies and frequency discrimination decreases as frequency increases.

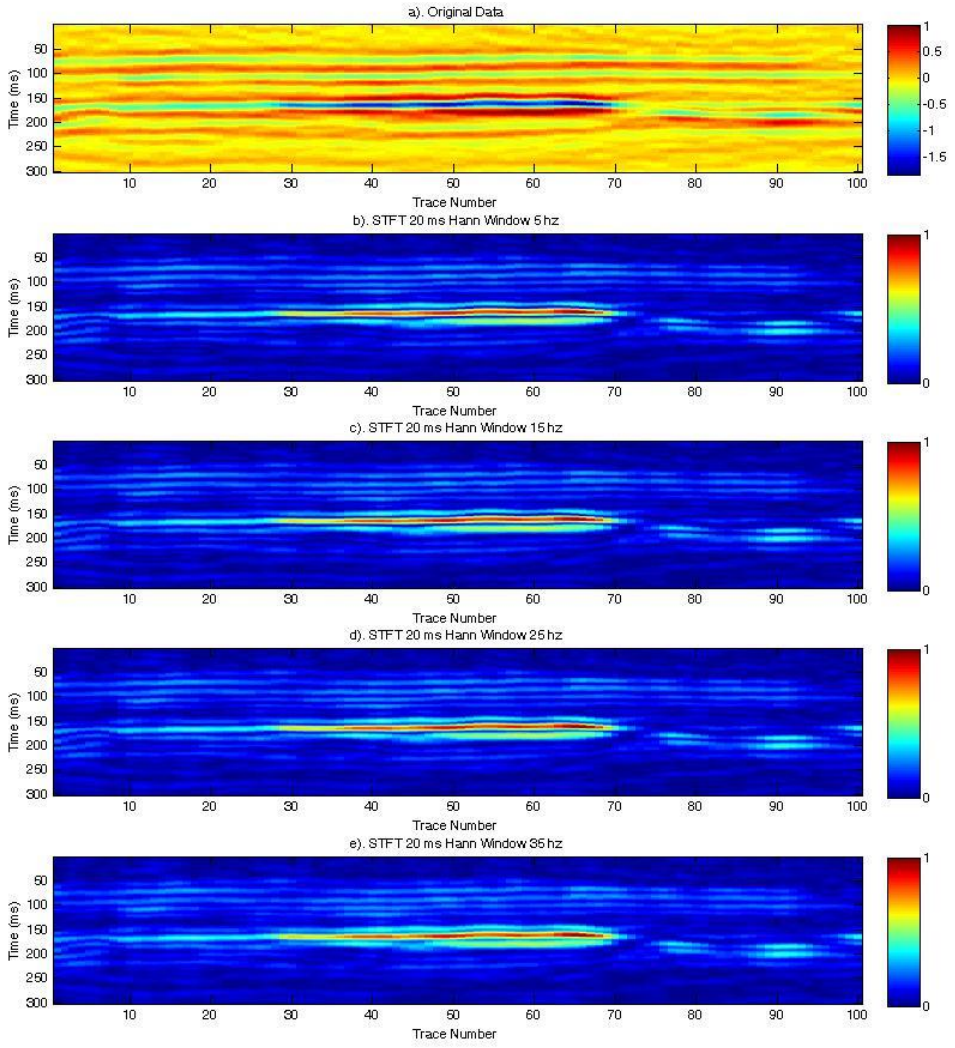

Figure 27). Original seismic data and 20 ms STFT vertical isofrequency sections through the black section line show in Figure 24. Plots show the (a) vertical seismic section, (b) 5 Hz section output, (c) 15 Hz section output, (d) 25 Hz section output , and (e) 35 Hz section output. The frequency sections show low variation as a function of frequency, a consequence of poor frequency resolution.

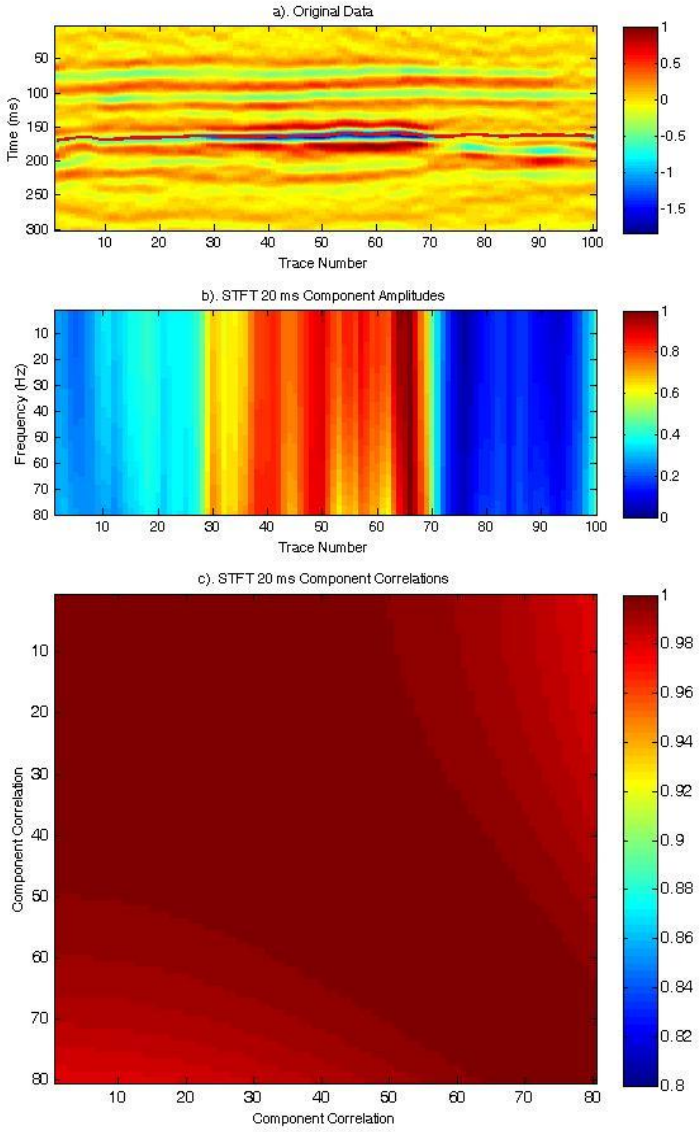

Figure 28). Seismic data section and 20 ms STFT spectrum through the black section line shown in Figure 24. Plots show the (a) vertical seismic section with picked horizon, (b) frequency panel up to 60 Hz (high limit of the seismic data band) on the horizon, and (c) component correlation matrix for the 20 ms STFT components plotted in (b). The horizon is picked along a trough, and the frequency panel is extracted on the horizon. Amplitude energy is spread across the spectrum and outside the wavelet band (Figure 28b). Frequency components are very poorly resolved across the spectrum (Figure 28c), which corresponds to the lack of frequency discrimination observed in Figure 27.

Figures 29-30 show the result computed with the 20 ms CLSSA (Ni=1, α_F=.001). In Figure 29, there are significant differences between 5 Hz and 15 Hz, while at higher frequencies, for example 25 Hz and 35 Hz, differences appear much less significant. As previously discussed, CLSSA preferentially incorporates low frequency information in the window due to the Hilbert transform operator. Thus, even for a very short window (in this case 20 ms), a high level of low frequency discrimination is achieved. Also, note that at higher frequencies, spreading amplitude lobes appear that could correspond to thinner sections of the overbank deposit. These are not distinct on the CWT or 20 ms STFT results. Figure 30b captures heightened spectral variability at low frequencies, and Figure 30c component correlation matrix illustrates the preferential spectral resolution at low frequencies.

Figures 31-32 show the result computed with the 40 ms STFT. In Figure 31, Amplitude energy is spread across the spectrum and outside the wavelet band, although this spreading effect is less pronounced than with the 20 ms STFT. For this window length, spectral resolution is doubled over the 20 ms STFT, and variation is observed across the spectrum. However, the tuned peaks visible on the 20 ms CLSSA (Ni=1, α_F=.001) are not obvious on the 40 ms STFT. The component correlation matrix (Figure 32) confirms significantly greater frequency discrimination than the 20 ms STFT and slightly poorer than the 20 ms CLSSA (Ni=1, α_F=.001) at high frequencies.

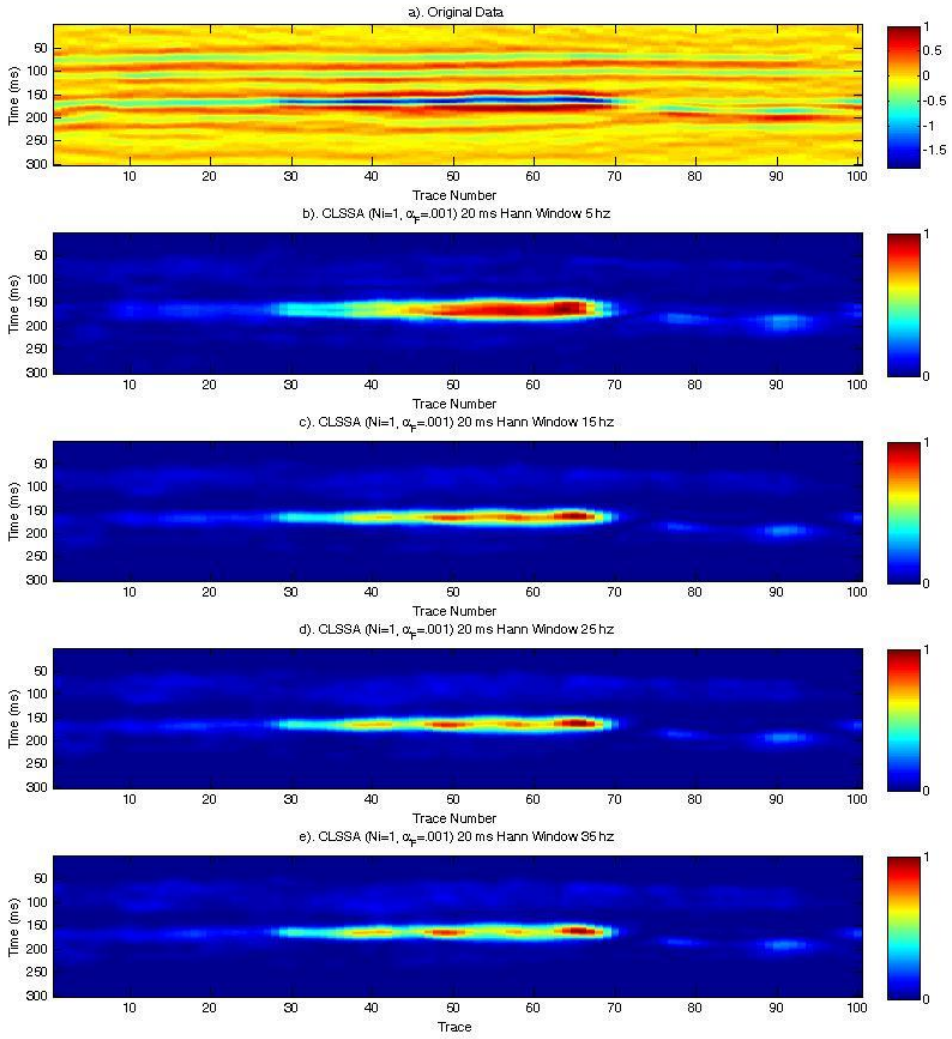

Figure 29). Original seismic data and 20 ms CLSSA (Ni=1, α_F=.001) vertical isofrequency sections through the black section line show in Figure 24. Plots show the (a) vertical seismic section, (b) 5 Hz section output, (c) 15 Hz section output, (d) 25 Hz section output , and (e) 35 Hz section output. The frequency sections show variability as a function of frequency at low frequencies, which diminishes at high frequencies. Spreading amplitude peaks not obvious on the 20 m STFT are seen at high frequencies, indicating thickness variation.

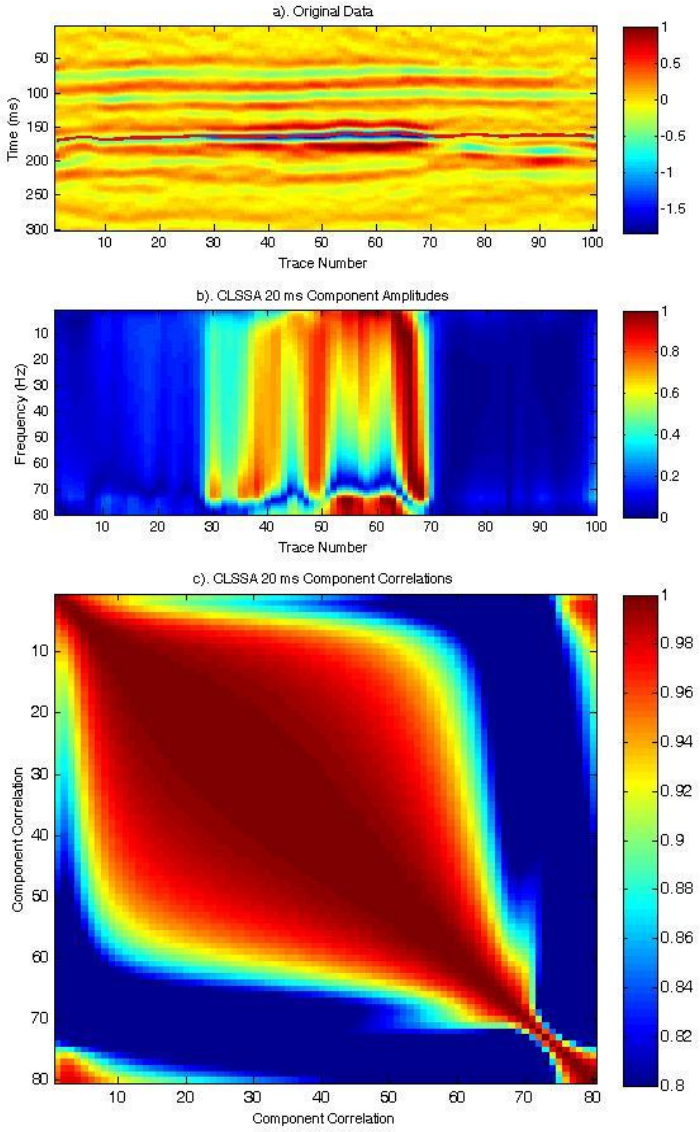

Figure 30). Seismic data section and 20 ms CLSSA (Ni=1, α_F=.001) spectrum through the black line shown in Figure 24. Plots show the (a) vertical seismic section with picked horizon, (b) frequency panel up to 60 Hz (high limit of the seismic data band) on the horizon, and (c) component correlation matrix for the 20 ms CLSSA (Ni=1, α_F=.001) components plotted in (b). The horizon is picked along a trough, and the frequency panel is extracted on the horizon. The low frequency discrimination/high frequency lack of discrimination noted in Figure 29 is observed in the frequency panels and the correlation component plots.

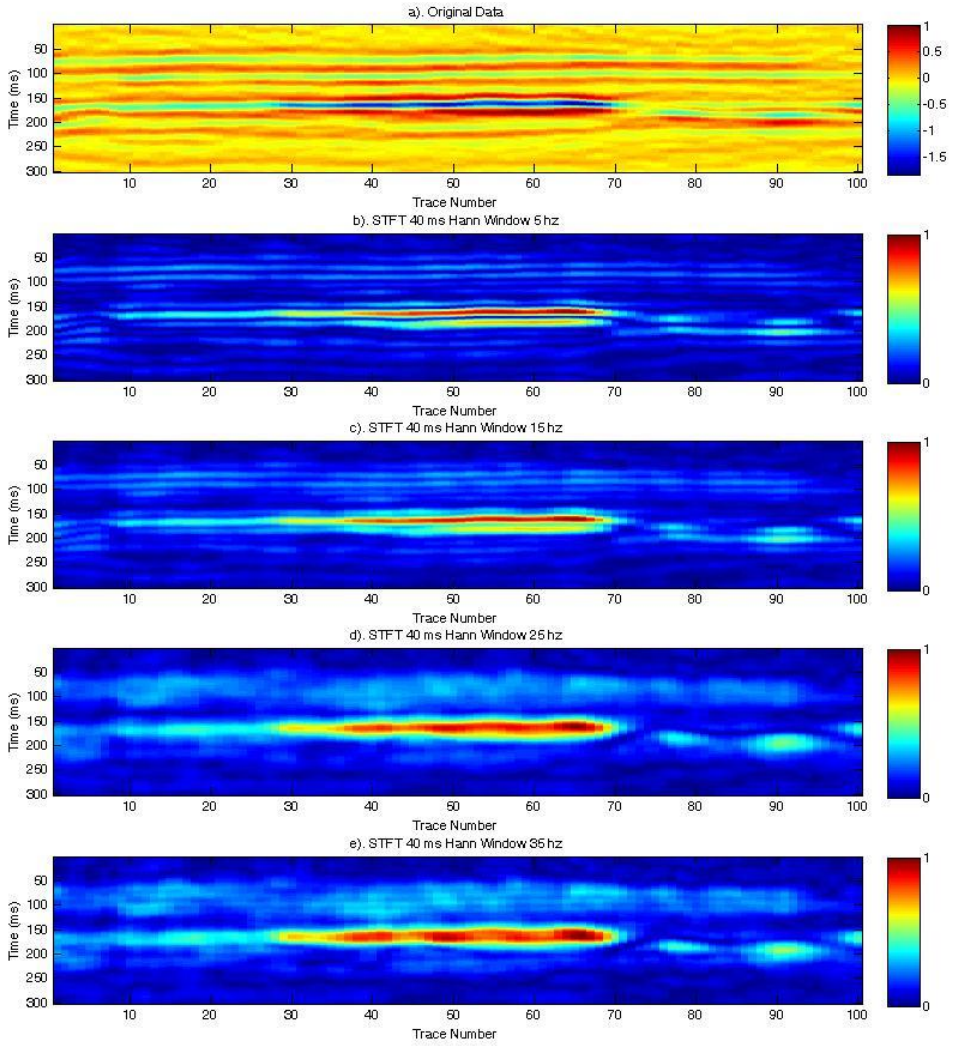

Figure 31). Original seismic data and 40 ms STFT vertical isofrequency sections through the black section line show in Figure 24. Plots show the (a) vertical seismic section, (b) 5 Hz section output, (c) 15 Hz section output, (d) 25 Hz section output , and (e) 35 Hz section output. The frequency sections show significantly greater variability as a function of frequency across the spectrum than the 20 ms STFT result.

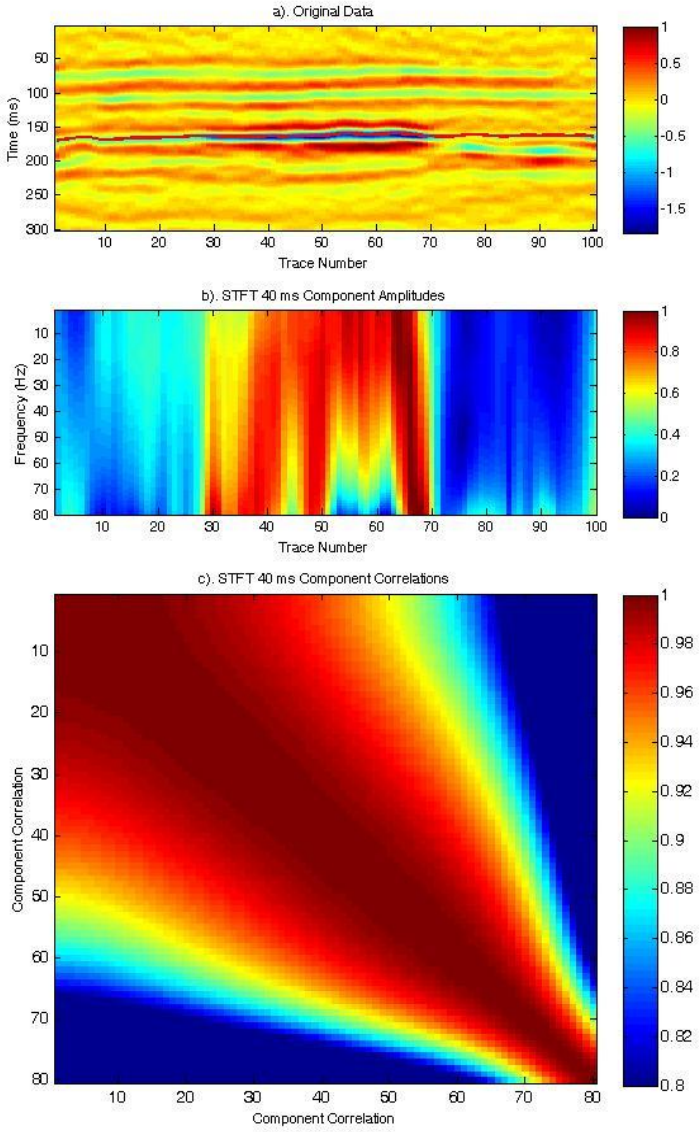

Figure 32). Seismic data section and 40 ms STFT spectrum through the black line shown in Figure 24. Plots show the (a) vertical seismic section with picked horizon, (b) frequency panel up to 60 Hz (high limit of the seismic data band) on the horizon, and (c) component correlation matrix for the 40 ms STFT components plotted in (b). The horizon is picked along a trough, and the frequency panel is extracted on the horizon. Amplitude energy is spread across the spectrum and outside the wavelet band. The component correlation matrix confirms significantly greater frequency discrimination than the 20 ms STFT and poorer than the 20 ms CLSSA (Ni=1, α_F=.001), especially at low frequencies.

Figures 33-34 show the result computed with the 40 ms CLSSA (Ni=1, α_F=.001). There are significant differences across the spectrum (including high frequencies), indicating improved spectral resolution over previous examples. Figure 34b captures heightened spectral variability, and Figure 34c component correlation matrix illustrates significant improvement in resolution over the 40 ms STFT, particularly at low frequencies.

Figure 35 shows several spectral decomposition peak frequency results on the horizon shown in Figure 24. The turbidite channel is not interpretable on the CWT result due to interference with neighboring events (poor temporal resolution). The 20 ms CLSSA result shows slightly more detail than the 20 ms STFT result, which gravitates toward very high frequency components due to the lack of spectral resolution. df=1/20ms=50 Hz, so 50 Hz is the first non-zero spectral component. A 40 ms window is needed in order to capture adequate frequency detail of the channel. Because the results are strongly biased toward the 25 Hz component for the 40 ms STFT, the peak frequencies of the channel fall within the background, and the channel is not captured by the 40 ms STFT. By contrast, the CLSSA result shows useful frequency details that are used to map channel thickness variation. Figure 36 illustrates the corresponding thickness variation maps for each method. For an odd dipole pair, the thickness is computed in ms by $1/(2*f_{peak})$, where f_{peak} is peak frequency.

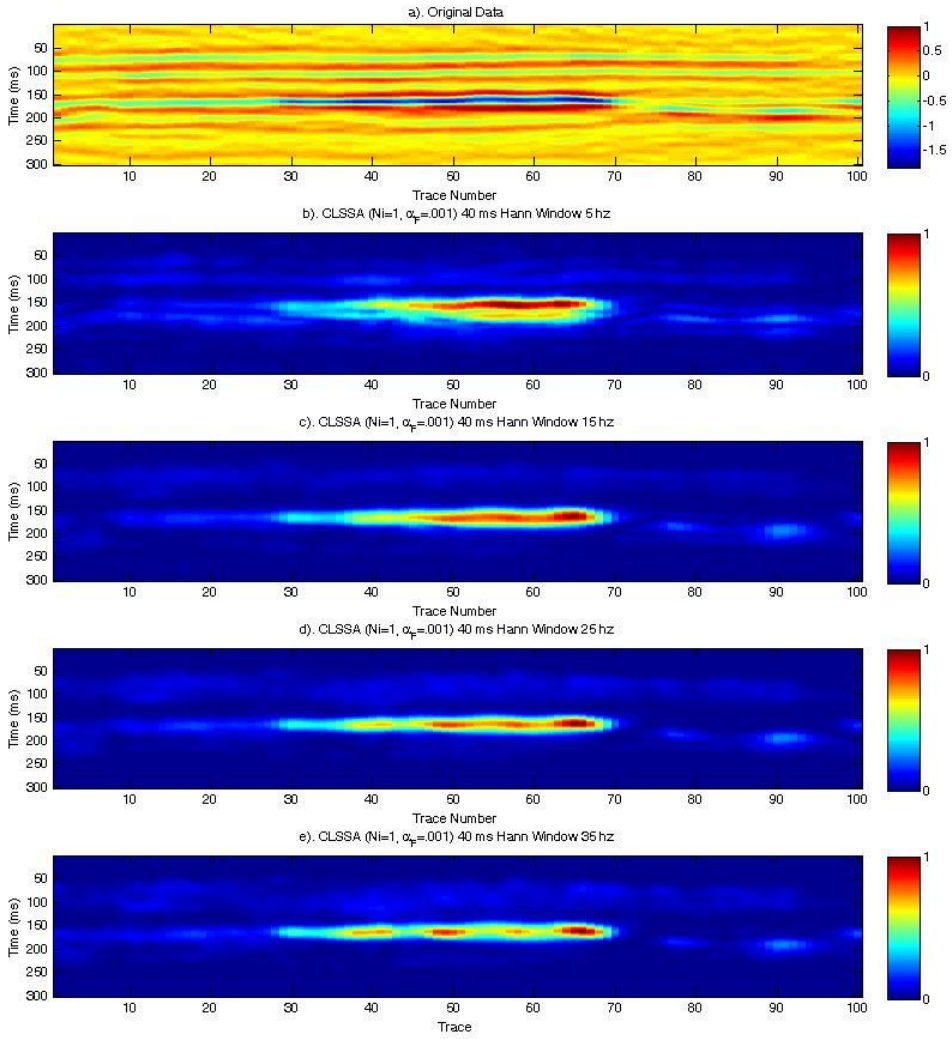

Figure 33). Original seismic data and 40 ms CLSSA (Ni=1, α_F=.001) vertical isofrequency sections through the black line show in Figure 24. Plots show the (a) vertical seismic section, (b) 5 Hz section output, (c) 15 Hz section output, (d) 25 Hz section output , and (e) 35 Hz section output. As compared to preceeding examples, the frequency sections show stronger variability across the spectrum.

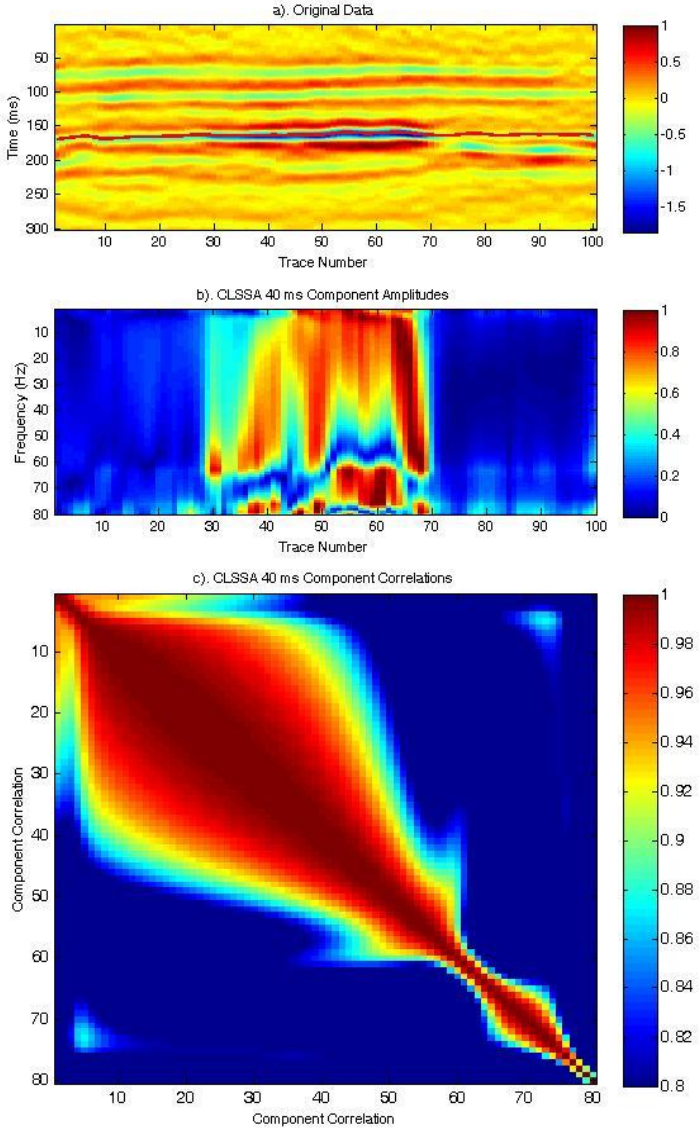

Figure 34). Seismic data section and 40 ms CLSSA (Ni=1, α_F=.001) spectrum through the black section line shown in Figure 24. Plots show the (a) vertical seismic section with picked horizon, (b) frequency panel up to 60 Hz (high limit of the seismic data band) on the horizon, and (c) component correlation matrix for the 40 ms CLSSA (Ni=1, α_F=.001) components plotted in (b). The horizon is picked along a trough, and the frequency panel is extracted on the horizon. As compared to previous examples, amplitude spectrum energy is compacted and the component correlation matrix confirms superior frequency discrimination and recognition of the wavelet bandwidth.

Figure 37 shows spectral decomposition peak amplitude results corresponding to the peak frequency results in Figure 35 on the horizon shown in Figure 24. The turbidite channel is not easily interpretable on the CWT result due to interference with neighboring events (i.e. channel amplitudes are suppressed). For each method, the results are comparable for 20 ms and 40 ms windows. The CLSSA results show improved delineation of the channel features over the STFT due to significantly increased dynamic range.

4.3. Barnett 3D Example

A second dataset comprises the combined processed Harris and Gleason 3D surveys in Hamilton County, Texas, which totals approximately 88.28 square miles of 3D data. The Gleason 3D survey data were acquired in 2005, and the Harris 3D survey data were acquired in 2006. Hamilton County is located in the Fort Worth Basin, which is an important petroleum system that is normally faulted against the Muenster Arch to the North and East. The primary reservoir is the Barnett, a dense, organic-rich shale gas reservoir covering more than 5,000 square miles and stretching across 20 counties in North Central Texas. Some experts believe the Barnett Shale could contain more than an estimated 40 trillion cubic feet of natural gas, making it one of the largest onshore natural gas fields in the United States. The Barnett is a “tight” gas reservoir, meaning that gas is not easily extracted by conventional means. In some locations, the Barnett is divided into upper and lower members of the Forestburg Limestone. In the Barnett, producers have observed a correlation between thickness and hydrocarbon

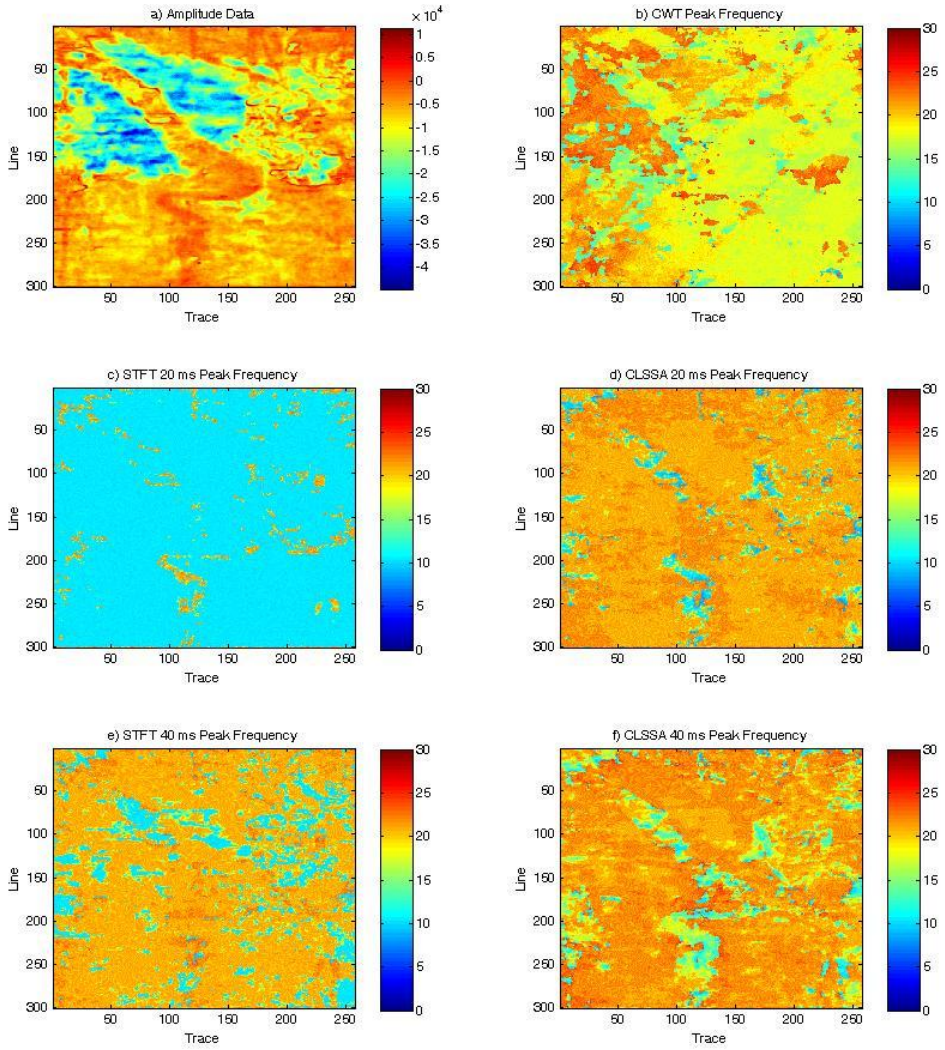

Figure 35). Spectral decomposition peak frequency results on a horizon picked on a turbidite channel. Plots show (a) amplitude extraction on the original horizon, (b) CWT peak frequency extraction, (c) 20 ms STFT peak frequency extraction, (d) 20 ms CLSSA (Ni=1, α_F=.001) peak frequency extraction, (e) 40 ms STFT peak frequency extraction, and (f) 40 ms CLSSA (Ni=1, α_F=.001) peak frequency extraction. The turbidite channel is not interpretable on the CWT result due to interference with neighboring events. While the 20 ms CLSSA result shows slightly more detail than the 20 ms STFT result, a 40 ms window is needed in order to capture subtle detail. Because the results are strongly biased toward the 25 Hz component for the 40 ms STFT, the peak frequency analysis does not capture the channel as an anomaly.

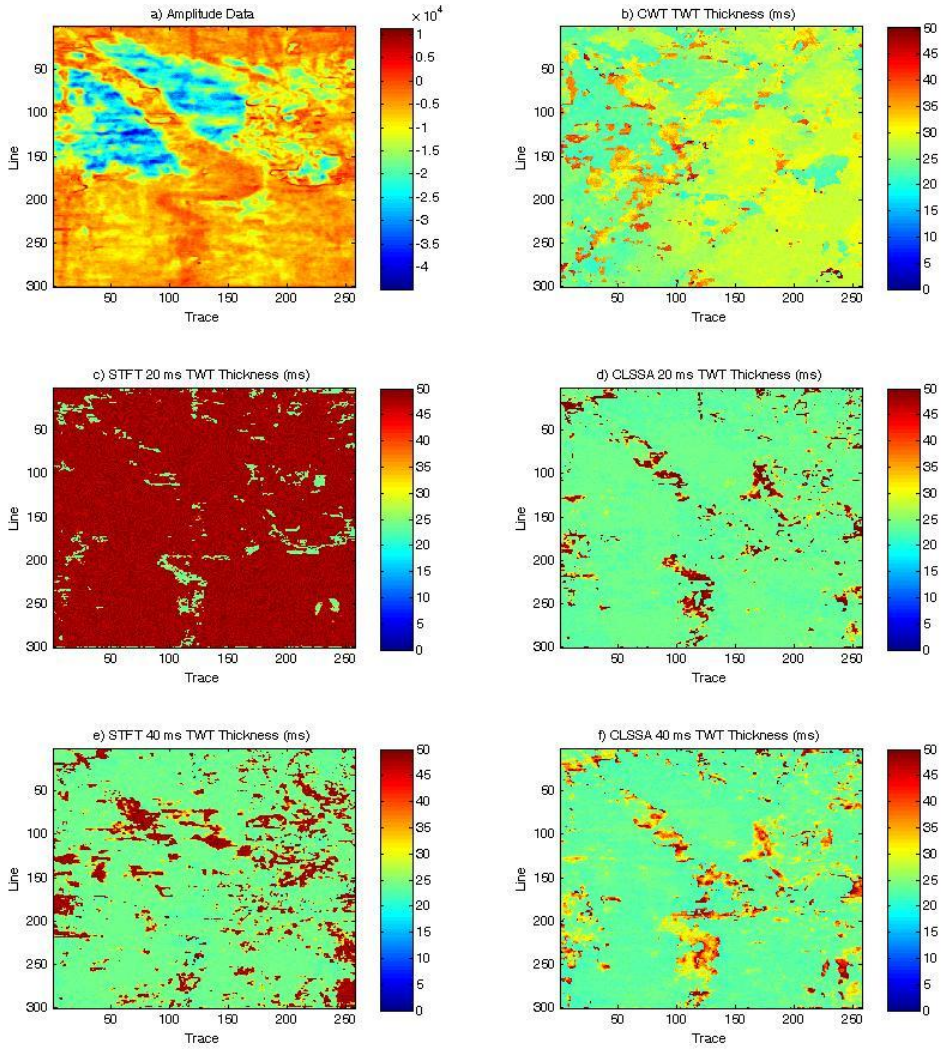

Figure 36). Spectral decomposition two-way time thickness calculation on a horizon picked on a turbidite channel. Plots show (a) amplitude extraction on the original horizon, (b) CWT thickness calculation, (c) 20 ms STFT thickness calculation, (d) 20 ms CLSSA (Ni=1, αF=.001) thickness calculation, (e) 40 ms STFT thickness calculation, and (f) 40 ms CLSSA (Ni=1, αF=.001) thickness calculation. The turbidite channel is not interpretable on the CWT result due to interference with neighboring events. Thickness variation is best highlighted on the 40 ms CLSSA map.

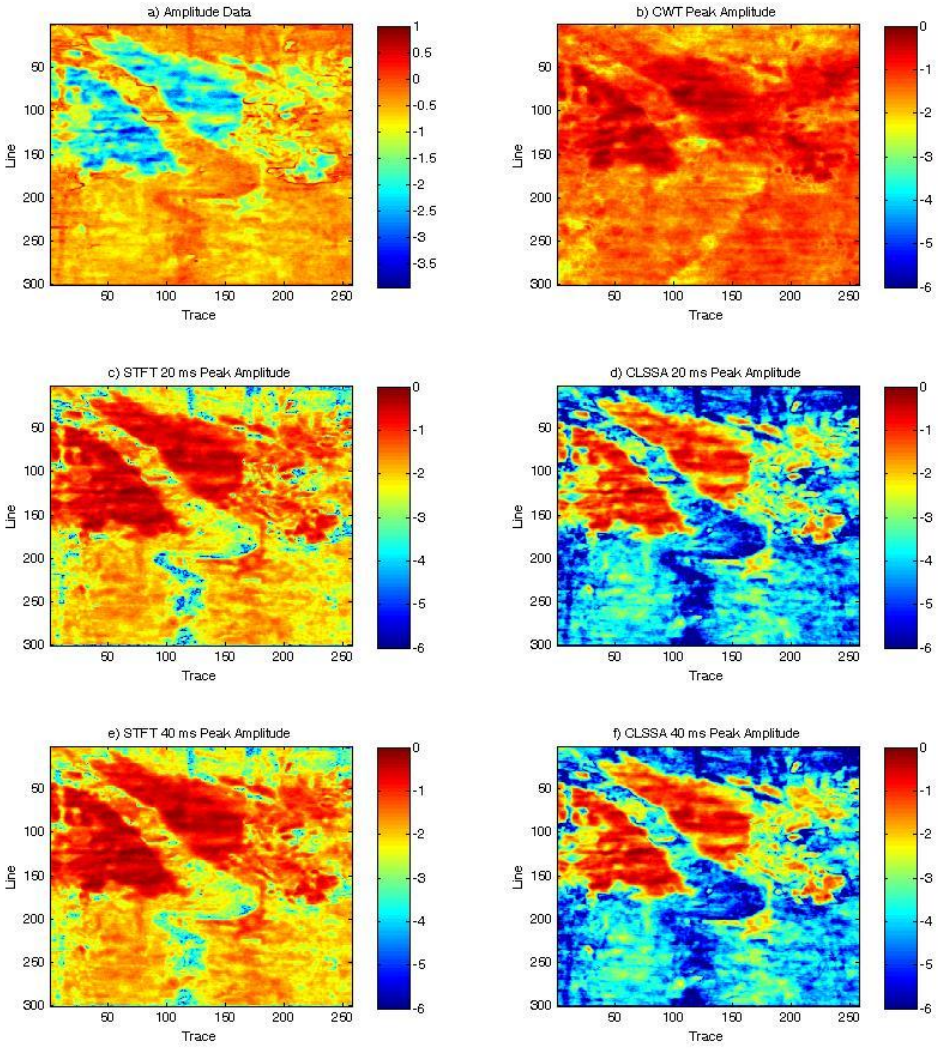

Figure 37). Spectral decomposition peak amplitude results on a horizon picked on a turbidite channel. Plots show (a) amplitude extraction on the original horizon, (b) CWT peak amplitude extraction, (c) 20 ms STFT peak amplitude extraction, (d) 20 ms CLSSA (Ni=1, α_F=.001) peak amplitude extraction, (e) 40 ms STFT peak amplitude extraction, and (f) 40 ms CLSSA (Ni=1, α_F=.001) peak amplitude extraction. The turbidite channel is not easily interpretable on the CWT result due to interference with neighboring events. For each method, the results are comparable for 20 ms and 40 ms windows. The CLSSA results show improved delineation of the channel features over the STFT due to significantly increased dynamic range.

productivity. According to Bruner and Smosna (2011), wells that encounter faults and/or karst tend to be less productive, while wells that intersect natural fractures tend to produce more gas. The overlying Marble Falls Formation (Pennsylvanian) is primarily limestone, and the underlying Ellenburger Formation (Ordovician) comprises porous dolomite and limestone. Water migrates from the Ellenburger into the Barnett by fault conduits.

Figure 38a shows data amplitude on a time slice at 750 ms. A vertical cross section A-B (black line) though the data and possible fault locations (black arrows) are also indicated. In Figure 38b, the interpreted locations of antithetic slump features at the top of the Barnett potentially linking to underlying fault systems in the Ellenberger are indicated by black arrows. The black horizontal line shows the location of the time slice plotted in Figure 38a.

Figure 39 shows a comparison of the original data amplitude to the amplitudes extracted from the spectral decomposition results on the time slice (t=750 ms), including the STFT 40 ms 20 Hz map, CWT 20 Hz map, and CLSSA (Ni=1, α_F=.001) 40 ms 20 Hz map. White arrows indicate an interpretation of the fault locations using CLSSA. The faults can be approximately inferred with difficulty on the original data map. On the STFT result, the linear features are overwhelmed by noise, possibly smeared from other portions of the spectrum. While there is some evidence of a linear disruption on the CWT, the results also fail to clearly highlight the fault trends. By contrast, CLSSA clearly indicates fault trends not obvious on the other maps.

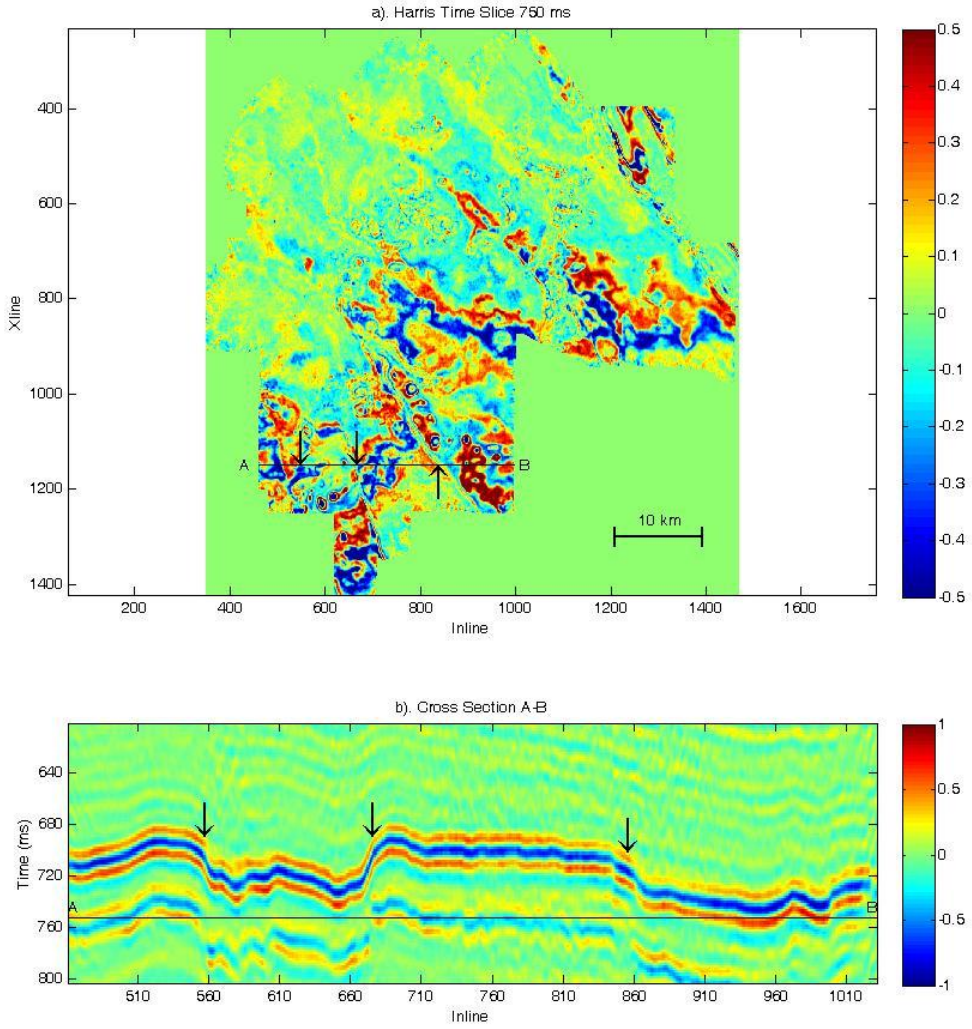

Figure 38). Marathon Harris dataset time slice and vertical section map. Plots show: (a) amplitude on a time slice through the seismic data at 750 ms and location of cross section A-B (black line) though several faults and (b) vertical section A-B though faults. Black arrows indicate locations of interpreted faults.

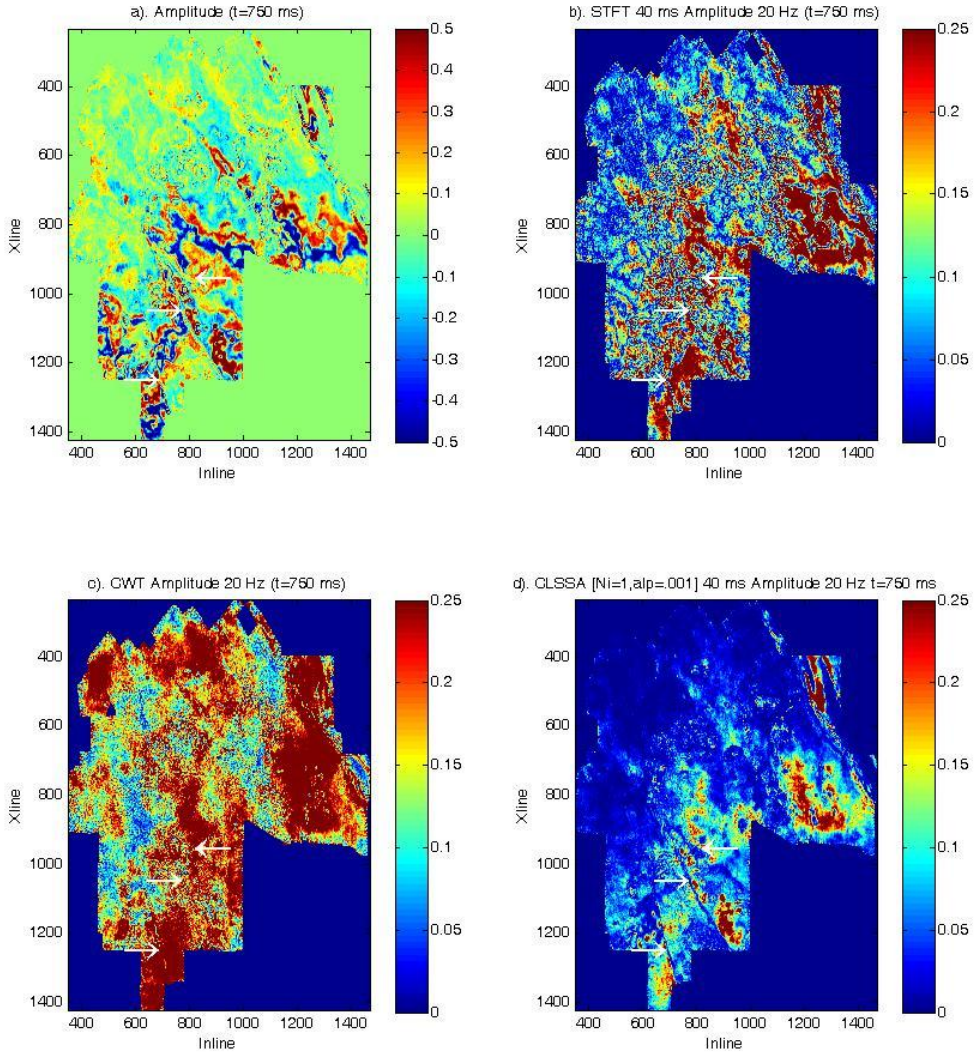

Figure 39). Marathon Harris dataset original data amplitude and 20 Hz spectral decomposition amplitudes on a time slice at 750 ms (see Figure 38). Plots show: (a) original data amplitude on the time slice, (b) 40 ms STFT 20 Hz amplitude on the time slice, (c) CWT 20 Hz amplitude on the time slice, and (d) 40 ms CLSSA (Ni=1, α_F=.001) 20 Hz amplitude on the time slice. Arrows indicate interpreted faults, which are most visible for interpretation on the CLSSA result.

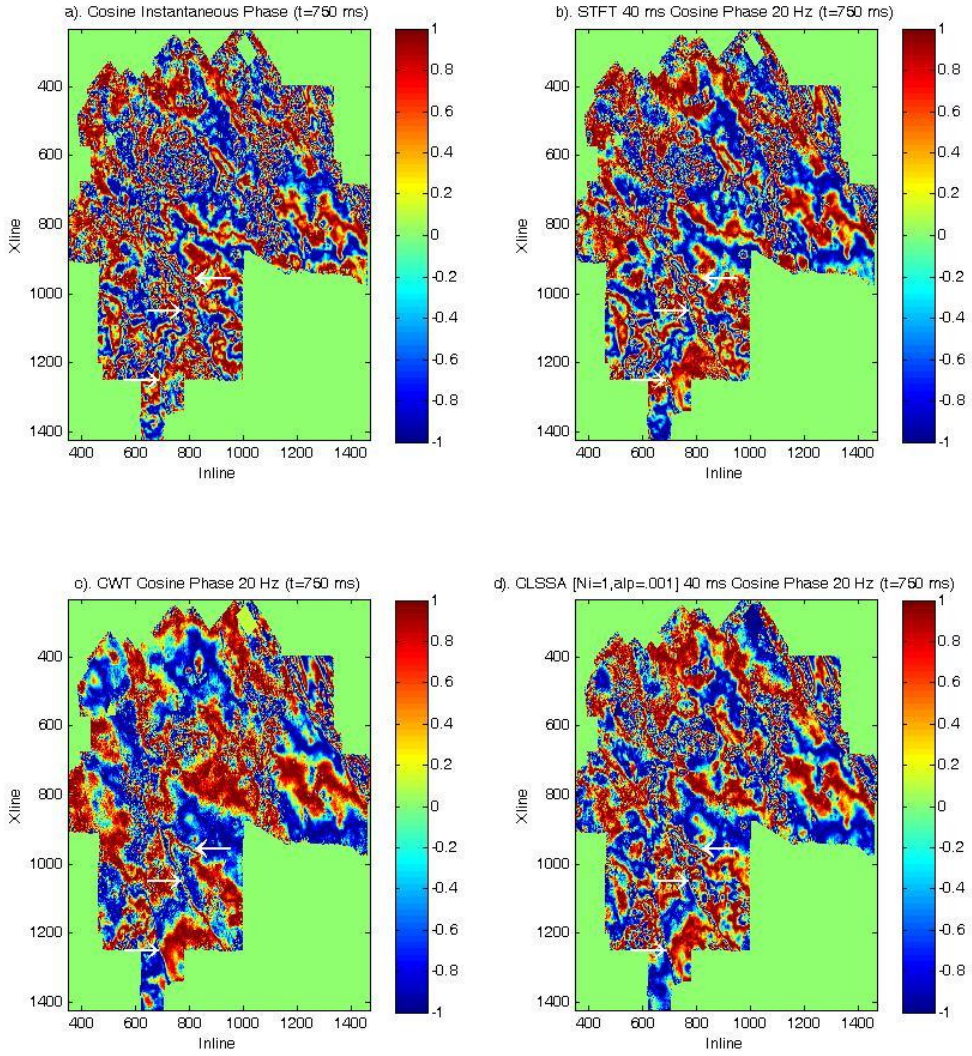

Figure 40). Marathon Harris dataset original data instantaneous phase and 20 Hz spectral decomposition phase on a time slice at 750 ms (see Figure 38). Plots show: (a) original data instantaneous phase on the time slice, (b) 40 ms STFT 20 Hz phase on the time slice, (c) CWT 20 Hz phase on the time slice, and (d) 40 ms CLSSA (Ni=1, α_F=.001) 20 Hz phase on the time slice. Arrows indicate interpreted faults.

Figure 40 shows phase plots on the same time slice. For comparison, the instantaneous phase on the original data is plotted in Figure 40a. Phase plots for each method show slightly different features, although the similarities among them are greater than on the amplitude maps.

5. DISCUSSION

Our modeling and real data spectral decomposition results show noteworthy improvement in resolution that follows from the application of fundamental principles of Fourier theory discussed in this paper. In order to generate valid time-frequency signal decompositions representative of the data within the window, rather than the windowed data, application of the Fourier Transform requires that the basis sinusoids be orthogonal. Generally, Fourier theory is to this day commonly applied using implicit analog assumptions, while the signals themselves have evolved to digital. Practitioners have learned to understand and deal with the consequences of windowing; however, in digital applications, it is not necessary to assume that the off-diagonal terms of the normal equations are zero, as the Fourier Transform implicitly does. Windowing effects can be mitigated by incorporating *a priori* information. For short windows, the STFT produces a set of sparse, evenly spaced spectral coefficients, resulting in dilution of spectral information content. Instead of being projected onto the continuous frequency domain, energy is restricted to discrete frequencies, resulting in distortion. Furthermore, there is no *a priori* information incorporated into the STFT formulation to favor resolution of the seismic band of interest.

With the development of modern computational science and inverse theory, these limitations of the STFT are surmountable. Instead of independently cross-correlating the signal with each orthogonal basis, we solve the normal equations with non-zero off-diagonal terms, thereby significantly reducing spectral component leakage. To do so robustly requires constraints, and our CLSSA formulation readily incorporates such constraints. Thus, the inversion for frequency coefficients can be formulated by including *a priori* knowledge of the signals through $\boldsymbol{W}_m$.

The complex trace effectively lengthens the window according to frequency. The Hilbert transform operator incorporates more information from outside the window at low frequencies than at high frequencies. In this sense, the complex CLSSA can be considered as having a frequency-dependent window. More importantly, the complex trace permits the use of infinitesimally short windows. For example, in the limit we can use just one sample window. In that case, CLSSA will simply produce instantaneous phase and frequency of one equivalent sinusoidal function.

The results of applying CLSSA to waveform models and real data traces validate the theoretical improvement in spectral resolution, and the hypothesis that the time-frequency product limitation can be improved over conventional methods. An additional benefit of the CLSSA method is that it does not require even sampling of the data in time or space, and can therefore be readily applied to a variety of seismic and non-seismic processing, inversion, and analysis problems. For example, the method could be extended to 2D spatial Fourier transforms, as irregular spatial sampling is

common, or to improve aperture resolution. Furthermore, the method could be applied to variable sampled data in the time domain for a variety of signal types. It is inferred that different types of signals will exhibit spectral-statistical characteristics that can be exploited by inversion formulations tailored to these characteristics. However, further modeling and case studies on seismic data are required to better understand the potential applications in identification and interpretation of geological features of interest.

There are a variety of avenues for future research aimed at furthering the CLSSA method: improved inversion algorithms, combination of window types and lengths, better use of STFT and CWT results as constraints, handling the DC problem better etc. We have attempted to show the promise of the CLSSA approach; however a number of complete case study comparisons to STFT, CWT, and other methods etc. will be needed before definitive conclusions can be drawn.

Whether or not one is convinced that CLSSA spectra are superior to those obtained using the CWT or STFT, the simple fact that the results are different is significant. Time-frequency analysis is non-unique, and there is no correct answer. A different valid answer may prove to be a useful addition to multi-attribute analysis in a given circumstance.

6. CONCLUSIONS

We developed an inversion-based algorithm for computing the spectral decomposition of seismic data using CLSSA and tested the algorithm on synthetic

waveforms and real data. The decomposition is performed by the inversion of a basis of truncated sinusoidal kernels in a short time window. The method results in a time-frequency analysis with frequency resolution and time-frequency product superior to the STFT and the CWT. The classical spectral smoothing inherent to Fourier spectral analysis of windowed data is reduced or eliminated, thereby allowing analysis of the spectral characteristics of composite reflections within windows significantly shorter than those used in previously published spectral decomposition work. We demonstrated the efficacy of the CLSSA transform on 6 synthetic waveforms. For sinusoidal waveforms, spectral content was resolved nearly perfectly using CLSSA, while frequency smearing effects dominated the STFT and CWT spectra. Ricker wavelet spectra were also well resolved within the short window. In all cases, the CLSSA spectra had narrower bandwidth than the CWT and STFT spectra due to the absence or reduction of window smearing effects. The real data trace frequency panel results showed improvements in the spectral analysis of a bright spot, including narrower frequency spectra and more detailed peak frequency trends potentially related to geological characteristics. Application of the method to seismic datasets containing a turbidite channel system and the Barnett shale resulted in the tentative interpretation of architectural elements not observed using conventional spectral decomposition methods.

7. REFERENCES

Bracewell, R., 1986, The Fourier Transform and its applications: McGraw-Hill Publishing Company.

Bruner, K. R., and R. Smosna, A comparative study of the Mississippian Barnett Shale, Fort Worth Basin, and Devonian Marcellus Shale, Appalachian Basin. URS Corp. National Energy Technology Lab., US DOE. 2011.

Castagna, J. P., S. Sun, and R. W. Siegfried, 2003, Instantaneous spectral analysis: Detection of low-frequency shadows associated with hydrocarbons: The Leading Edge, **22**, 120–127.

Chakraborty, A., and D. Okaya, 1995, Frequency-time decomposition of seismic data using wavelet-based methods: Geophysics, **60**, 1906-1916.

Daubechies, I., R. DeVore, M. Fornasier, and C. S. Güntürk, 2008, Iteratively reweighted least squares minimization of sparse recovery: Communication on Pure and Applied Mathematics, **63**, 1-38.

Fahmy, W.A., G. Matteucci, J. Parks, M. Matheney, and J. Zhang, 2008, Extending the limits of technology to explore below the DHI floor; successful application of spectral decomposition to delineate DHI's previously unseen on seismic data: SEG Expanded Abstracts, **27**, 408-412.

Grossmann, A., R. K. Martinet, and J. Morlet, 1989, Reading and understanding continuous wavelet transforms, *in* Combes, J. M., A. Grossmann, and P. Tchamitchian, eds., Wavelets: time-frequency methods and phase space: Springer-Verlag, 2-20.

Last B.J. and K. Kubik, 1983, Compact gravity inversion: Geophysics, **48**, 713-721.

Liu, J. and K.J. Marfurt, 2007, Instantaneous spectral attributes to detect channels: Geophysics, **72**, 23-31.

Mallat, S., 1999, A wavelet tour of signal processing, 2nd ed.: Academic Press Inc.

Marfurt, K. J., and R. L. Kirlin, 2001, Narrow-band spectral analysis and thin-bed tuning: Geophysics, **66**, 1274–1283.

Marquardt, D. W., 1963, An algorithm for least-squares estimation of nonlinear parameters: Journal of the Society of Industrial and Applied Mathematics, 431-441.

Matos, M. C., O. Davogusto, K. Zhang, and K. J. Marfurt, 2010, Continuous wavelet transform phase residues applied to detect stratigraphic discontinuities: 80th Annual International Meeting, SEG, Expanded Abstracts, 1494-1499.

Oldenburg, D. W., 1976, Calculation of Fourier transforms by the Backus-Gilbert method: Geophysical Journal of the Royal Astronomical Society, **44**, 413-431.

Partyka, G. A., J. A. Gridley, and J. A. Lopez, 1999, Interpretational aspects of spectral decomposition in reservoir characterization: The Leading Edge, **18**, 353–360.

Partyka, G. A., 2005, Spectral decomposition: SEG Distinguished Lecture, http://www.seg.org/education/lectures-courses/distinguished-lecturers/spring2005/partykaabstract.

Portniaguine, O., Image focusing and data compression in the solution of geophysical inverse problems, 1999: Ph.D. dissertation, University of Utah.

Portniaguine, O., and M.S. Zhdanov, 1998, Focusing geophysical inversion images: Geophysics, **64,** 874-887.

Portniaguine, O., and J. P. Castagna, 2004, Inverse spectral decomposition: 74th Annual International Meeting, SEG, Expanded Abstracts, 1786–1789.

Puryear, C. I., and J. P. Castagna, 2008, Layer-thickness determination and stratigraphic interpretation using spectral inversion: Theory and application: Geophysics, **73,** 37–48.

Puryear, C.I., S. Tai, J.P. Castagna, R. Masters, and F. Dwan, Comparison of frequency attributes from CWT and MPD spectral decompositions of a complex turbidite channel model, 78th Annual International Meeting, SEG, Expanded Abstracts, 393-397.

Sacchi, M. D., and T.J. Ulrych, 1996, Estimation of discrete Fourier transform, a linear inversion approach: Geophysics, **61**, 1128-1136.

Sinha, S., P. S. Routh, P. D. Anno, and J. P. Castagna, 2005, Spectral decomposition of seismic data with continuous wavelet transform: Geophysics, **70**, P19-P25.

Tikhonov, A. N., and V.Y. Arsenin, 1977, Solutions of ill-posed problems: V.H. Winston and Sons.

Vaníček, P., 1969, Approximate spectral analysis by least-squares fit: Astrophysics and Space Science, **4**, 387-391.

Widess, M., 1973, How thin is a thin bed?: Geophysics, **38**, 1176-1180.

Xu, S., Y. Zhang, D. Pham, and G. Lambaré, 2005, Antileakage Fourier transform of seismic data regularization: Geophysics, **70**, 87-95.

APPENDIX 1

LAYER THICKNESS DETERMINATION AND STRATIGRAPHIC INTERPRETATION USING SPECTRAL INVERSION:

THEORY AND APPLICATION

Charles I. Puryear[1] and John P. Castagna[1]

[1]University of Houston, Department of Geosciences, Houston, Texas

Email: cipuryear@hotmail.com; jcastagnaou@yahoo.com.

ABSTRACT

Spectral inversion is a seismic method that uses *a priori* information and spectral decomposition to improve images of thin layers whose thickness is below the tuning thickness. We formulate a method to invert frequency spectra for layer thickness and apply it to synthetic and real data using complex spectral analysis. We find that absolute layer thicknesses significantly below the seismic tuning thickness can be robustly determined in this fashion without amplitude calibration. We extend our method to encompass a generalized reflectivity series represented by a summation of impulse pairs. Application of our spectral inversion to seismic datasets from the Gulf of Mexico results in reliable well ties to seismic, accurate prediction of layer thickness to less than half the tuning thickness, and improved imaging of subtle stratigraphic features. Comparisons between well ties for spectrally inverted data and those for conventional seismic data illustrate the superior resolution of the former. A number of stratigraphic examples illustrate the various destructive effects of the wavelet, including creation of illusory geologic information, such as false stratigraphic truncations that are actually related to lateral changes in rock properties, and masking of geologic information, such as updip limits of thin layers. We conclude that data which are spectrally inverted on a trace-by-trace basis show greater bedding continuity than do the original seismic data, suggesting that wavelet sidelobe interference produces false bedding discontinuities.

INTRODUCTION

According to the Widess (1973) model, seismically thin layers below 1/8th of a wavelength in thickness cannot be resolved. However, such "thin" layers may be significant reservoirs or important flow units within reservoirs. Exploration and development geophysicists are frequently faced with the task of inferring layer thickness for layers such as these where the top and base of the layer cannot be distinctly mapped. Determination of layer properties for such seismically thin beds is consequently of great interest in both exploration and development applications. While tuning-thickness analysis based on the theory of Widess (1973) and Kallweit and Wood (1982) has been the method of choice for thickness mapping for several decades, Partyka et al. (1999), Partyka (2005), and Marfurt and Kirlin (2001) have demonstrated the effectiveness of spectral decomposition using the Discrete Fourier Transform as a thickness estimation tool. However, such methods have difficulty with thin layers if the seismic bandwidth is not sufficient to unambiguously identify the periodicity of spectral peaks and notches. This difficulty motivates the development of methods that do not require the precise identification of peaks and troughs within the seismic bandwidth.

Partyka (2005), Portniaguine and Castagna (2004 and 2005), Puryear (2006), Chopra et al, (2006a and 2006b), and Puryear and Castagna (2006) have shown that inversion of spectral decompositions for layer properties can be improved when reflection coefficients are simultaneously determined. The result is a sparse-reflectivity inversion that can be parameterized to provide robust layer thickness estimates. Such a

process is called *spectral inversion* and produces results that differ from conventional seismic inversion methods. In this paper, we discuss the basic theory of spectral inversion, develop a new spectral inversion algorithm, and show field examples of improved bed thickness determination and enhanced stratigraphic imaging that can be achieved with the process.

Widess model

The Widess (1973) model for thin-bed reflectivity teaches that the fundamental limit of seismic resolution is λ/8, where λ is the wavelength. Essentially, constructive wavelet interference and measured amplitude in the time domain peak at λ/4; the waveform shape and peak frequency continue to change somewhat as amplitude decreases to λ/8, at which point the waveform approximates the derivative of the seismic wavelet. As the layer thins below λ/8, the waveform does not change significantly, while amplitude steadily decreases as demonstrated in Figure A1. In this figure, amplitudes are obtained from the convolution of a 30 Hz Ricker wavelet with a wedge model. From this point of view, there are no means to differentiate between amplitude changes associated with reflection coefficient changes and thickness changes below λ/8, making this thickness a hard resolution limit for broadband analysis in the time domain. Worse yet, in the presence of noise and wavelet broadening, the transition between λ/4 and λ/8 is obscured, sometimes making λ/4 a practical limit of resolution. The key assumptions for the Widess model are that the half spaces above

and below the layer of interest have the same acoustic impedance and that the acoustic impedance of the thin layer is constant.

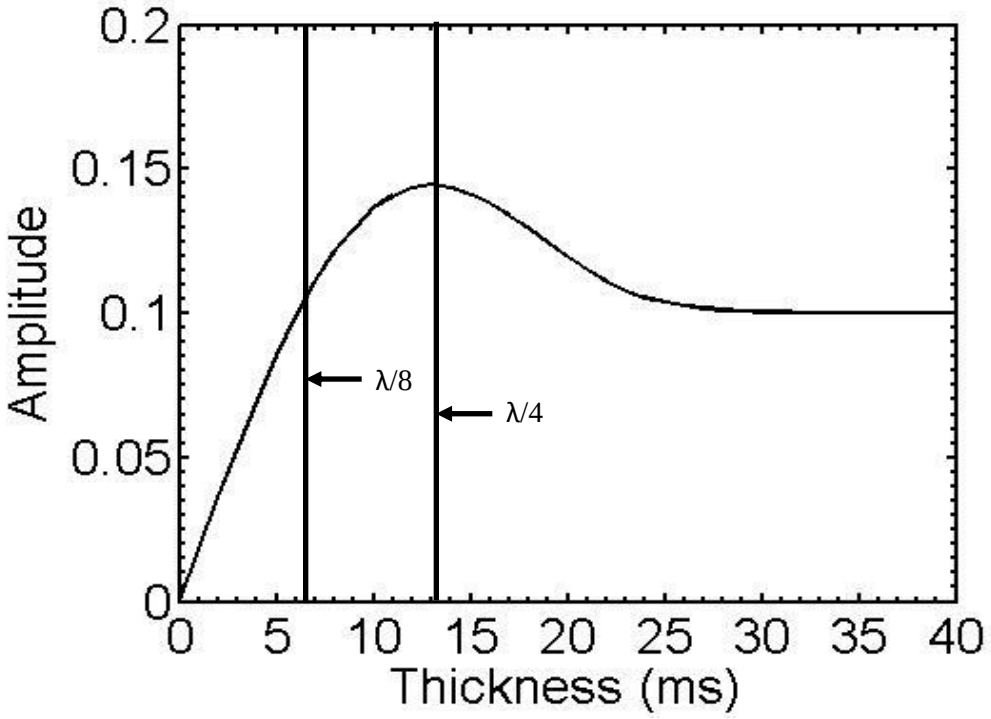

Figure A1. A plot of amplitude vs. thickness shows the increase in amplitude over background as the tuning thickness (λ/4) is approached. Below tuning, the amplitude rolls off nearly linearly, and the waveform approximates the derivative of the wavelet at λ/8.

Generalized reflectivity model

While the theory of Widess (1973) is valid when the assumptions are satisfied, nature rarely accommodates such strict theoretical provisions. The theory of spectral inversion is based on the realization that the Widess model for thin-bed reflectivity presupposes a reflectivity configuration that is actually a singularity in the continuum of possible reflection coefficient ratios. Any reflection coefficient pair can be decomposed

into even and odd components, the even components having equal magnitude and sign and the odd components having equal magnitude and opposite sign, as described by Castagna (2004) and Chopra et al. (2006). The identity is illustrated in Figure A2. The Widess model assumes that reflection coefficient pairs are perfectly odd, which can be a good approximation for certain target classes such as a sand layer encased in a shale matrix. However, the odd-reflectivity-pair assumption implies the worst possible resolution for thin beds. Even a small even component in the reflection coefficient pair can significantly increase the resolvability of a layer. The improvement in resolution results from the fact that the even component constructively interferes as thickness approaches zero, in contrast to the odd component, which destructively interferes. Thus, the even component is more robust against noise as thickness approaches zero (see Tirado, 2004).

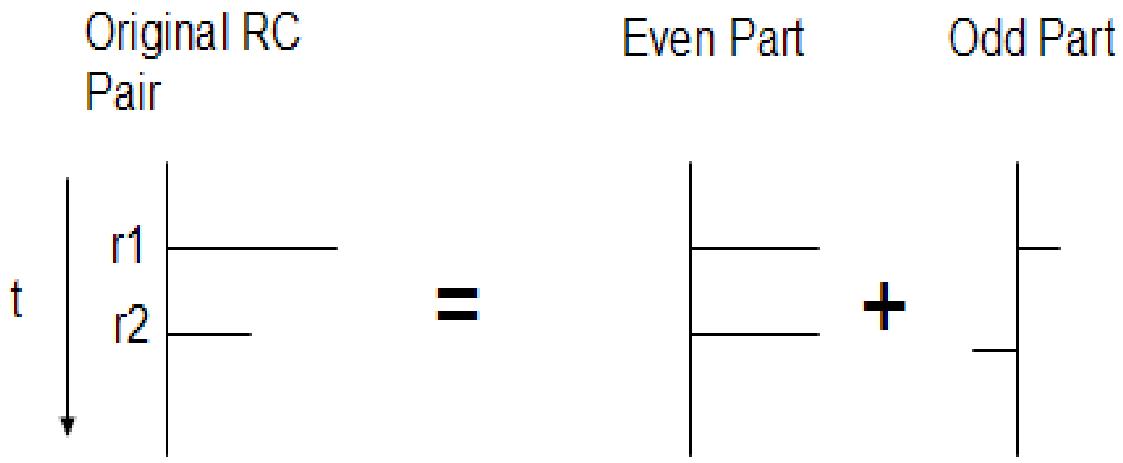

Figure A2. Any arbitrary pair of reflection coefficients r_1 and r_2 can be represented as the sum of even and odd components. The even components have the same magnitude and sign, and the odd components have the same magnitude and opposite sign.

We calculated peak frequency and peak amplitude from equations given by Chung and Lawton (1995). Figure A3a shows the effect of thinning on the peak frequency of a reflection coefficient pair with even and odd components. For the model, the total peak frequency increases with decreasing thickness and then returns to the peak frequency of the wavelet rather than that of the derivative of the wavelet as predicted by the Widess model. Interestingly, the total peak frequency shows significant and continuous change down to zero thickness. Likewise, the total peak amplitude (Figure A3b) does not approach zero with thickness as predicted by the Widess model. The example indicates that the reflection amplitude trend can show significant variation from the Widess curve (Figure A1) as the layer thickness approaches zero when the even component is nonzero. Thus, there is significant information below the Widess resolution limit that is not captured by traditional amplitude mapping techniques which assume equal and opposite reflection coefficients. Such examples of unequal reflection coefficients at top and base of a layer, which are the rule rather than the exception for most real-world seismic reflections events, reinforce the need for a more generalized approach to thin-bed amplitude analysis.

Based on the fact that the spacing between spectral peaks and notches is a deterministic function of layer thickness, our objective was to develop a new algorithm to invert reflectivity using the constant periodicity in the frequency domain. Our development started with the expression for an impulse pair in the time domain, from which we formulated a numerical algorithm using complex spectral analysis, and then

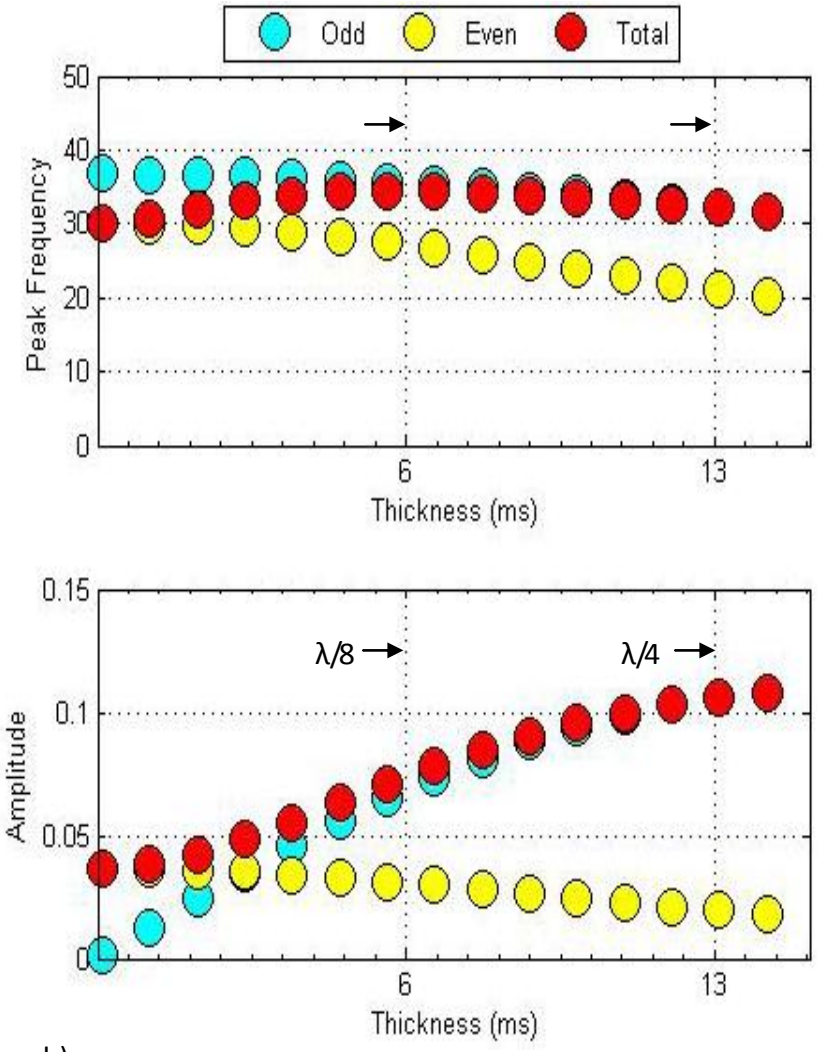

b).

Figure A3. The (a) peak frequency and (b) peak amplitude as a function of thickness for the even component, the odd component, and the total. There is (a) peak frequency information below the tuning thickness. Also, the (b) total peak amplitude approaches the even component amplitude below tuning. Layer model parameters are: r_1 = -.2, r_2 = .1, and f_0 = 30 Hz.

tested the algorithm on synthetic wedge models. We extended our development to multiple layers, and we tested our method on 3D seismic data from the Gulf of Mexico shelf, comparing seismic data, spectrally inverted seismic data, and well log data.

METHODS

Spectral inversion method

We apply windowed Fourier Transforms to several reflectivity models in order to generate the data for spectral inversion, and use complex spectral analysis to formulate the inversion algorithm. The algorithm described herein defines the inversion for reflectivity using the constant periodicity of the amplitude spectrum for a layer of a given thickness, taking advantage of the fact that the spacing between spectral peaks and notches is precisely the inverse of the layer thickness in the time domain (Partyka et al, 1999; Marfurt and Kirlin, 2001). Essentially, layer thickness can be robustly determined from a narrow band of frequencies with a high ratio of signal-to-noise. To prove this concept, note that the entire reflectivity spectrum for a single layer could be reconstructed from amplitudes at three frequencies in the absence of noise.

Beginning with the expression for an impulse pair in the time domain as expressed by Marfurt and Kirlin (2001) (Figure A4):

$$g(t) = r_1\delta(t - t_1)+r_2\delta(t - t_1 - T), \quad \text{(A1)}$$

where r_1 = top reflection coefficient, r_2 = base reflection coefficient, t = time sample, t_1 = time sample at top reflector, and T = layer thickness. Locating the analysis point at the center of the layer yields

$$g(t) = r_1\delta(t - T/2) + r_2\delta(t + T/2). \quad \text{(A2)}$$

Taking the Fourier transform of the shifted equation 2 gives

$$g(t, f) = r_1\exp(-i2\pi f\,[t + T/2]) + r_2\exp(-i2\pi f\,[t - T/2]), \quad \text{(A3)}$$

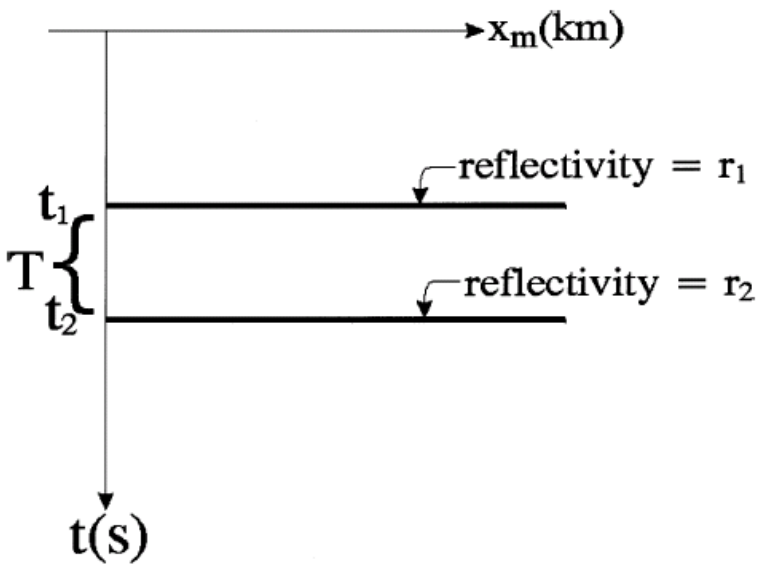

Figure A4. Two-layer reflectivity model (from Marfurt and Kirlin, 2001).

where f = frequency and g(f) = the complex spectrum. Simplifying using trigonometric identities and taking the real part yields

$$\mathrm{Re}[g(f)] = (2r_e)\cos(\pi f T), \tag{A4}$$

where r_e = the even component of the reflection coefficient pair.

Similarly, the imaginary part of the complex spectrum is

$$\mathrm{Im}[g(f)] = (2r_o)\sin(\pi f T), \tag{A5}$$

where r_o = the odd part of the reflection coefficient pair.

Plots for both the even and odd reflectivity spectra corresponding to equations A4 and A5 for a layer with thickness T = 10 ms and reflection coefficients r_1 = .2 and r_2 = .1 are shown in Figures A5a and A5b respectively. Note that while both even and odd spectra show the same notch period, the two are shifted by one-half of the frequency spacing. For the individual real and imaginary components, the constant period in the

spectrum is related to the symmetric location of the analysis point at the center of the layer. This placement effectively divides the reflection coefficient pair into perfectly odd and even components, thereby eliminating the phase variation for each. The effect of violating this condition is discussed in Appendix A1.

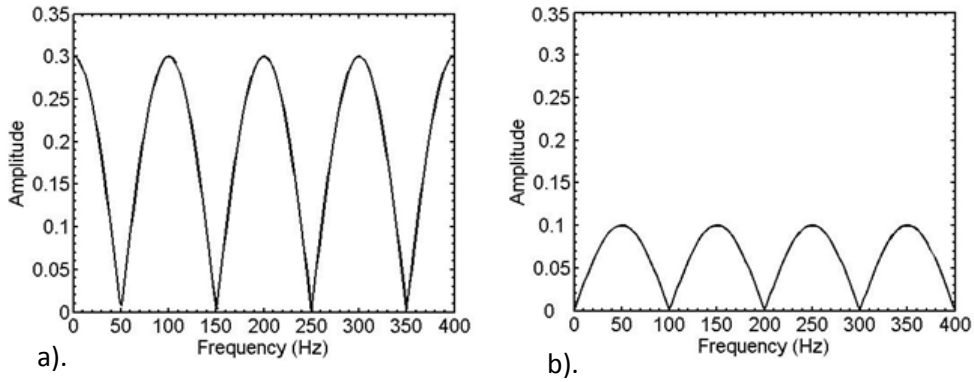

Figure A5. Amplitude vs. frequency plots for the (a) even components and the (b) odd components for the reflection coefficient pair r_1 = .2 and r_2 = .1. In this example, the even component is dominant.

In order to maintain constant periodicity in the spectrum while shifting the analysis point away from the layer center, we computed the modulus of the real and imaginary components of the spectrum, which is insensitive to phase. Beginning with general expressions for the real and imaginary time shifted spectra,

$$\mathrm{Im}[e^{2i\pi f\Delta t}g(f)] = 2r_o \sin(\pi fT)\cos(2\pi f\Delta t) + 2r_e \cos(\pi fT)\sin(2\pi f\Delta t) \quad \text{and} \quad \text{(A6)}$$

$$\mathrm{Re}[e^{2i\pi f\Delta t}g(f)] = 2r_e \cos(\pi fT)\cos(2\pi f\Delta t) - 2r_o \sin(\pi fT)\sin(2\pi f\Delta t), \quad \text{(A7)}$$

it can be shown (Appendix A2) that

$$O(t,k) = G(f)\frac{dG(f)}{df} + 2\pi Tk\sin(2\pi fT), \quad \text{(A8)}$$

where G(f) = amplitude magnitude as a function of frequency, $k = r_e^2 - r_o^2$, and O(t, k) is the cost function at each frequency. The solution to equation A8 occurs where the sum of cost functions O(t, k), evaluated at each frequency, is minimized over the range of frequencies within the analysis band. One data term exists at every sample frequency, so the performance of the method is determined by the signal-to noise ratio over a given analysis band (i.e. more frequencies with a high ratio of signal-to-noise yields a more stable and accurate inversion).

We found the global minimum of equation A8 for a given analysis band by searching physically reasonable model parameters k and T in two-parameter model space and minimizing the objective function as illustrated in Figure A6. While costly and impractical for more complicated cases, the global search method guarantees the avoidance of local minima for the single-layer case. The remaining model parameters are then determined by

$$r_o = \sqrt{\frac{G(f)^2}{4} - k\cos^2(\pi f T)}, \tag{A9}$$

$$r_e = \sqrt{k + r_o^2}, \text{ and} \tag{A10}$$

$$t_1 = \frac{1}{2i\pi f}\ln[\frac{g(f)}{r_1 + r_2 e^{2i\pi f T}}], \tag{A11}$$

where t_1 is the time sample at the top reflector r_1 and g(f) is the complex spectrum for the reflection coefficient pair. Equation A11 can be derived by taking the Fourier transform of equation A1 and solving for t_1. The reflection coefficients r_1 and r_2 can be

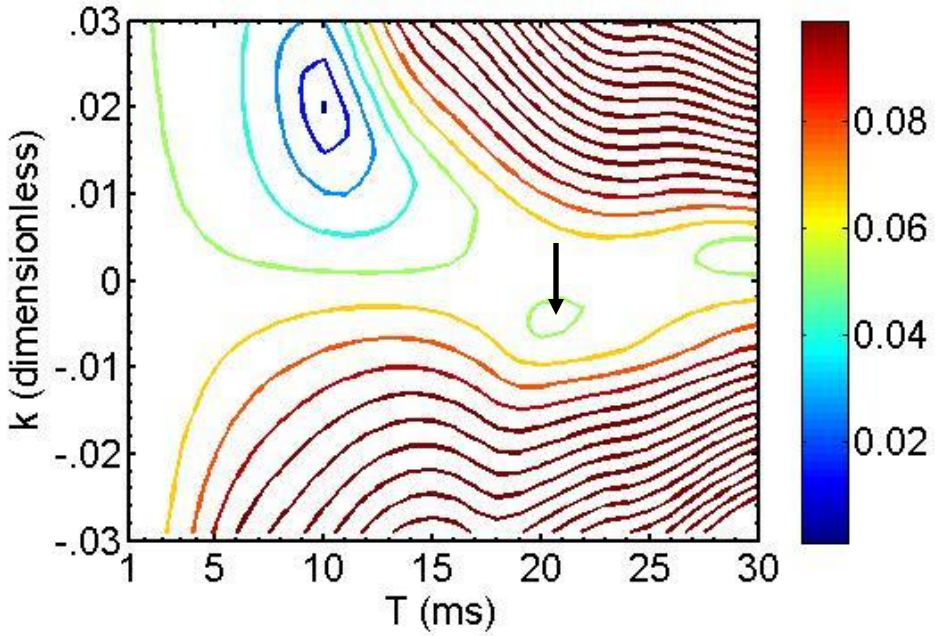

Figure A6. The difference or error function between the data and a range of model parameter pairs is calculated. The blue bullseye is the correct model solution (T = 10 ms, k = .02). A local minimum is shown by the black arrow.

recovered by recomposing the odd and even components of the pair calculated using equations A9 and A10**,** which is the reverse of the operation illustrated in Figure A2. Thus, it is straightforward to compute the remaining components of the layer reflectivity model from the initial parameters k and T. Note that although the derivation (Appendix B) of the algorithm assumes that the even reflectivity component is greater than the odd reflectivity component, the solution is the same for the antithetical assumption.

Modeling results

We tested the method by convolving a 30 Hz Ricker wavelet with reflection coefficient pairs having various ratios. We produced wedge models with 4 ms sampling

for a predominately odd reflection coefficient pair r_1 = -.2 and r_2 = .1, and a predominately even reflection coefficient pair r_1 = .2 and r_2 = .1. The tuning thickness of a thin bed model with a Ricker wavelet is given by Chung and Lawton (1995):

$$t_R = \frac{\sqrt{6}}{2\pi f_0}, \tag{A12}$$

where f_0 is the dominant wavelet frequency. For a 30 Hz Ricker wavelet, t_R = 13 ms. The convolution of the wavelet with the reflection coefficient pair in the time domain is equivalent to multiplication with the reflectivity spectrum in the frequency domain. The inversion performs perfectly in the absence of noise for layers of any thickness. In order to achieve a more realistic model, we added noise in the time domain; and we measured and controlled the noise level by computing the ratio of the area under the spectrum of the signal to that of the noise in the frequency domain. We tested the model with 1 percent and 5 percent noise levels. The forward modeling procedure is illustrated in Figure A7a.

The addition of noise causes instability in the inversion for very thin layers, partly because of the fact that the reflectivity spectrum approaches a flat spectrum as the layer thickness, T, approaches zero; we mitigated this problem by applying the arbitrary constraint -.03 < k < .03 to insure that the reflection coefficient strength could not exceed what is typically observed in seismograms. After Fourier transforming the time domain signal, we removed the wavelet overprint by dividing the magnitude of the amplitude of the seismic signal by that of the wavelet at each analysis frequency.

We tested the inversion at different noise levels while varying the analysis band and smoothing filter. These experiments showed that the optimal analysis band and the

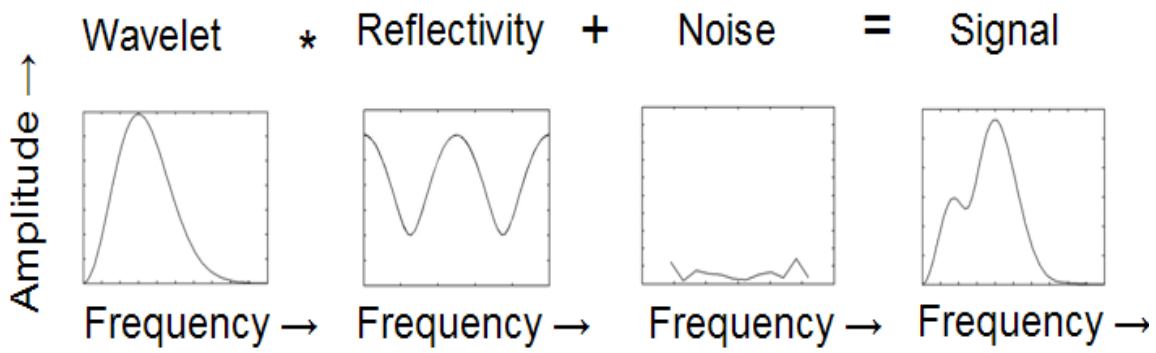

a).

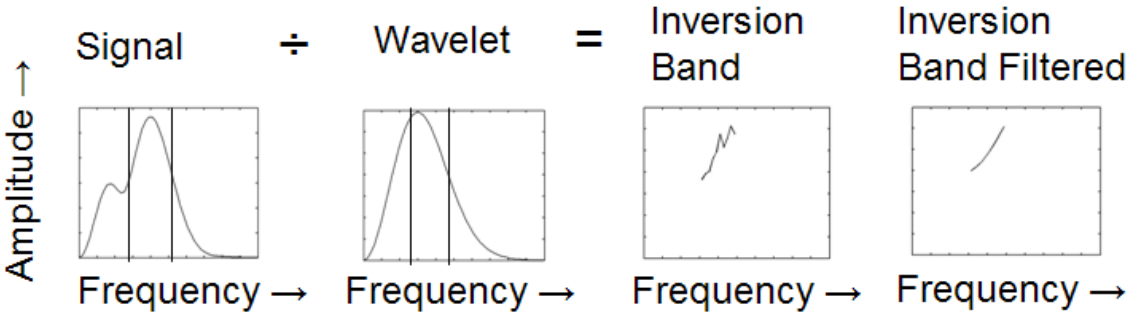

b).

Figure A7. The (a) forward model and (b) inverse model schemes used for the synthetic. The plots show magnitude of amplitude vs. frequency. In the (a) forward model, multiplication of the wavelet with the reflectivity spectrum and addition of noise in the frequency domain yields the seismic signal. In the (b) inverse model, division of the seismic signal by the wavelet in the frequency domain yields the noisy reflectivity band. Application of a smoothing filter produces the inversion band for input to the model.

optimal smoothing filter are determined by the noise level. We achieved optimal results for the 1 percent noise case using a 25 Hz bandwidth sampled at 2 Hz frequency increments and centered on the peak signal frequency. As the signal is corrupted by noise, it is necessary to narrow the bandwidth. For the 5 percent noise case, we

achieved optimal results with a 20 Hz bandwidth. Furthermore, more smoothing is required to stabilize the derivative operator as noise is added. The process resulting in the smoothed inversion band is illustrated in Figure A7b. We took derivatives of the magnitude of the amplitude with respect to frequency at each observation frequency sample using a first order central difference approximation. Finally, we multiplied the magnitude of the amplitude at each observation frequency by the derivative of the magnitude of the amplitude at that frequency and minimized the error between the model defined by equation A8 and the data for the range of frequencies within the analysis band (Figure A6).

We applied the inversion defined by equation A8 using a 256 ms window FFT for spectral decomposition to wedge models having predominately odd and even reflection coefficient pairs (Figures A8a and A8b). Figures A9a and A9b show the result of the inversion (black) compared with the true reflectivity model (green and red) for 1 percent and 5 percent levels of noise respectively for the predominately odd reflection coefficient pair, while Figures A10a and A10b show these results for the predominately even pair. The tuning thickness is represented by the vertical black line. We compared the 5 percent noise results with the corresponding amplitude mapping results (brown) using tuning analysis (see Widess, 1973 and Kallweit and Wood, 1982). The algorithm performs nearly perfectly for both configurations at 1 percent noise levels as expected, illustrating the principle that noiseless data would yield extremely high resolution. While the noise level is unrealistically low for most seismic data, the results highlight the

importance of meticulous noise suppression in acquisition and during processing. For thin layers, the results are useful far below tuning. For the 5 percent noise cases, the absolute error

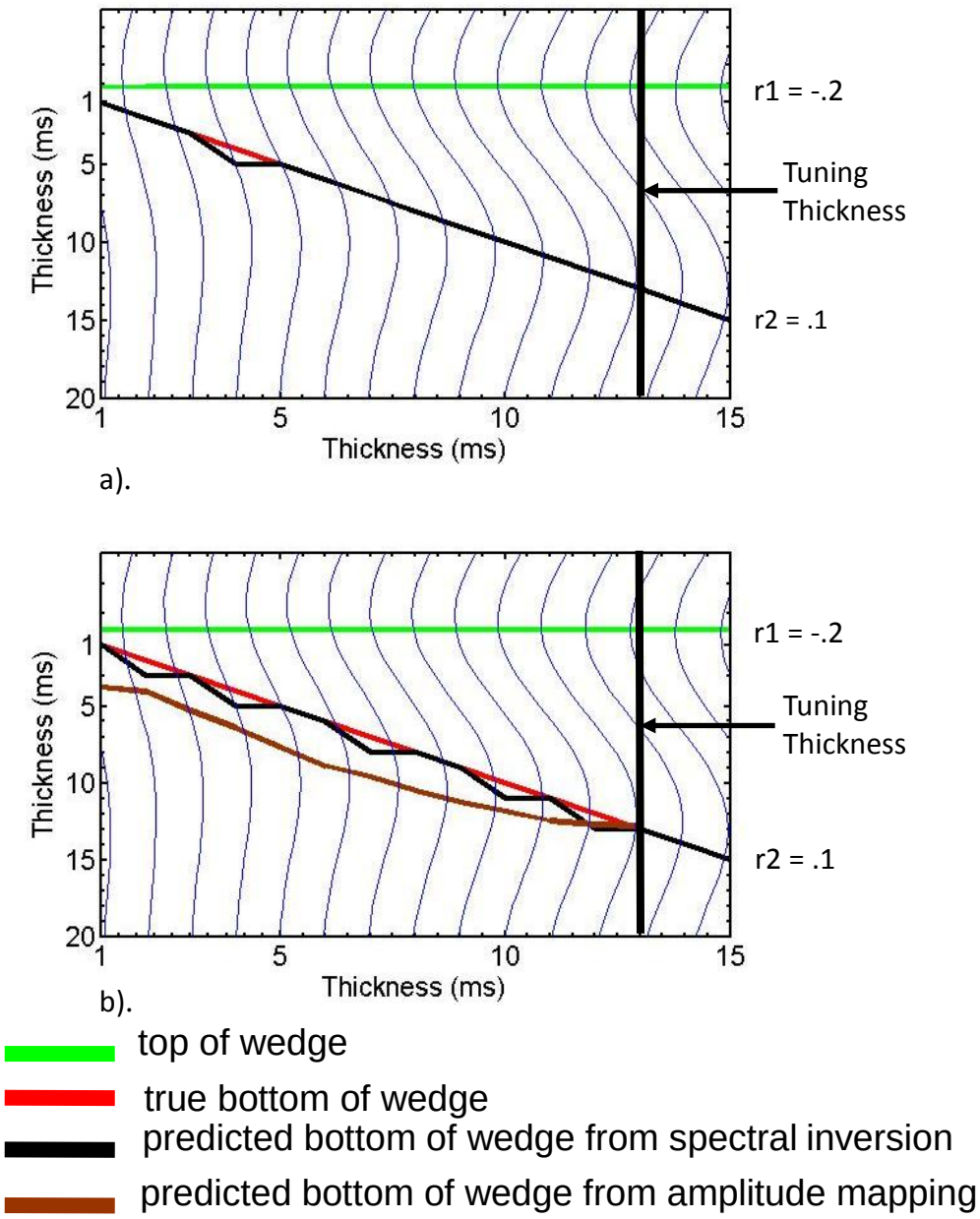

Figure A8. Original reflectivity models for a (a) predominately odd reflection coefficient pair and a (b) predominately even reflection coefficient pair. The tuning thickness for the 30 Hz Ricker wavelet convolved with the RC pair (blue) is defined by the vertical black line.

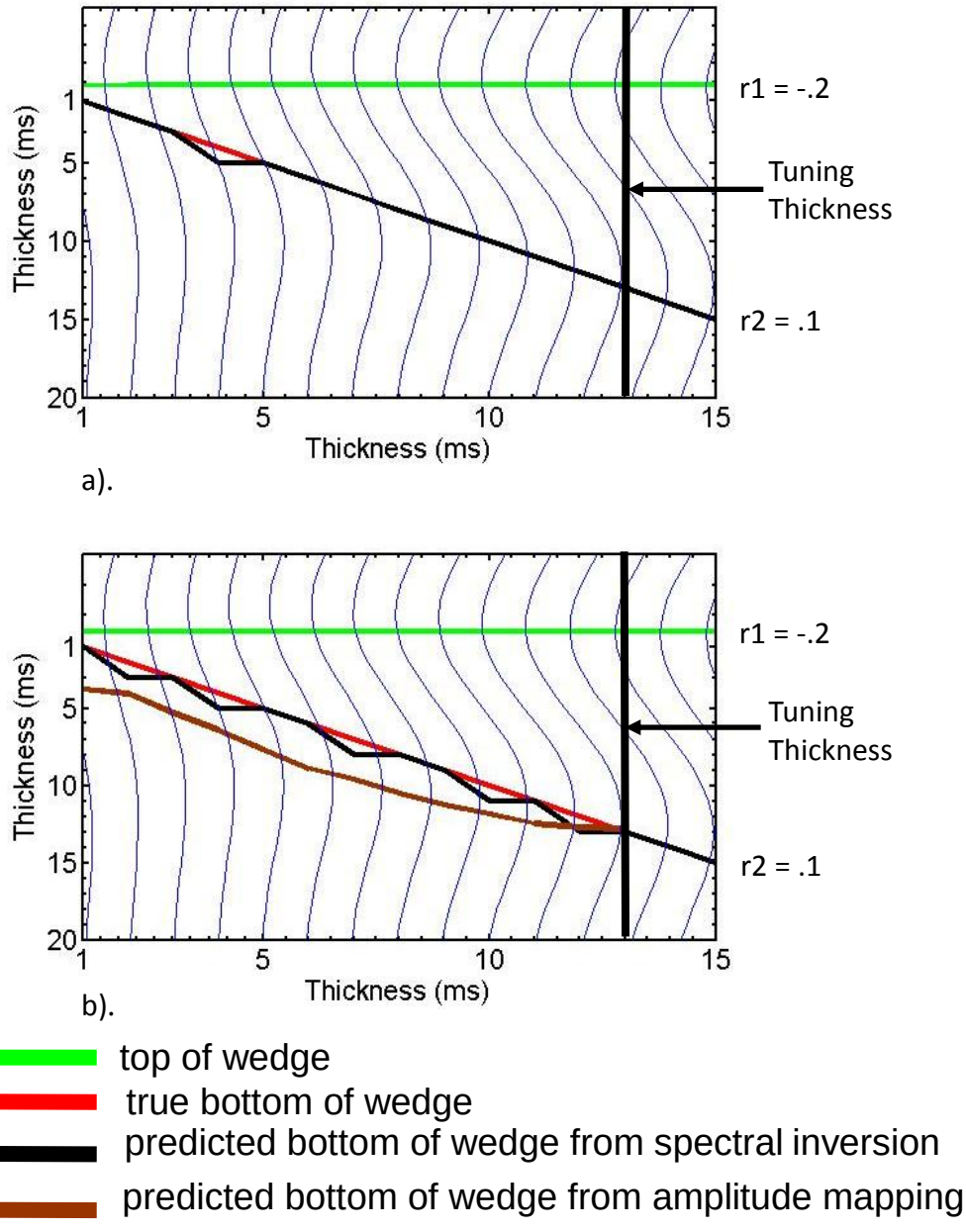

Figure A9. Result of the thickness inversion of a predominately odd reflection coefficient pair with (a) 1 percent noise and (b) 5 percent noise. The plot shows the original model (green and red) together with the inversion (black) and the amplitude mapping technique (brown), which uses the incorrect assumption of equal reflectivity. The tuning thickness for the 30 Hz Ricker wavelet convolved with the RC pair (blue) is defined by the vertical black line.

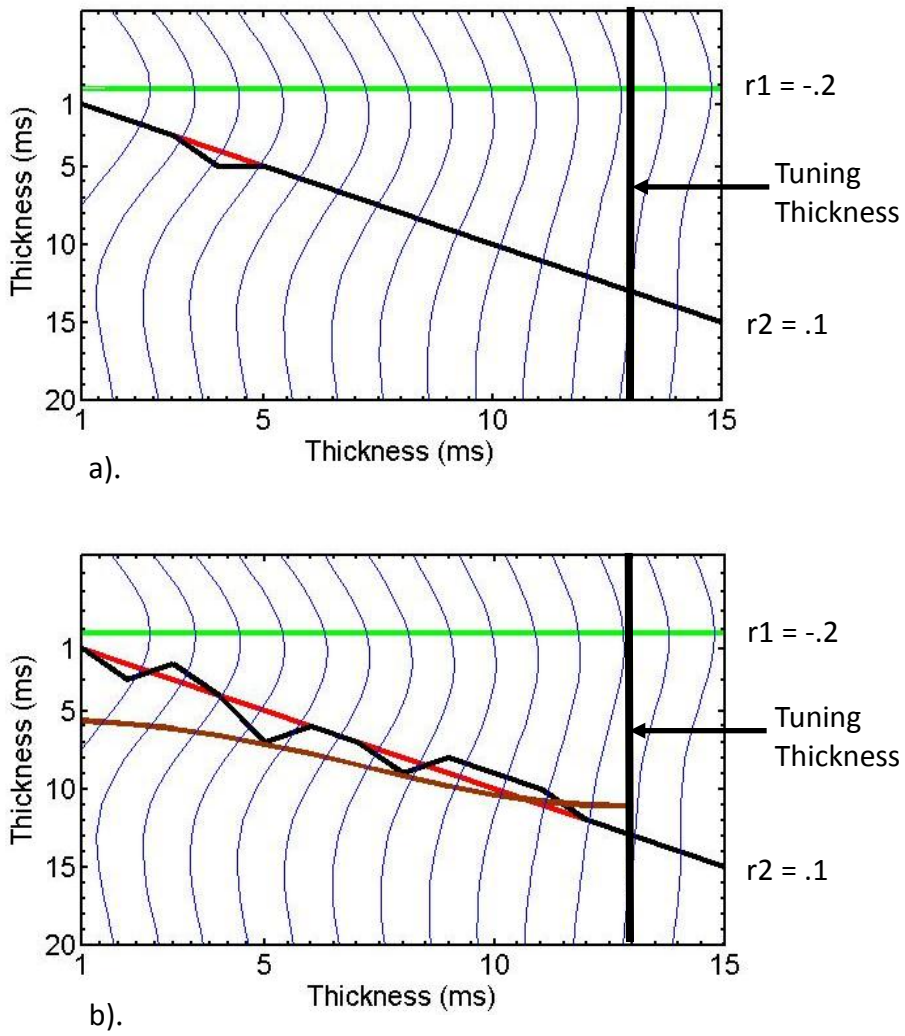

Figure A10. Result of the thickness inversion of a predominately even reflection coefficient pair with (a) 1 percent noise and (b) 5 percent noise. The plot shows the original model (green and red) together with the inversion (black) and the amplitude mapping technique (brown), which uses the incorrect assumption of equal reflectivity. The tuning thickness for the 30 Hz Ricker wavelet convolved with the RC pair (blue) is defined by the vertical black line.

does not increase significantly for very thin layers due to the reflectivity constraint, although the percent error increases as layer thickness decreases. Reflection coefficient estimates were comparably accurate. As expected, accuracy deteriorates as the noise increases beyond 5 percent. Thus, for a given wavelet peak frequency and analysis band, the noise level rather than the tuning thickness determines the limit of resolution.

The tuning analysis predictions are shifted toward thicker layers for the even and odd components due to the assumption of equal magnitude reflection coefficients at top and base. The assumption causes a bias in the relationship between amplitude and thickness that depends on the particular mapping scheme. We plotted the results of the amplitude mapping techniques that generated the least error in thickness prediction. For the predominately odd pair, the optimal amplitude mapping method was a simple linear regression from peak tuning to zero thickness. However, this technique generated large errors and negative thickness predictions for the predominately even pair. Instead, for the predominately even pair, we assumed that both the reflection coefficients were equal to the peak background amplitude for the thick layer and mapped thickness from the tuning amplitude to zero thickness.

We tested the inversion on a reflector model that violates the basic assumptions of the method. The model includes two layers defined by 3 reflectors, all with reflection coefficients equal to .1. The top layer has twice the thickness of the lower layer. We decomposed the spectrum using an 80 ms DFT with a Gaussian taper centered on the thicker layer. Figure A11 shows the model (green and red) and the resulting inversion

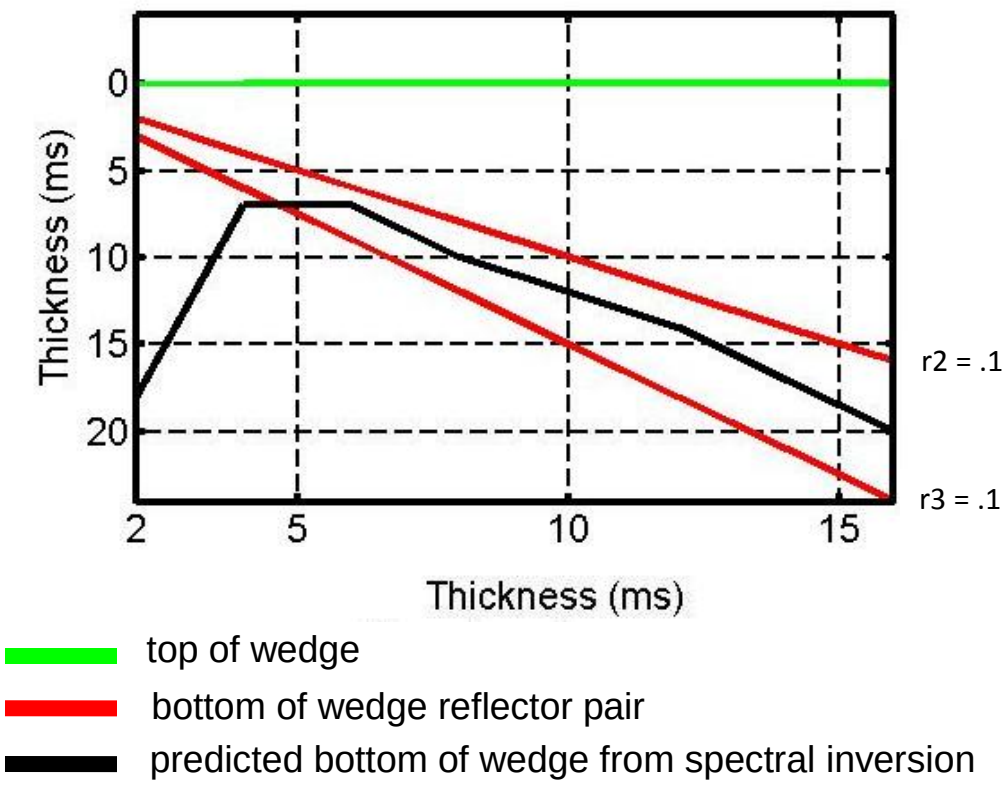

Figure A11. Result of the inversion for a two-layer model, violating the assumptions of the method. For thicker layers, the predicted layer thickness from the inversion (black), measured from the top reflector, falls between the thickness of the thicker layer and that of the total package. As the reflectors converge, the inversion becomes unstable.

(black). The predicted layer thickness is measured from the top reflector to the black line, yielding a thickness value greater than that of the thicker layer but less than that of the two layers combined. The observed predicted thickness results from the interference of the two layers in the frequency domain, creating a period corresponding to a single layer that is slightly thicker than the thickest layer. The reflection coefficient predictions for the lower reflector were closer to the sum of the two base reflection coefficients $r_2 + r_3 = .2$ for thin layers, and to the single base reflection coefficient value

$r_2 = r_3 = .1$ for thicker layers. In practice, additional spikes widely spaced from the reflectors of the layer should be considered noise for the single layer model. While we value the single layer model for its ease of invertibility, it is necessary to extend the inversion scheme so that it can simultaneously invert seismograms containing multiple interfering layers for most real cases.

Extension of the method to multiple layers

Recognizing that the seismogram can be represented as a superposition of impulse pairs, the inversion for the properties of a single layer is easily extended to encompass a general reflectivity series inversion by considering the spectrum versus time acquired using a moving window as a superposition of interference patterns originating at different times. The inversion process for reflection coefficients and layer thickness is performed simultaneously for all impulse pairs affecting the local seismic response.

Let us represent the reflectivity series, r(t), as a summation of even and odd impulse pairs.

$$r(t) = \int_{-\infty}^{\infty} [r_e(t) II(\frac{t-\tau}{T(t)})]dt + \int_{-\infty}^{\infty} [r_o(t) I_I(\frac{t-\tau}{T(t)})]dt, \qquad \text{(A13)}$$

where $r_e(t)$ and $r_o(t)$ are the magnitudes of the impulse pairs as a function of time, and T(t) is the time series of layer time-thicknesses. Assuming a convolutional seismogram and known wavelet w(t, f), a spectral decomposition of a seismic trace s(t, f) is then

$$s(t, f) = w(t, f) \int_{-t_w}^{t_w} \{r_e(t)\cos[\pi f T(t)] + i r_o(t)\sin[\pi f T(t)]\}dt\,, \qquad \text{(A14)}$$

where t_w = window half length. As the multi-layer case involves more than two reflectors, it is necessary to use an objective function for inversion that properly accounts for interference between multiple layers. If the wavelet spectrum is known, we can now solve for r(t) and T(t) by optimizing the objective function, $O(t, r_e, r_o, T)$, by

$$O(t, r_e, r_o, T) = \int_{f_L}^{f_H} \left[\begin{array}{l} \alpha_e \{ \mathrm{Re}[s(t, f) / w(t, f)] - \int_{-t_w}^{t_w} r_e(t) \cos[\pi f T(t)] dt \} \\ + \alpha_o \{ \mathrm{Im}[s(t, f) / w(t, f)] - \int_{-t_w}^{t_w} r_o(t) \sin[\pi f T(t)] dt \} \cdot \end{array} \right] df \quad , \text{(A15)}$$

where f_l = low frequency cutoff, f_h = high frequency cutoff, and α_e and α_o are weighting functions, the ratio of which can be adjusted to find an acceptable trade-off between noise and resolution. For high α_o / α_e, the reflectivity approaches the Widess model and the resolution limit becomes λ/8. We summarize the multi-layer inversion method using a flowchart in Figure A12.

Multilayer synthetic example

In order to validate the multilayer inversion technique in a controlled situation, we generated a model containing several arbitrary layers (Figure A12a), from which we generated a synthetic trace (Figure A12b). The reflectivity spikes were convolved with a 30 Hz Ricker wavelet. The identical trace with variable random noise is repeated in the figure for visual clarity. We tested the inversion using windows of different lengths and centered at different locations along the synthetic trace. Assuming no *a priori* insight, we set the weighting function relationship $\alpha_o = \alpha_e$, and minimized the objective function given by equation A15 using a standard least-squares conjugate gradient inversion. We

inverted the data from a 200 ms Gaussian-tapered Fourier transform, thereby recovering the original model (Figure A12c). Shortening the total window length to 100 ms and maintaining the Gaussian taper, we computed the Fourier transform for time samples between 50 ms and 150 ms, respectively. The window is shifted one time sample at a time, with the results of each previous window acting as a constraint for the next inversion. If no new reflectors appear in the window or exit the window as it is shifted downward, the result is the same as in the previous window. If there are no reflectors in the window, the algorithm simply inverts the noise, a result which is not particularly problematic because the noise is not amplified. The results for the windows centered at 50 ms and 150 ms are shown in Figures A12d and A12e. As expected, the shorter windows divide the overall longer series of reflectors into two isolated sets. By superposition, we can add up the two sets of reflectors to obtain the longer series. Although the window length can be varied according to the desired result, there are practical limits to the length of an optimal inversion window, which are often defined by trial-and error. If the window is too short, frequency resolution suffers; if the window is too long, time resolution is lost (see Castagna et al., 2003).

REAL DATA RESULTS

Comparison to well log data

We studied the results of the application of the multi-layer spectral inversion method shown in Figure 13 to two seismic data sets from the Gulf of Mexico shelf. Well information for lithologic interpretation including P-wave, resistivity, and deep induction

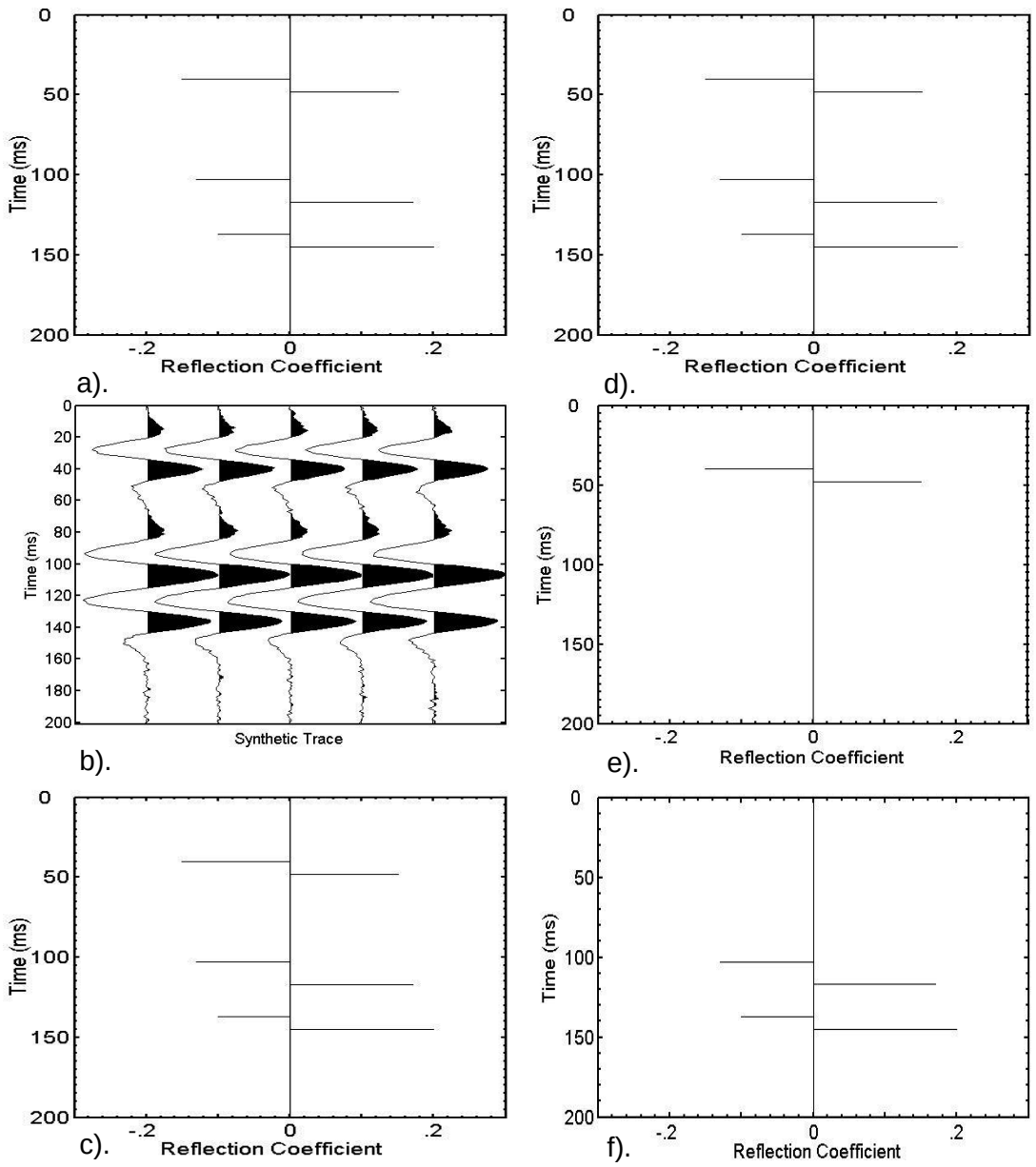

Figure A12. The (a) original model is convolved with a 30 Hz Ricker wavelet to create a (b) synthetic seismogram. The (c) spectral inversion result using a 200 ms window centered at 100 ms recovers the original reflectivity series. The (d) spectral inversion result using a 100 ms window centered at 50 ms and (e) spectral inversion result using a 100 ms window centered at 150 ms recover the portions of the reflectivity series contained within the window. By superposition, c = d +e.

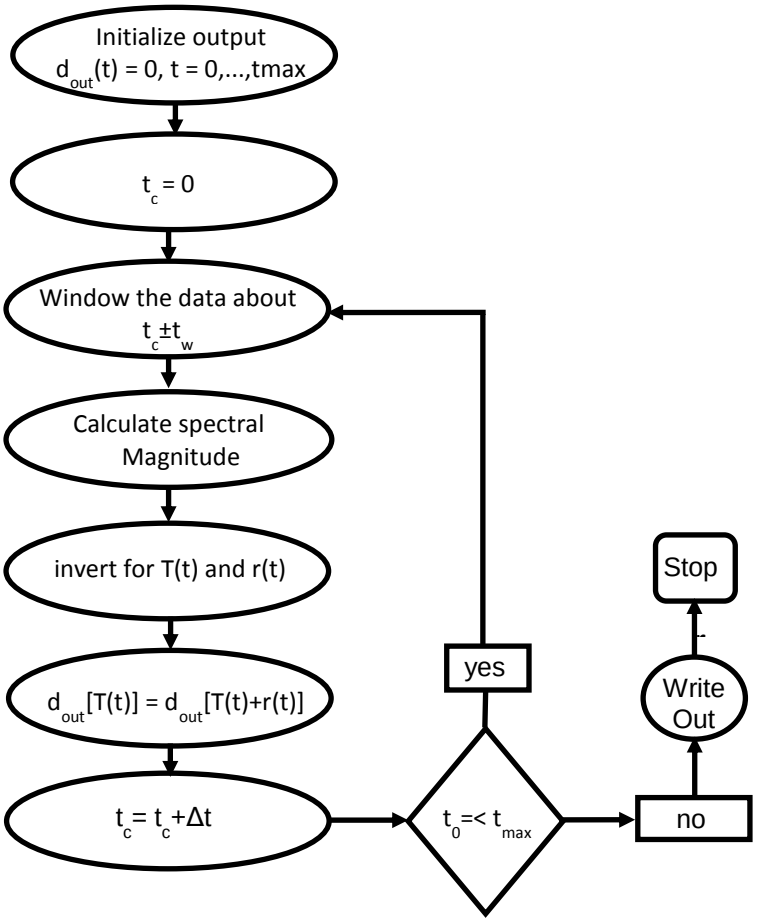

Figure A13. Flowchart for the method of the inversion, where d_{out} is the output trace, t_c is the time sample at the center of the window, and Δt is the sampling invterval.

and the well log data, stretching the well log data to time without reference to the inverted data for an unbiased, quantitative layer thickness comparison between the well log data and the inverted data. The wavelet extracted from the well for the synthetic is shown in Figure A15. We also visually compared the well log data, the inverted data, and the original data in order to assess the difference in vertical resolution between the inverted data and the original data (Figures A16 and A17).

The original seismic tie to the well is shown in Figure A14. We achieved a relatively good fit (r = .64) between the reflectivity convolved with the extracted wavelet and the seismic trace. However, because the seismic data are much lower frequency than the log data, the fit is useful only as an approximation for aligning gross lithologic packages. A great deal of useful information is lost to the seismic wavelet (Figure A15).

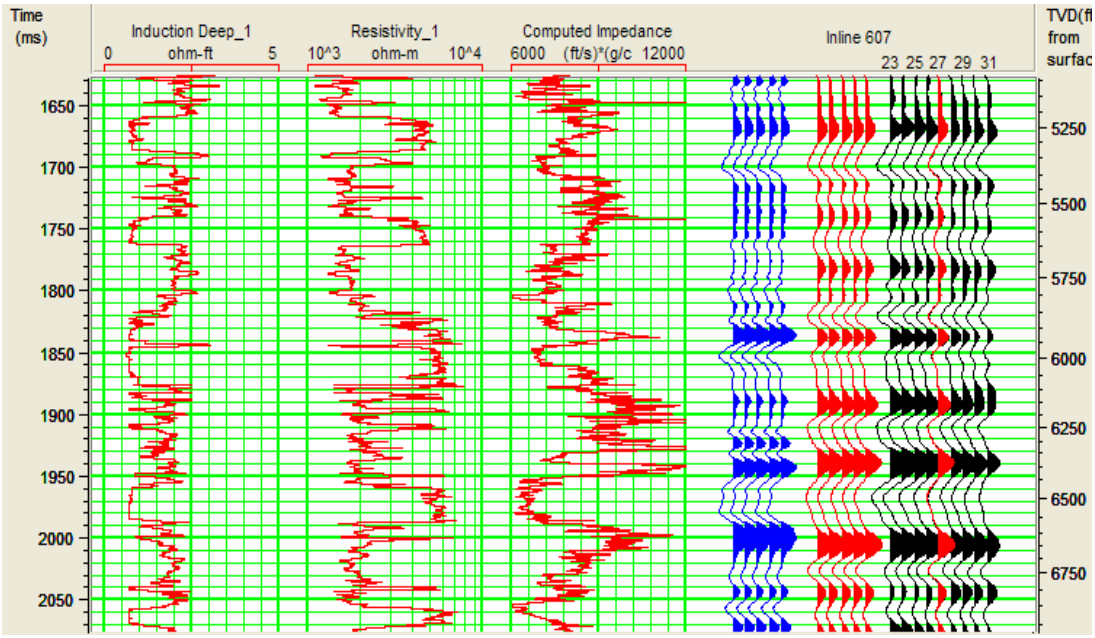

Figure A14. Well log data including deep induction, resistivity, and computed impedance, together with the synthetic tie (blue), the trace at the well (red), and the seismic traces surrounding the well (black). The correlation coefficient is r = .64.

The thickness inversion provides a significantly better representation of the layering observed in the log data than does the original seismic data. Figure A16 shows the spectral inversion for reflectivity displayed with a -90 degree phase shift to emphasize relative impedance changes and a slight time shift from the original synthetic to provide

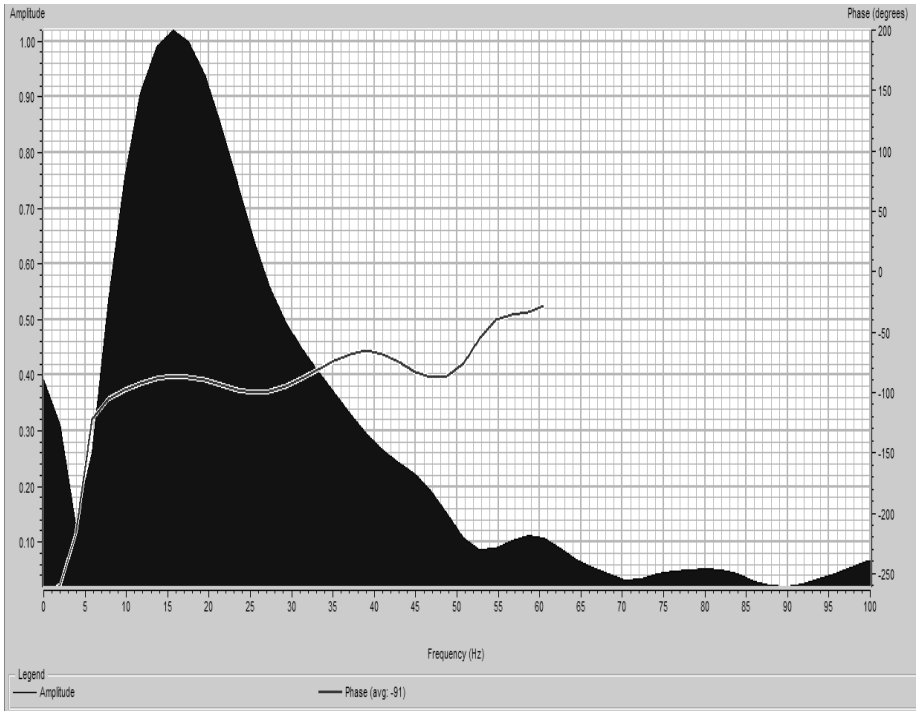

Figure A15. The phase and amplitude spectra of the wavelet extracted from the well. The peak frequency is 16 Hz.

a tie to the well with higher fidelity. The need for this time shift only becomes apparent after reflectivity inversion. The lithologic column shows sand and shale packages interpreted primarily from the three logs (see Figure A17). We initially distinguished sands and shales using a gamma ray log; but we used resistivity, deep induction, and impedance for the bulk of the interpretation because the gamma ray was absent in the available well with a P-wave velocity log. Generally, sands correspond to higher resistivity and lower deep induction than shallow resistivity values as a result of mud filtrate invasion. In the interval shown in Figure A16, the sands have higher impedance than the shales. Comparing the lithologic column to the inverted data, the thickness inversion clearly shows layering below the tuning thickness (the peak frequency of the

data is 16 Hz, yielding a one-quarter wavelength resolution of about 31 ms). A well resolved sand-shale sequence having a total thickness very close to the tuning thickness is also indicated in Figure A16. While the thickness inversion effectively delineates the layering sequence below tuning, it fails to capture gradational impedance changes within thin layers, as in the case of the shale grading to sand shown in the lithologic column. The following example demonstrates the vast improvement in vertical resolution for discrete layers achieved by the thickness inversion over the original data.

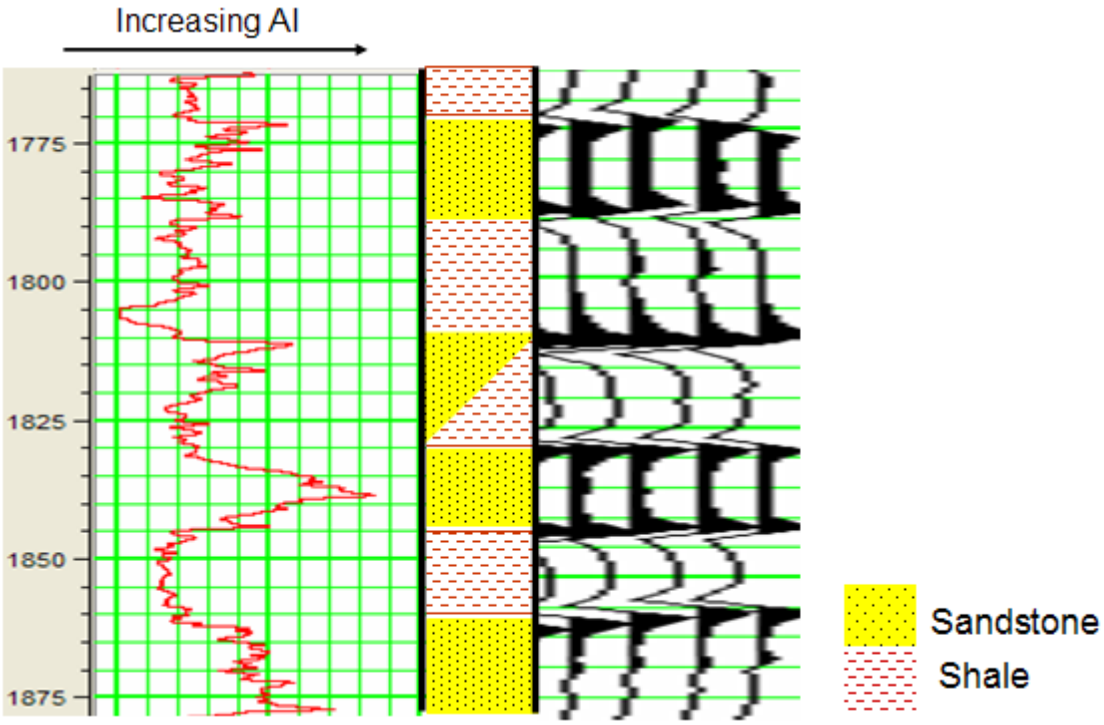

Figure A16. Impedance log (left) compared with the spectrally inverted data (right). Sands are higher impedance in this interval. The lithologic section interpreted from the impedance log shows a close correspondence to the inverted data. Note the two-layer sequence resolved at the tuning thickness.

Comparison to conventional seismic data

Viewing the comparison of the thickness inversion to the original seismic data in Figure A17, both with a -90 degree phase rotation, it is clear that boundaries between layers are indistinct on the original seismic. Layers below the 31 ms tuning thickness are not resolved on the original seismic data. Geologic detail is obscured by the wavelet interference patterns, which become more apparent when compared to the inversion. While a skilled interpreter can decipher meaningful information embedded in the wavelet interference patterns, it is desirable to remove these artifacts altogether in order to allow direct access to the underlying geology.

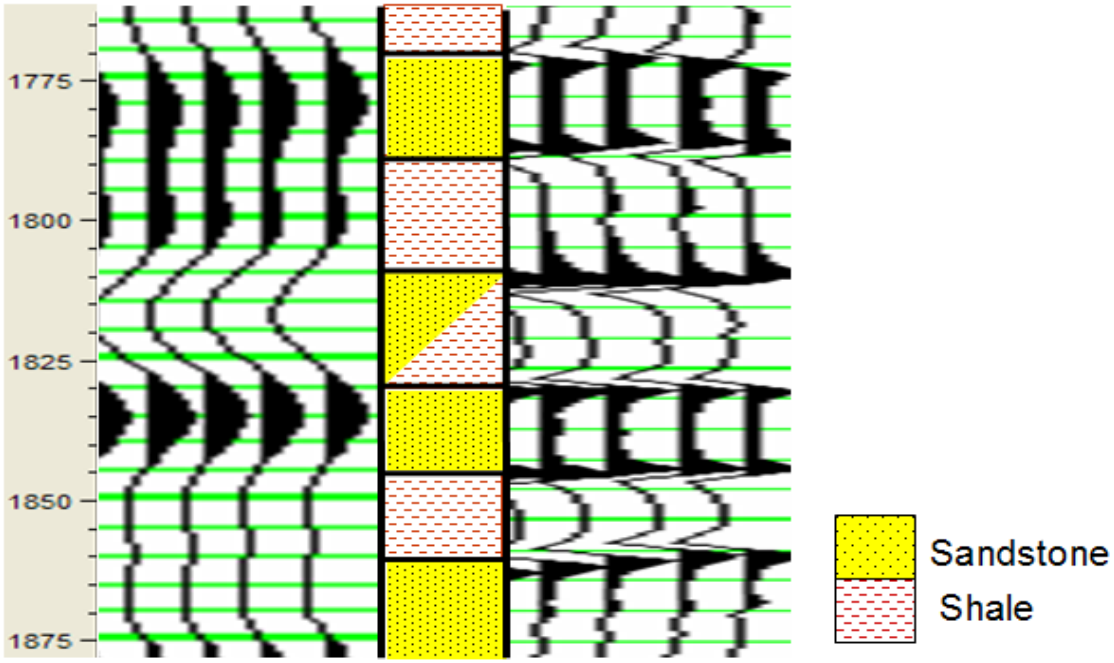

Figure A17. Comparison of the original seismic data (left) with the lithologic column (center) and the thickness inverted data (right). Both data sets are phase rotated by -90 degrees. Note the failure of the original seismic data to delineate thin layering as compared to the inverted data. Also note that the inverted data does not resolve gradational changes within an individual layer.

Thickness comparison

We quantitatively compared thicknesses from the well log data to those from the spectral reflectivity inversion, interpreting the layering from the well log data that was stretched from depth to time on the original synthetic and comparing the results to the inverted thicknesses as defined by zero crossings on the -90 degree phase rotated spectral reflectivity inversion. We performed the interpretation between 1700 ms and 2900 ms. The comparison is plotted in Figure 18, with an excellent correlation between the well log data thicknesses and the predicted thicknesses (pink) below the tuning line (red). The mean error for the two data sets is μ = -.5 ms, indicating that on the average the method is accurate and unbiased. The square of the correlation coefficient is R^2 = .94 with a standard deviation of σ = 3.10 ms, corresponding to precision in thickness estimation on the order of 15 feet for this example.

Stratigraphic interpretation

Figures A19-A21 show stratigraphic examples in which both the original seismic data and the spectrally inverted data have a -90 degree phase to highlight layer boundaries. An example of the wavelet overprint effect is observed on the large-scale seismic line comparison of Figure A19. On the original seismic line, an apparent discontinuity is inferred at about 1315 ms (Figure A19a). The discontinuity might be interpreted as a localized fault with minimal offset or as a stratigraphic discontinuity in layering. However, comparison with the inverted data (Figure A19b) reveals another picture. While the inverted data shows more detail in general, it is interesting to note

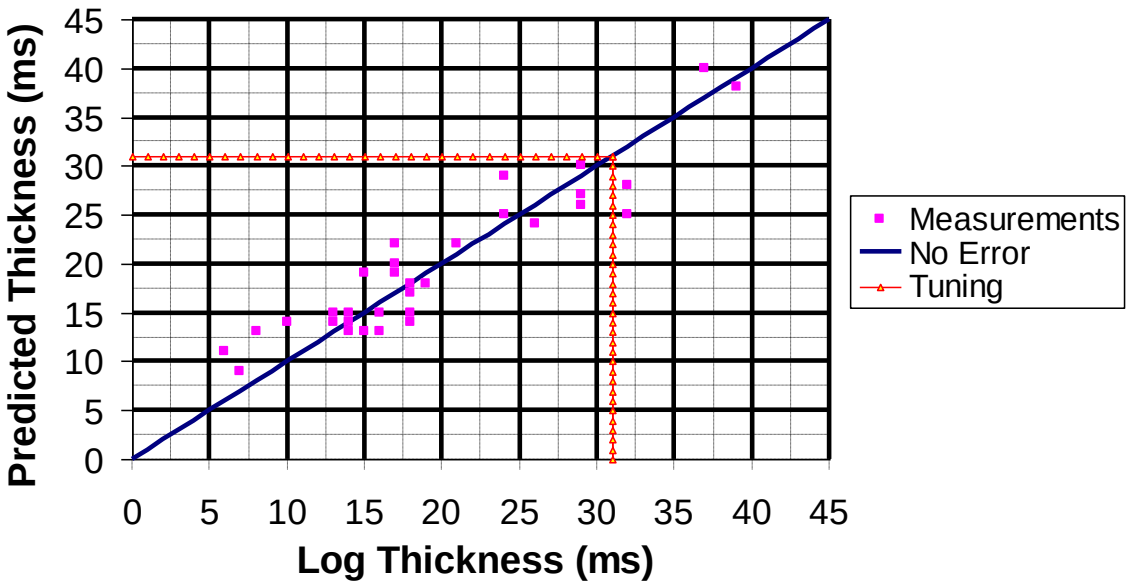

Figure A18. Plot of predicted thicknesses from the inversion (pink dots) vs. well log interpreted thickness (1:1 diagonal is shown by the blue line), showing a strong correlation between the two. The thicknesses were interpreted between 1700 ms and 2900 ms. The tuning thickness is marked by the red line, and accuracy is maintained below one-eighth of a wavelength.

that the apparent discontinuity in layering does not exist on the inverted section in spite of the fact that the inverted data is generated using a trace-by-trace operation that makes no assumption about lateral continuity. On the inverted section, it can be seen that the apparent disruption in layering actually represents a lateral change of rock properties within a given layer. The discrepancy points to the fact that the apparent discontinuity in reflection arrival times seen on the original data is actually not a geological feature but a geophysical effect, specifically a shift in the wavelet interference pattern caused by an impedance change that resembles a small geological layering discontinuity in the seismic image.

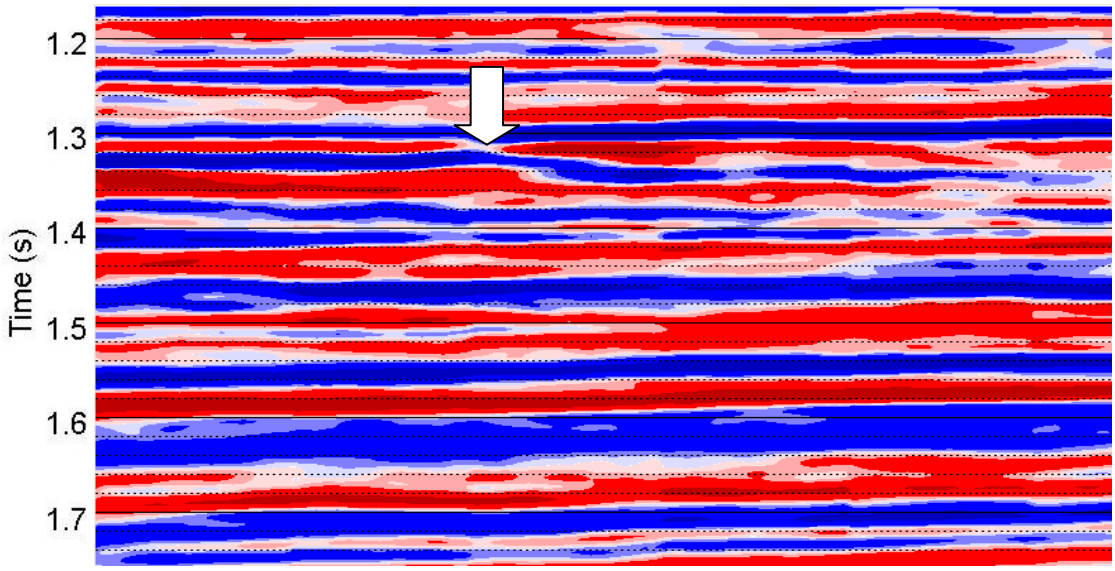

a).

1 Km

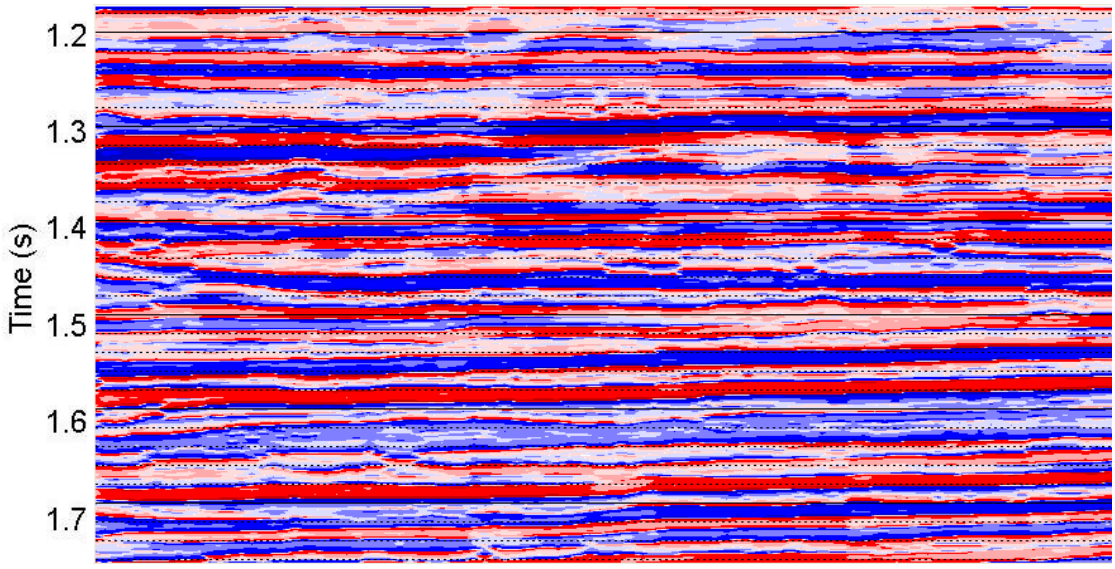

1 Km

b).

Figure A19. The (a) original seismic data shows a small discontinuity. The (b) thickness inverted data reveals a strikingly continuous layer, a strong indication that the geological discontinuity seen in (a) is actually a wavelet effect rather than a real subsurface feature. The phase for both images is -90, and red is higher impedance.

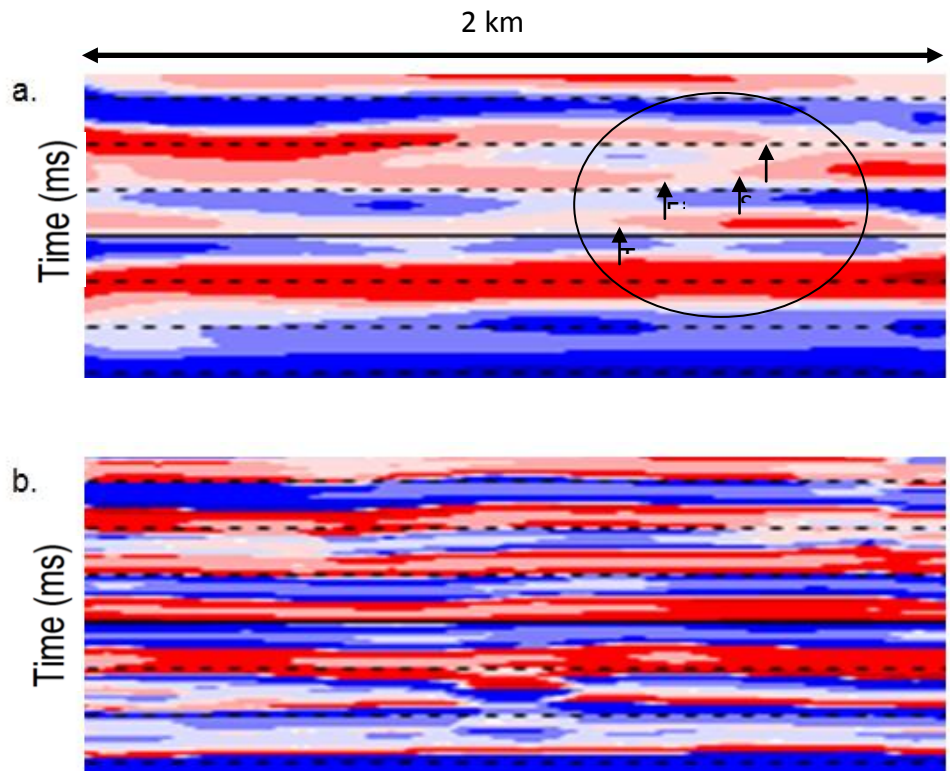

Figure A20. The (a) original seismic line has significant stratigraphic discontinuities (black arrows) that might be interpreted as the termini of discreet depositional lobes. The (b) spectrally inverted data reveals laterally continuous layering characteristic of undisturbed layer cake geology. The phase for both datasets is -90 degrees. Timing lines are 20 ms, and red is higher impedance.

The smaller-scale image in Figure A20 shows significant lateral breaks in layering that might be interpreted as discreet sand bodies with possible erosion of previously continuous layers. These features can be caused by different types of downslope transport mechanisms such as channel incision. The horizons on the original data (Figure A20a) are difficult to continue in places (black arrows). However, the spectrally inverted data (Figure A20b), which assumes no relationship between neighboring traces, shows striking continuity along the same horizons. Once again, the complex wavelet

interference pattern has created an illusory geological scenario that accompanies limited resolution.

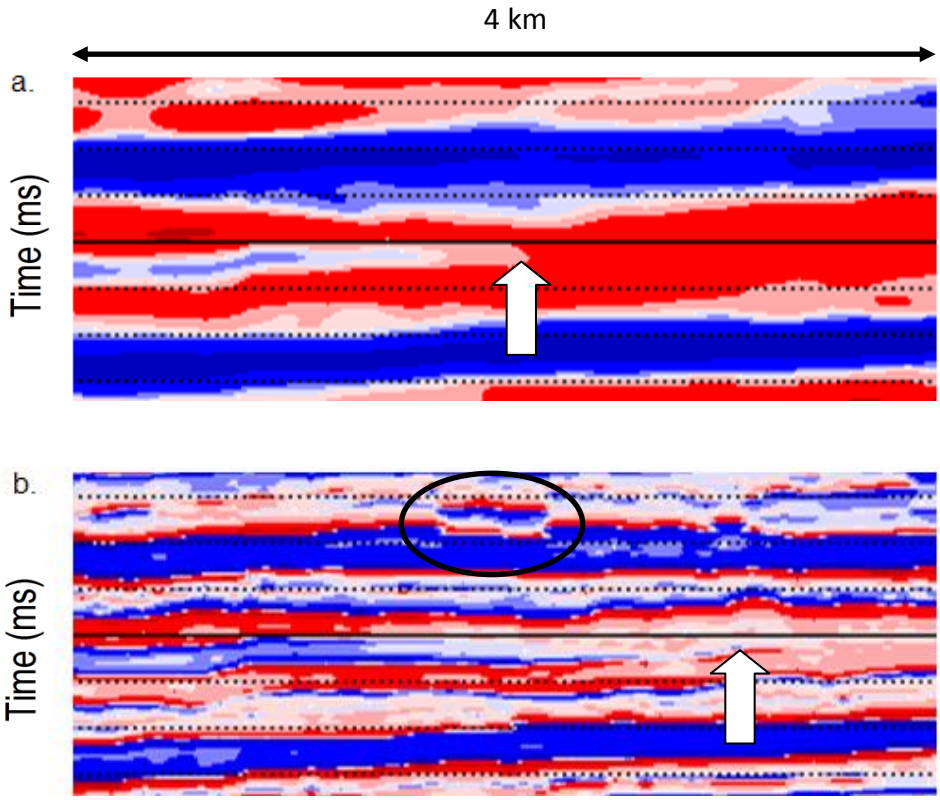

Figure A21. The (a) original seismic data shows a pinchout (white arrow) where the thin layer becomes unresolved. The (b) inverted data images the pinchout much further updip. An apparent erosional feature (black circle) is resolved on the inversion. The phase for both datasets is -90 degrees. Timing lines are 20 ms, and red is higher impedance.

Figure A21 shows an example of the same wavelet effect erasing geological information. In the original seismic data (Figure A21a), the apparent pinchout of a low impedance layer is observed, with the upper and lower events merging below the resolution of the layer (white arrow). However, the spectrally inverted data (Figure A21b) shows the same low impedance layer imaged much further updip, together with the resolved

bounding layers. Also, an apparent localized broadening or bulge in the wavelet in the original data just below the first two timing lines is resolved as a possible erosional incision on the inverted data. Such improved detection of stratigraphic variation has significant implications for better reservoir characterization and delineation.

We tested the method on a line of data from a shallow Gulf of Mexico dataset with known large incision features previously mapped using the coherence attribute. Figures A22 and A23 show zero-phase original seismic images and -90 degree phase rotated spectral inversion images. Typically, seismic images of channels show significant relief from the overbank deposit to the thalwag, which appeals to the intuitive concept of a curved channel geometry. Figure A22a shows an example of a pair of adjacent channels showing a strongly curved geometry on the original seismic data. The -90 degree phase rotated spectrally inverted section of the data (Figure A22b) shows an alternate image of the channels in which the curvature seen in the channel profile is not as prominent, hinting at the possibility that some component of the curvature can be attributed to the rapid rock property changes known to occur across the strike of a channel. We believe further investigation of this phenomenon using well control is warranted.

Figures A23a and A23b show another large channel imaged on the original seismic data and on the -90 degree phase rotated spectral inversion respectively. The tuning effect in the original data confounds channel thickness interpretation as the channel

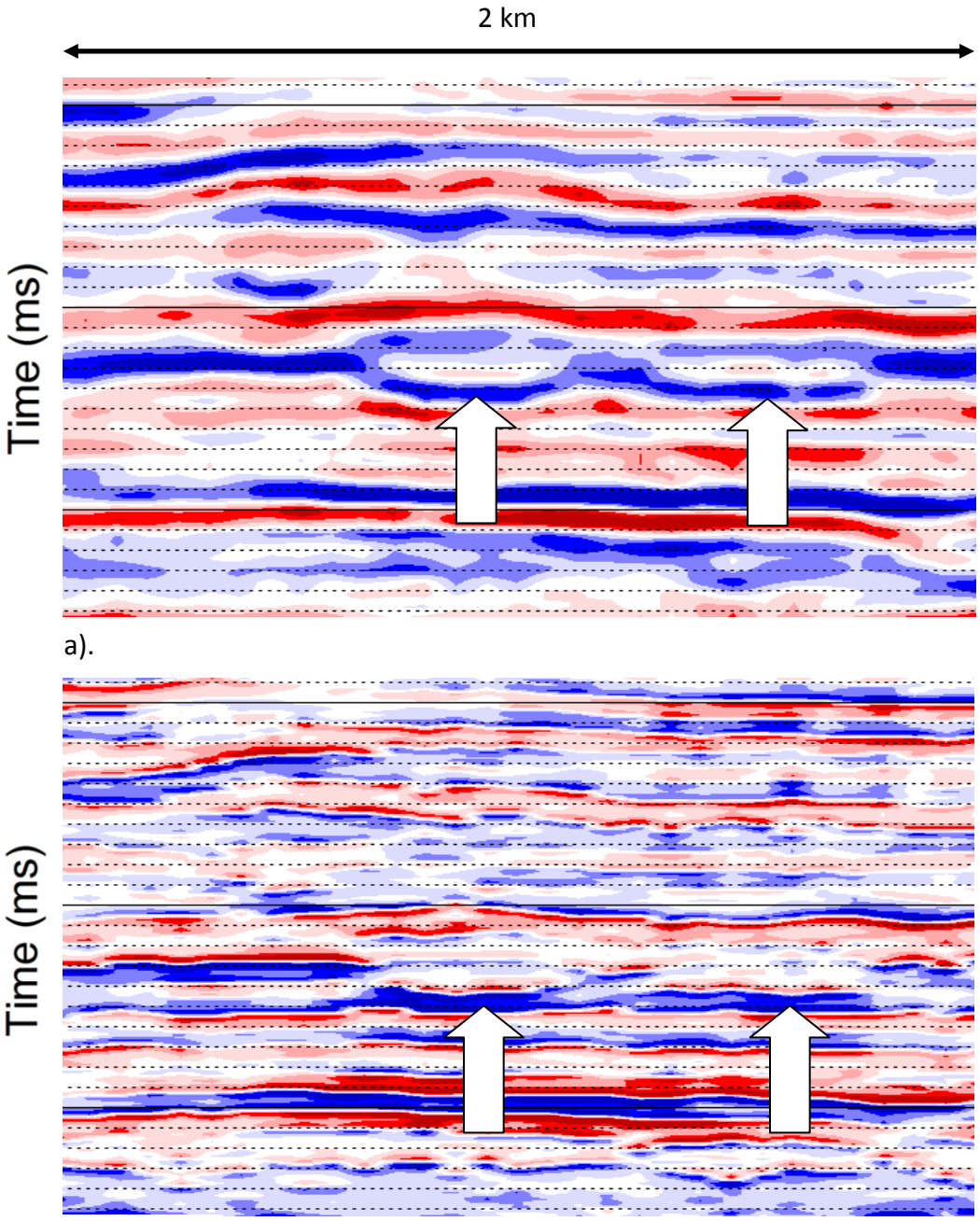

Figure A22. Comparison of the (a) original zero phase seismic data to the (b) spectrally inverted data, which is phase rotated -90 degrees from (a). Channels (white arrows show the base of channels) have more relief and more curvature on the original seismic data. Timing lines are 10 ms, and red is higher impedance.

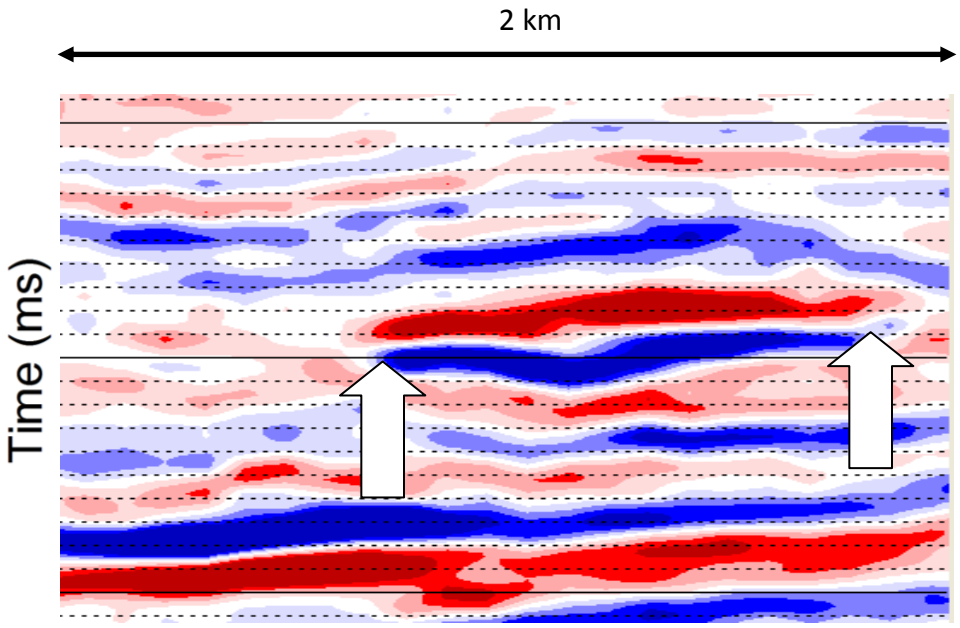

a).

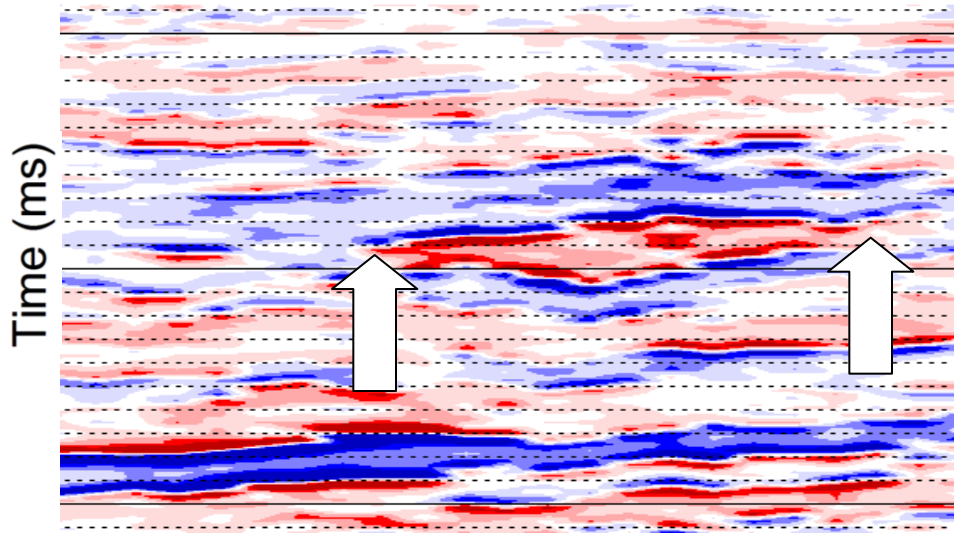

b).

Figure A23. A large channel (white arrows show the edges of the channel) imaged on the (a) original zero phase seismic data and the (b) spectrally inverted data, which is phase rotated -90 degrees from (a). The thin bed layering of the channel edges and overall vertical channel extent are more precisely imaged on the inverted data. Timing lines are 10 ms, and red is higher impedance.

thins toward the levees. There is also an ambiguity in the placement of the top and base bounding surfaces of the channel related to the wavelet phase. The inverted data shows a clearer picture of the channel geometry, with constant thinning of the channel fill wedges toward the edges of the channel. Also, the top and base bounding surfaces of the channel can be picked more precisely on the inverted data at the sharply defined zero crossings with less guesswork in the placement of horizons. Thus, in the workflow of seismic interpretation, spectral inversion adds visual information that can contribute to the delineation of geologic features of interest such as channels.

CONCLUSIONS

Beginning with a generalized theory of reflectivity, spectral decomposition is used as a tool to unravel the complex interference patterns created by thin-bed reflectivity. These patterns can be inverted to obtain the original reflectivity. We developed and studied new analytical methods for spectral inversion based on complex spectral analysis. We find that spectral inversion yields accurate thickness determinations below tuning utilizing the inverse relationship between thickness and the constant periodicity of spectral interference patterns. Representing the seismogram as a superposition of simple layer responses constitutes a means of imposing on the inversion the *a priori* assumption that sedimentary rocks occur as layers with discrete interfaces at the top and base and can be represented as such in a reflectivity series. When this assumption is valid, the consequence is that, on the inverted reflectivity trace, there is geologically meaningful information at frequencies outside the band of

the original seismic data. When this assumption is false, the "recovered" frequency information outside the band of the original seismic will also be false. For example, smooth impedance transitions will be inverted as blocky steps in impedance.

Spectral shape information obtained from spectral decomposition can be used to drive an inversion with significantly greater vertical resolution than that of the original seismic data, thereby allowing improved thickness estimation, better correlation to well logs, and improved stratigraphic interpretation. These results are achieved without utilization of well log information in the inversion as a starting model or as a constraint. The resulting inversion is, therefore, unbiased by pre-conceived ideas. As evidenced by the results of the application of the method to real data, spectral inversion has great potential for practical value as a tool for seismic exploration.

While the spectral inversion methods described in this work demonstrate improvement in vertical resolution, we did not utilize well log information after the wavelet removal step. It is desirable to investigate the effectiveness of using well log data to further improve vertical resolution of inter-bedded layers or gradational changes within layers that are not revealed by seismic spectral inversion alone. Also, thickness constraints from spectral inversion could be used as input for more accurate model-based impedance inversion.

ACKNOWLEDGEMENTS

The authors would like to thank Gene Sparkman, Carlos Moreno, Xianhui Zhu, and Oleg Portniaguine of Fusion Petroleum Technologies for their help and support. Thanks also to Kurt Marfurt and Scott Morton for assistance, suggestions, and contributions. Financial support was provided by ExxonMobil and Shell.

APPENDIX A1

DISCUSSION OF THE SHIFT EFFECT

When examining the real and imaginary components separately, a phase shift occurs if the analysis window is not centered on the layer. In order to study this effect in more detail, we revisited the original equations. The shift theorem says that a time sample shift Δt away from the layer center t_c in the time domain is equivalent to a phase ramp in the frequency domain:

$$g(t_c + \Delta t) \leftrightarrow e^{2i\pi f\Delta t} g(f). \qquad \text{(A1-1)}$$

Apply this equivalency

$$e^{2i\pi f\Delta t} g(f) = [\cos(2\pi f\Delta t) + i\sin(2\pi f\Delta t)][2r_e \cos(\pi fT) + i2r_o \sin(\pi fT)]. \qquad \text{(A1-2)}$$

Take the real component of equation A1-2

$$\mathrm{Re}[e^{2i\pi f\Delta t} g(f)] = 2r_e \cos(\pi fT)\cos(2\pi f\Delta t) - 2r_o \sin(\pi fT)\sin(2\pi f\Delta t). \qquad \text{(A1-3)}$$

Rearranging yields

$$\begin{aligned}\mathrm{Re}[e^{2i\pi f\Delta t} g(f)] &= 2r_o[\cos(\pi fT)\cos(2\pi f\Delta t) - \sin(\pi fT)\sin(2\pi f\Delta t)] \\ &\quad \text{or} \\ &\quad + 2(r_e - r_o)\cos(2\pi f\Delta t)\cos(\pi fT), \\ &= 2r_o \cos(2\pi f\,(\Delta t + T/2)) + 2(r_e - r_o)\cos(2\pi f\Delta t)\cos(\pi fT), \end{aligned} \qquad \text{(A1-4)}$$

which has the form of a modulation and represents the spectral plots of time-shifted models. A similar expression can be derived for the odd component. The phase shift corresponds to a sinusoidal modulation of the signal, which can be viewed as an interference pattern superimposed upon another interference pattern. Furthermore, the period of the interference pattern is determined by the magnitude of the shift.

APPENDIX A2

INVERSION MODEL DERIVATION

Applying the shift theorem (equation A1-1) and taking general expressions for the real and imaginary spectra

$$\mathrm{Im}[e^{2i\pi f\Delta t}g(f)] = 2r_o \sin(\pi fT)\cos(2\pi f\Delta t) + 2r_e \cos(\pi fT)\sin(2\pi f\Delta t) \quad \text{and} \qquad \text{(A2-1)}$$

$$\mathrm{Re}[e^{2i\pi f\Delta t}g(f)] = 2r_e \cos(\pi fT)\cos(2\pi f\Delta t) - 2r_o \sin(\pi fT)\sin(2\pi f\Delta t). \qquad \text{(A2-2)}$$

Express the amplitude spectrum and setting Δt = 0 as a constant reference

$$G(f) = \sqrt{\{\mathrm{Re}[e^{2i\pi f\Delta t}g(f)]\}^2 + \{\mathrm{Im}[e^{2i\pi f\Delta t}g(f)]\}^2} \quad \text{or}$$

$$= \sqrt{4r_e^2\cos^2(\pi fT) + 4r_0^2\sin^2(\pi fT)}. \qquad \text{(A2-3)}$$

Rearrange terms

$$G(f) = 2\sqrt{(r_e^2 - r_0^2)\cos^2(\pi fT) + r_0^2\cos^2(\pi fT) + r_0^2\sin^2(\pi fT)} \quad \text{or}$$

$$= 2\sqrt{(r_e^2 - r_0^2)\cos^2(\pi fT) + r_0^2}. \qquad \text{(A2-4)}$$

Take the derivative

$$\frac{dG(f)}{df} = -\frac{2\pi T(r_e^2 - r_o^2)\cos(\pi fT)\sin(\pi fT)}{\sqrt{(r_e^2 - r_o^2)\cos^2(\pi fT) + r_0^2}}. \qquad \text{(A2-5)}$$

Multiplying and simplifying using trigonometric identities yields

$$G(f)\frac{dG(f)}{df} = -4\pi T(r_e^2 - r_0^2)\cos(\pi fT)\sin(\pi fT) \quad \text{or}$$

$$= -2\pi Tk\sin(2\pi fT), \qquad \text{(A2-6)}$$

where $k = r_e^2 - r_o^2$.

Table 1. Nomenclature.

t	= seismic record time
$g(t)$	= time domain impulse pair
r_1	= top reflector in a two-reflector model
r_2	= base reflector in a two-reflector model
t_1	= time at top reflector in a two-reflector model
t_2	= time at base reflector in a two-reflector model
T	= layer two-way travel time thickness
t_c	= time at layer center in a two-reflector model
Δt	= time shift
f	= frequency
$g(f)$	= frequency domain impulse response
Re	= real component of a function
Im	= imaginary component of a function
r_e	= even component of the reflection coefficient
r_o	= odd component of the reflection coefficient
$G(f)$	= magnitude of amplitude as a function of frequency
$\frac{dG(f)}{df}$	= derivative of magnitude of amplitude with respect to frequency
k	= even component of reflectivity squared minus odd component squared
t_R	= tuning thickness
f_o	= wavelet peak frequency
$r(t)$	= reflection coefficient series as a function of time

τ = convolutional place holder

II = even impulse pair

I_I = odd impulse pair

s(t, f) = time and frequency varying seismic trace

w(t, f) = time and frequency varying seismic wavelet

t_w = window half length

$O(k,T)$ = frequency varying objective function

$O(t,r_e,r_o,T)$ = time and frequency varying objective function

α_e = even component weighting function

α_o = odd component weighting function

f_L = low frequency cutoff

f_H = high frequency cutoff

References

Castagna, J. P., S. Sun and R. W. Siegfried, 2003, Instantaneous spectral analysis: Detection of low-frequency shadows associated with hydrocarbons: The Leading Edge, **22**, 120-127.

Castagna, J. P., 2004, Spectral decomposition and high resolution reflectivity inversion: Presented at the Oklahoma Section Meeting, Society of Exploration Geophysicists.

Chopra, S., J. P. Castagna and O. Portniaguine, 2006a, Seismic resolution and thin-bed reflectivity inversion: Canadian Society of Exploration Geophysicists Recorder, **31**, 19-25.

Chopra, S., J. P. Castagna and O. Portniaguine, 2006b, Thin-bed reflectivity inversion: 75th Annual International Meeting of the Society of Exploration Geophysicists Expanded Abstracts, 2057-2061.

Chung, H. and D.C. Lawton, 1995, Frequency characteristics of seismic reflections from thin beds: Journal of the Canadian Society of Exploration Geophysicists, **31**, Nos. 1 and 2, 32-37.

Kallweit, R. S. and L. C. Wood, 1982, The limits of resolution of zero-phase wavelets: Geophysics, **47**, 1035-1046.

Marfurt, K. J. and R. L. Kirlin, 2001, Narrow-band spectral analysis and thin-bed tuning: Geophysics, **66**, 1274-1283.

Partyka, G. A., J. A. Gridley and J. A. Lopez, 1999, Interpretational aspects of spectral decomposition in reservoir characterization: The Leading Edge, **18**, 353-360.

Partyka, G. A., 2005, Spectral Decomposition: Society of Exploration Geophysicsts Distinguished Lecture.

Portniaguine O. and J. P. Castagna, 2004, Inverse spectral decomposition: 74th Annual International Meeting of the Society of Exploration Geophysicists Expanded Abstracts, 1786-1789.

Portniaguine O. and J. P. Castagna, 2005, Spectral Inversion: 75th Annual International Meeting of the Society of Exploration Geophysicists Expanded Abstracts, 1638-1641.

Puryear, C.I., 2006, Modeling and Application of Spectral Inversion for Determination of Layer Properties: M.S. Thesis, University of Houston.

Puryear, C.I. and J.P. Castagna, 2006, An algorithm for calculation of bed thickness and reflection coefficients from amplitude spectrum: 76th Annual International Meeting of the Society of Exploration Geophysicists Expanded Abstracts, 1767-1770.

Tirado, S., 2004, Sand thickness estimation using spectral decomposition: M.S. Thesis, University of Oklahoma.

Widess, M., 1973, How thin is a thin bed: Geophysics, **38**, 1176-1180.

APPENDIX B

Comparison of frequency attributes from CWT and MPD spectral decompositions of a complex turbidite channel model

Charles I. Puryear, Shenghong Tai, and John P. Castagna*
Department of Geosciences , University of Houston
Ron Masters and Fa Dwan
Shell International Exploration and Production Company

Summary

Various studies have demonstrated the usefulness of spectral decomposition and its associated frequency attributes in seismic interpretation and hydrocarbon exploration. However, many different techniques for spectral decomposition exist in the petroleum industry, creating a need for comparative studies of these techniques to evaluate their utility. In this work, we compare the results of the application of the CWT and MPD algorithms and associated frequency attributes to a complex turbidite model. Our results indicate that better resolution of stratigraphic features is achieved by the MPD algorithm. These improvements include sharper definition of lateral stratigraphic changes and detection of subtle channel features associated with off-peak frequencies. We also show the effective extraction of stratigraphic features associated with off-peak frequencies achieved by principal component analysis. We believe a quantitative assessment of the relationship between the rock properties volume and frequency attributes will provide useful insight during future work.

Introduction

Spectral decomposition is a seismic analysis technique that decomposes seismic data into the time-frequency domain, which often contains useful information for layer thickness estimation (Partyka et al.,1999; Puryear and Castagna, 2008), stratigraphic interpretation (Marfurt and Kirlin, 2001; Puryear and Castagna, 2008), and hydrocarbon indication (Castagna et al., 2003; Sinha et al., 2005). There are many spectral decomposition algorithms and frequency attributes that can be generated from spectral decomposition volumes. In this paper, we compare results obtained from two common spectral decomposition algorithms – the Continuous Wavelet Transform (CWT) and Matching Pursuit Decomposition (MPD). Because of the large volume of data produced by the spectral decomposition process, the general objective of frequency attributes applied to spectral decomposition is to reduce the quantity of cumbersome frequency volumes to a manageable number while retaining the most geologically pertinent information contained within the redundant frequency volumes. Common frequency attributes include peak frequency/peak amplitude mapping (Marfurt and Kirlin, 2001) and principal component analysis of spectral components (Guo et al., 2006). Our objective is to compare both the spectral decomposition results generated by the CWT and MPD and the frequency attributes derived from those results. We apply the algorithms to synthetic data generated by the application of the 3D “Huygens” method to a complex turbidite rock properties model (van Hoek and Salomon, 2006).

Theory and Method

The CWT is a commonly used wavelet transform that utilizes orthogonal basis wavelets in order to decompose the seismic trace into individual frequency components. The CWT is essentially equivalent to a narrow-band filtering of the data in the temporal domain. We apply CWT to seismic traces using a Morlet wavelet basis function, which utilizes a window that varies as a function of frequency. MPD is a technique for time-frequency analysis that utilizes non-orthogonal basis functions, thereby allowing for atoms with more time compactness and more flexibility in the selection of atoms that match the shape of the trace. We compare the results from the spectral decompositions directly and then use these results as input into peak frequency/peak amplitude mapping and principal components mapping for comparison. Peak frequency/peak amplitude mapping tracks the frequency with the highest amplitude and the amplitude at that frequency along a particular horizon. Peak frequency is strongly related to layer thickness below tuning. Peak amplitude is highly correlated to broadband amplitude, and is therefore a less useful frequency attribute (Blumentritt, 2008). Hence, we focus on peak frequency for comparison between the CWT and MPD. We also perform a principal component analysis of the spectral components in order to isolate frequency bands representative of the data for comparison between the CWT and MPD. We compare the data using identical plotting ranges relative to the standard deviation of the data. We note that the single frequency

components, the peak frequency, and the principal components all highlight subtle channel features that respond preferentially to narrow frequency ranges.

Examples

Van Hoek and Salomons (2006) generated the synthetic seismic data using Kirchoff demigration, or ray tracing, followed by standard processing and migration. Figure B1 shows the spectrum of the seismic wavelet, with a peak frequency of approximately 16 Hz. Figure B2a shows a vertical slice through the impedance model volume with prominent channel belts at the depth range of interest circled, Figure B2b shows the synthetic seismic data and analysis horizon used in subsequent figures, and Figure B2c shows the line of section through a broadband amplitude extraction map.

We illustrate the results of the spectral decomposition algorithms and frequency attributes using several examples. In order to better understand the information content of the principal components, we plot the spectral energy distribution of the first 5 principal components of the spectral components. The peak energy of each increasing component number gravitates toward lower frequencies. We speculate that this tendency is related to the fact that there is more variation in wavelength scale relative to a given feature in the low end of the spectrum than in the high end (i.e. a given quantity of frequency change is more significant in the low end of the spectrum than in the high end of the spectrum). Figure B4 shows a comparison of the 2nd principal components, which are correlated to spectral components of approximately 9 Hz, computed from the CWT and MPD spectral components; the plots are scaled to ± 4

standard deviations. The images show similar channel geometries, both highlighting a channel that is not prominent in the broadband amplitude extraction (Figure B2c) or the 1st principal component extractions. However, the 2nd principal component extracted from the MPD result shows sharper delineation of lateral stratigraphic changes, as indicated by block arrows. Figure B5 illustrates the difference between 5 Hz spectral component maps, also scaled to ± 4 standard deviations, obtained from the CWT and MPD. The low frequency MPD result isolates a channel meander loop that is not highlighted by any of the CWT frequency components, while the 5 Hz CWT component highlights the same channels that are highlighted by both methods at higher frequencies (see Figures B2c and B3). We believe this discrepancy can be attributed to the long cross-correlation window used by the CWT at low frequencies, which fails to isolate temporally-restricted low-frequency energy. Figure B6 compares peak frequency extractions from the CWT and MPD spectral components. The result obtained from the MPD spectral components displays greater continuity and delineation of the low frequency channel highlighted in Figure B5 than that obtained from the CWT spectral components.

Conclusions

We have compared spectral components and frequency attributes from the CWT and MPD spectral decomposition algorithms applied to a synthetic seismic model of a complex turbidite rock properties model volume. Our results indicate that MPD yields higher resolution of stratigraphic detail than does the CWT in two ways. First, lateral

stratigraphic changes appear sharper on the MPD sections, indicative of less energy smoothing in the time domain. Second, low frequency features with limited temporal extent are effectively isolated on MPD, yet averaged out by the CWT due to the variable window smoothing effect. We note that principal component sections beyond the 1st principal component effectively isolate stratigraphic features that are difficult to distinguish on broadband amplitude extractions. It is our expectation that in more complex geological scenarios, principal component analysis will separate intermingled stratigraphic features into "classes" based on optimal spectral response. In future work, we intend to quantitatively link the rock properties model to the responses of frequency attributes and investigate the implications of those attributes for understanding depositional systems.

Acknowledgements

We would like to thank Shell International Exploration and Production for permission to publish the data.

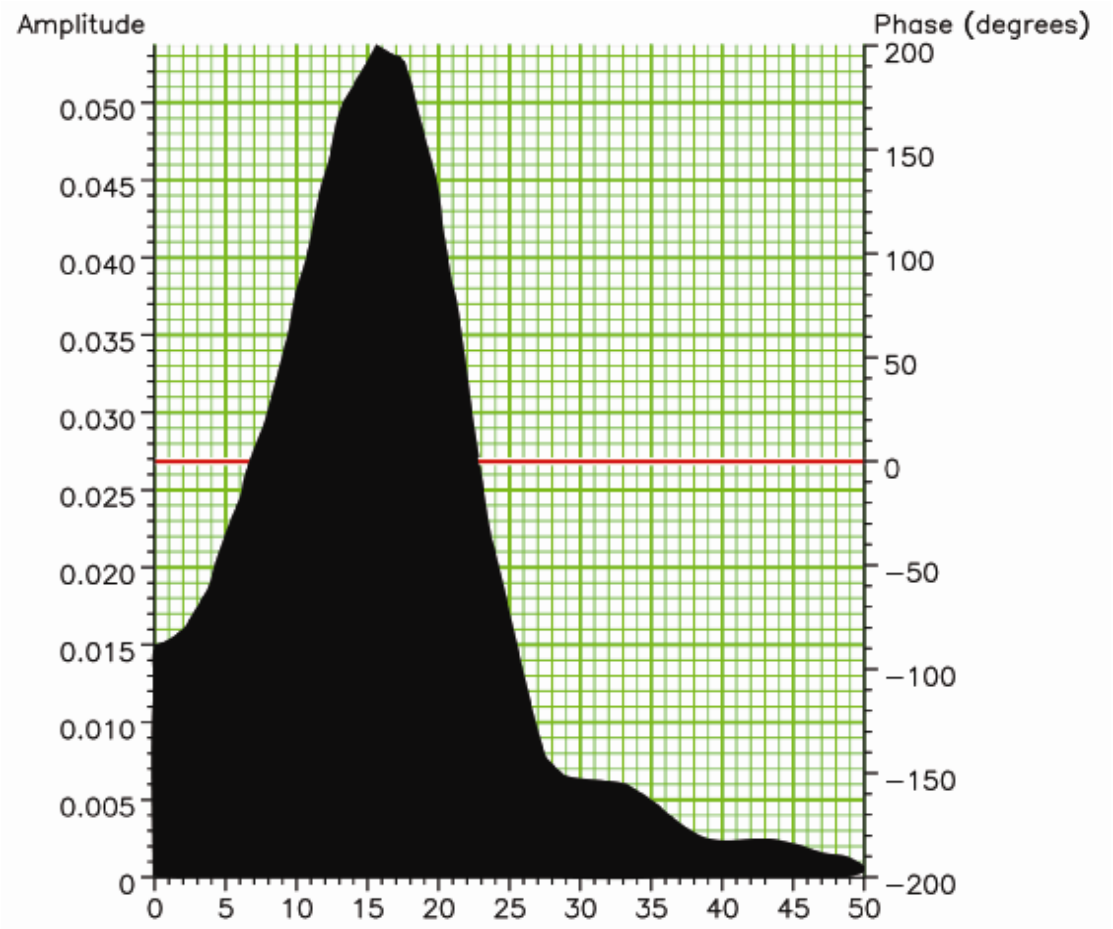

Figure B1. The spectrum of the synthetic seismic wavelet. The peak frequency is about 16 Hz.

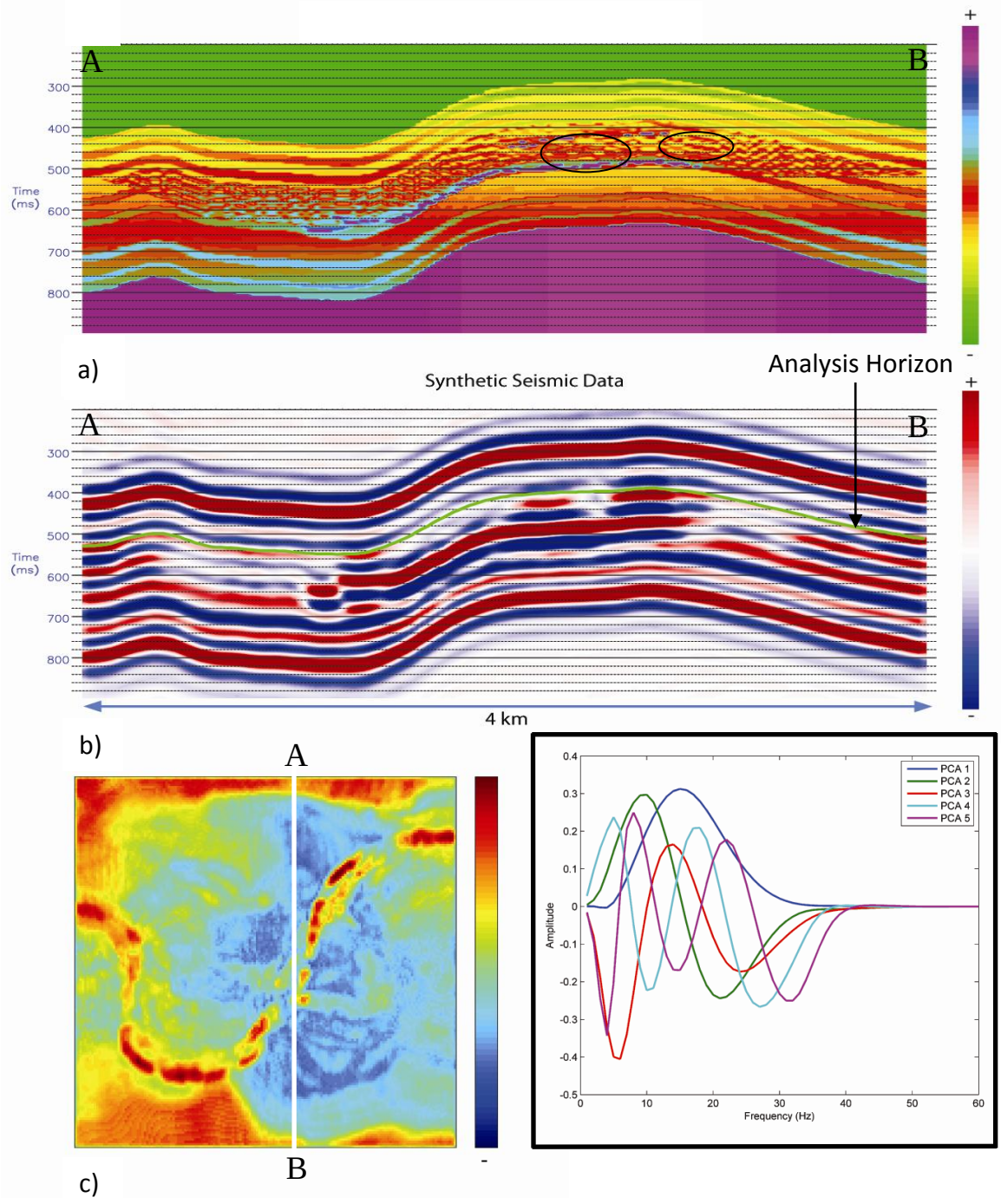

Figure B2. (a) Impedance model with channel belts circled, (b) synthetic seismic model and horizon (green), and (c) horizon amplitude extraction.

Figure B3. Principal component spectra. Peak spectral energy gravitates toward lower frequencies with increasing component number.

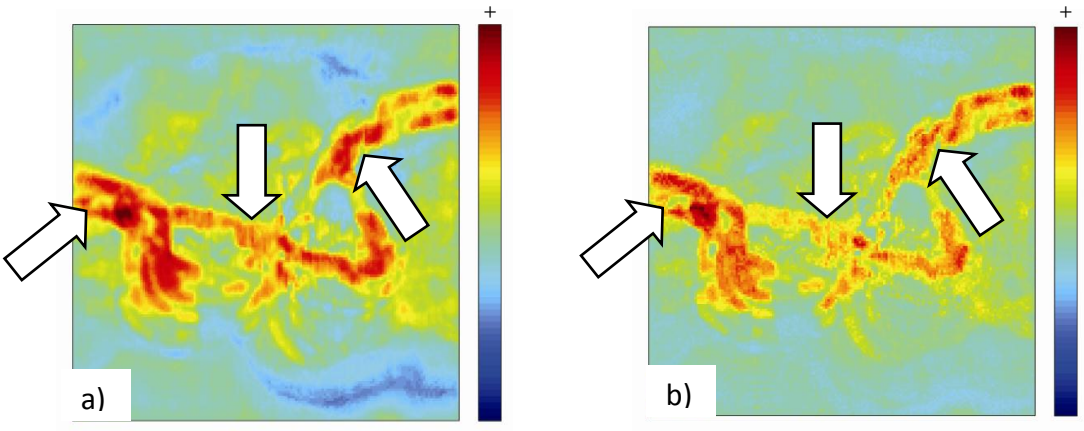

Figure B4. Comparison of the 2nd principal component derived from (a) CWT and (b) MPD spectral components. Arrows indicate improved resolution by MPD.

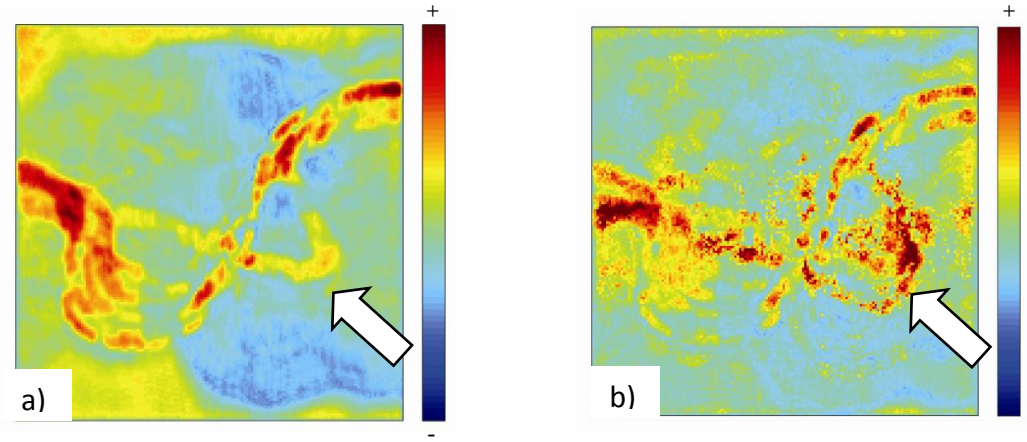

Figure B5. Comparison of 5 Hz spectral components from (a) CWT and (b) MPD. Block arrows indicate a meander loop that is highlighted by MPD but not CWT.

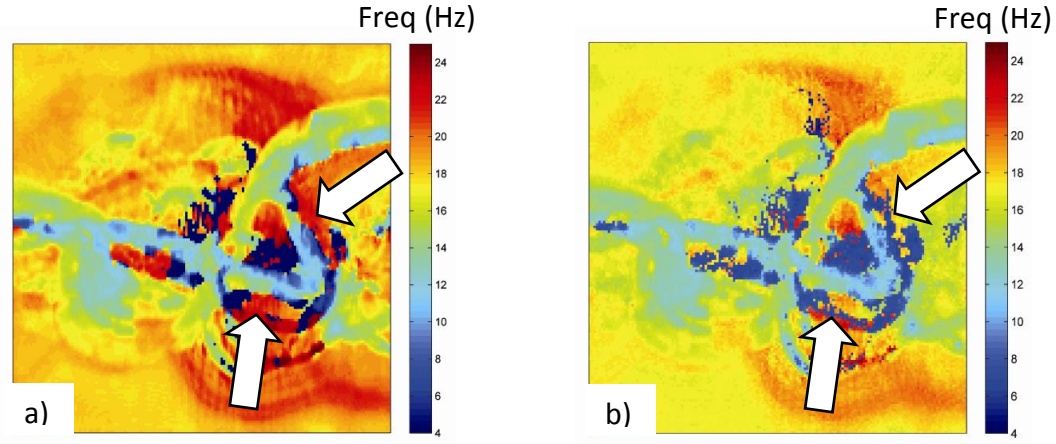

Figure B6. Comparison of peak frequency horizons extracted from (a) CWT and (b) MPD components. Arrows indicate a meander seen more distinctly on MPD.

References

Blumentritt, C.H., 2008, Highlight volumes: reducing the burden of interpreting spectral decomposition data: The Leading Edge, **27**, 330-333.

Castagna, J. P., S. Sun, and R. W. Siegfried, 2003, Instantaneous spectral analysis: Detection of low-frequency shadows associated with hydrocarbons: The Leading Edge, **22**, 120–127.

Marfurt, K. J., and R. L. Kirlin, 2001, Narrow-band spectral analysis and thin-bed tuning: Geophysics, **66**, 1274–1283.

Partyka, G. A., J. A. Gridley, and J. A. Lopez, 1999, Interpretational aspects of spectral decomposition in reservoir characterization: The Leading Edge, **18**, 353–360.

Puryear, C.I. and J.P. Castagna, 2008, Layer thickness determination and stratigraphic interpretation using spectral inversion: Theory and application: Geophysics, **73**, R37-R48.

Sinha,S., Routh, P.S., Anno, P.D., and Castagna, J.P., 2005, Spectral decomposition of seismic data with continuous-wavelet transforms, Geophysics, **70**, 19-25.

Van Hoek, T. and B. Salomons, 2006, Understanding the seismic expression of complex turbidite reservoirs through synthetic seismic forward modeling: 1D convolutional versus 3D modeling approaches: 26th Annual Gulf Coast Section SEPM Foundation Bob F. Perkins Research Conference, 345-372.

APPENDIX C
MODEL NOISE TESTS

In order to assess the robustness of CLSSA to noise, we compile a series of tests involving different types of noise added to the signal shown in Figures 19c and 20c. In Figures C1 and C2, we add Gaussian noise with an L2 norm equal to .1 times the L2 norm of the signal. The CLSSA (Ni=1, α_F=.001) results are shown for the signal, the noise, and the summation of the signal and noise. The algorithm is stable in the presence of Gaussian noise. We further test the algorithm by adding a series of simulated noise bursts in the time domain (Figures C3 and C4). Streaking noise associated with the time domain expression of the noise (Figures C3b and C4b) is observed in the CLSSA transformation (Figures C3f and C4f) of the time-domain superposition of the data and noise bursts (Figures C3c and C4c). However, the frequency characteristics of the signal are captured, again demonstrating stability. Finally, in Figures C5 and C6, we add preshot gather noise with an L2 norm scaled to .1 times the signal L2 norm. Again, the noise manifests in the results but does not destabilize the algorithm.

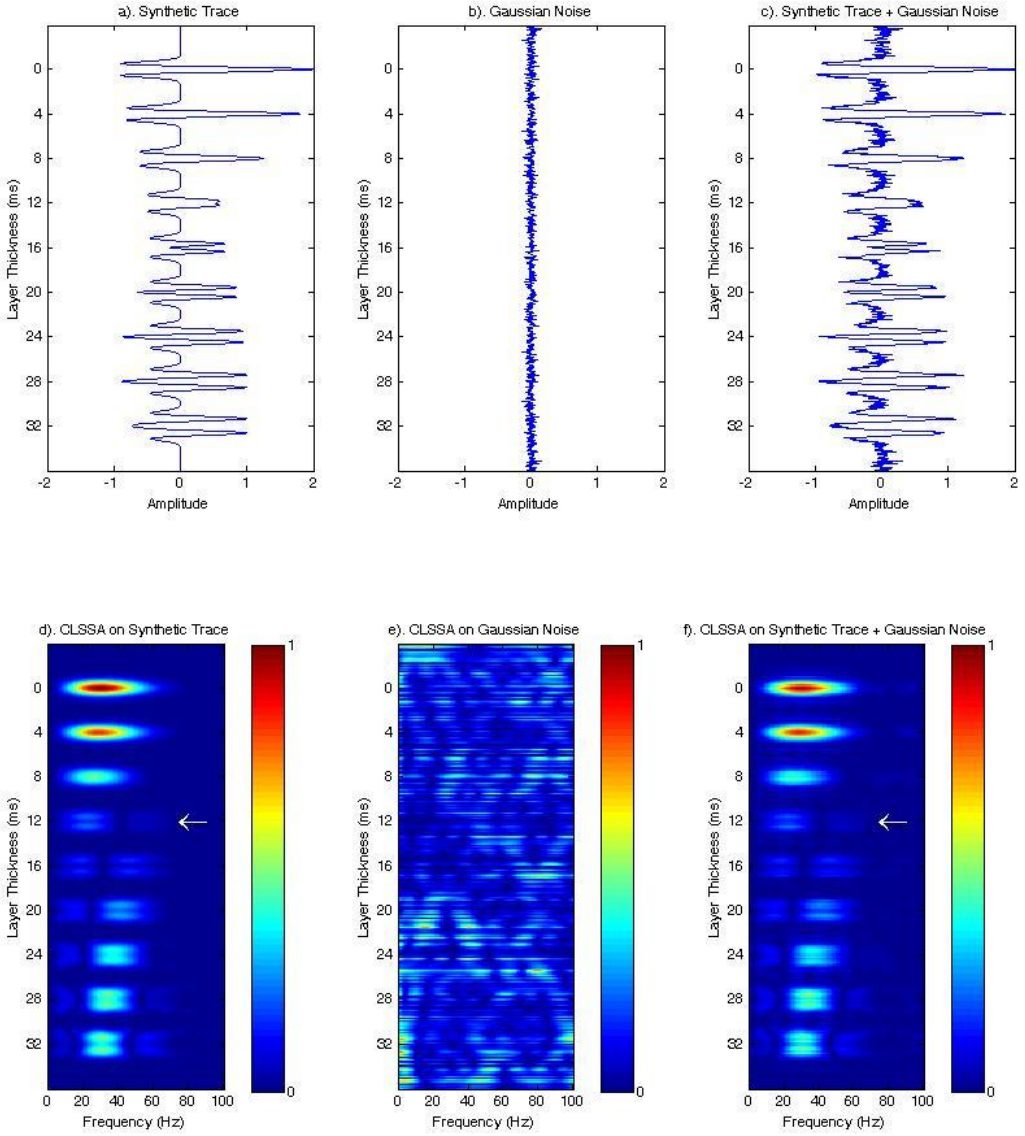

Figure C1). Even dipole pair synthetic reflectivity model with increasing thickness as a function of time (see Figure 19). In order to demonstrate robustness in the presence of noise, we added Gaussian noise having an L2-norm equal to .1 times the L2-norm of the signal. Plots show: (a) the signal, (b) Gaussian noise, (c) summation of signal and Gaussian noise, (d) the spectral decomposition of (a), (e) the spectral decomposition of (b), and (f) the spectral decomposition of (c).

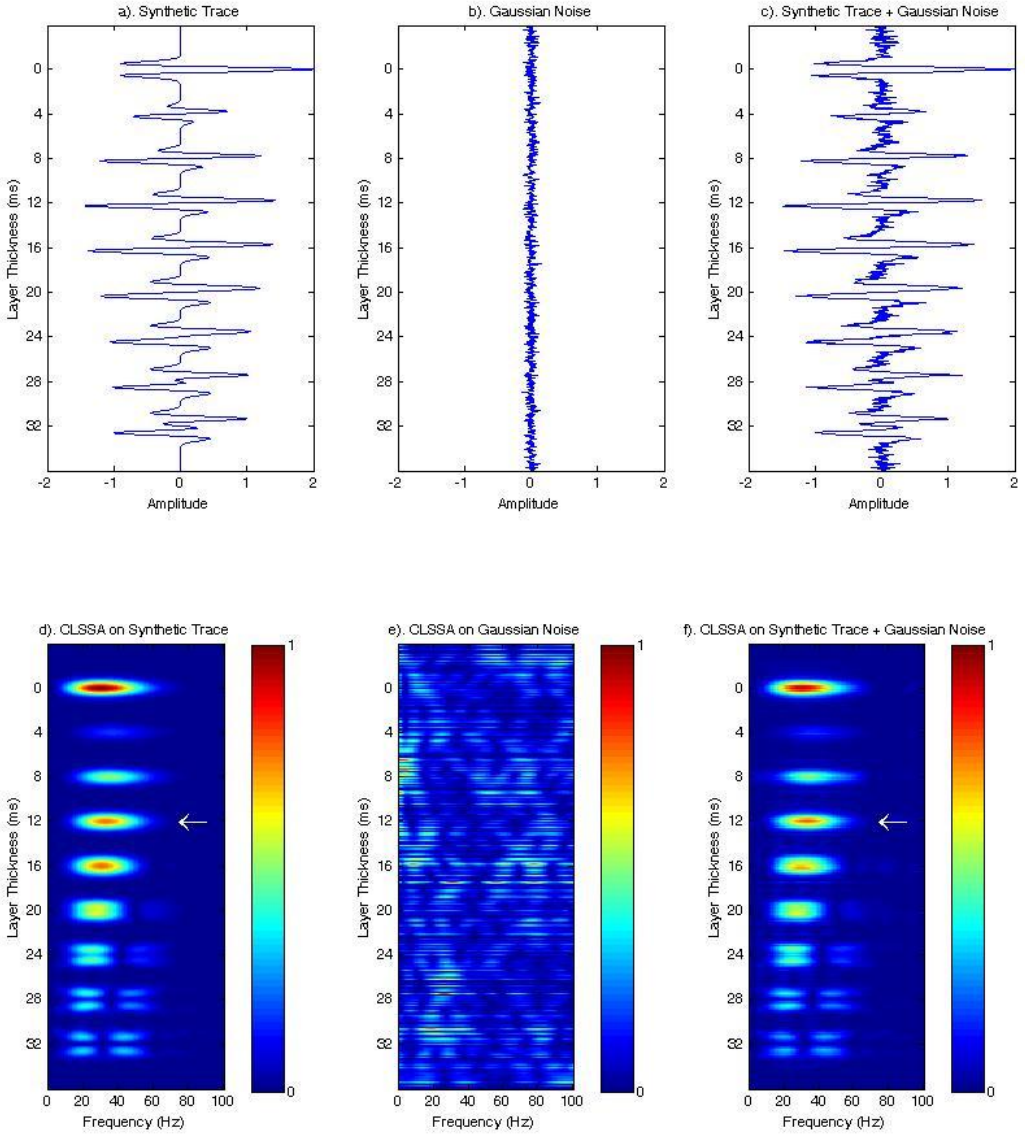

Figure C2). Odd dipole pair synthetic reflectivity model with increasing thickness as a function of time (see Figure 19). In order to demonstrate robustness in the presence of noise, we added Gaussian noise having an L2-norm equal to .1 times the L2-norm of the signal. Plots show: (a) the signal, (b) Gaussian noise, (c) summation of signal and Gaussian noise, (d) the spectral decomposition of (a), (e) the spectral decomposition of (b), and (f) the spectral decomposition of (c).

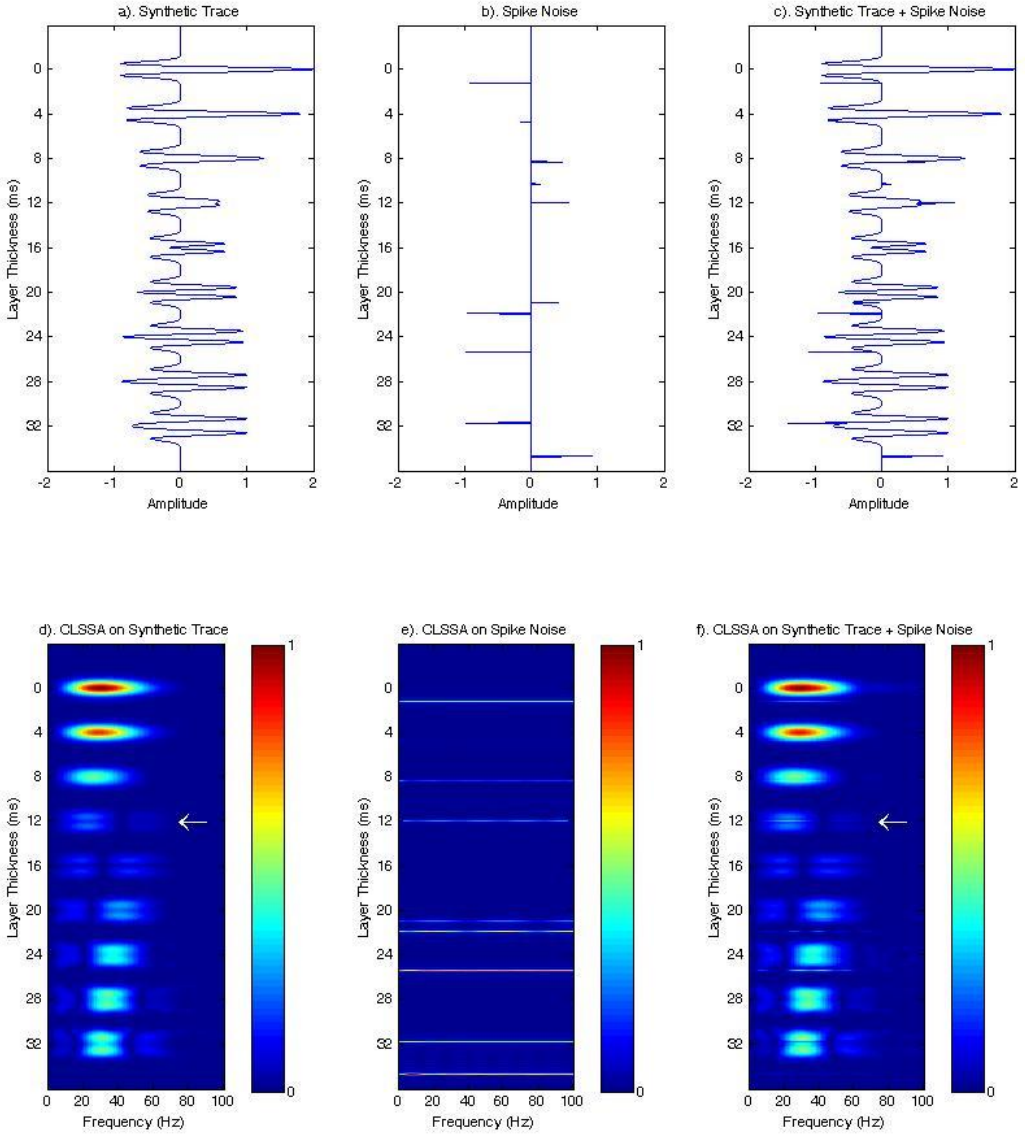

Figure C3). Even dipole pair synthetic reflectivity model with increasing thickness as a function of time (see Figure 19). In order to demonstrate robustness in the presence of noise, we added a series of noise bursts to the signal. Plots show: (a) the signal, (b) noise burst series, (c) summation of signal and Gaussian noise, (d) the spectral decomposition of (a), (e) the spectral decomposition of (b), and (f) the spectral decomposition of (c).

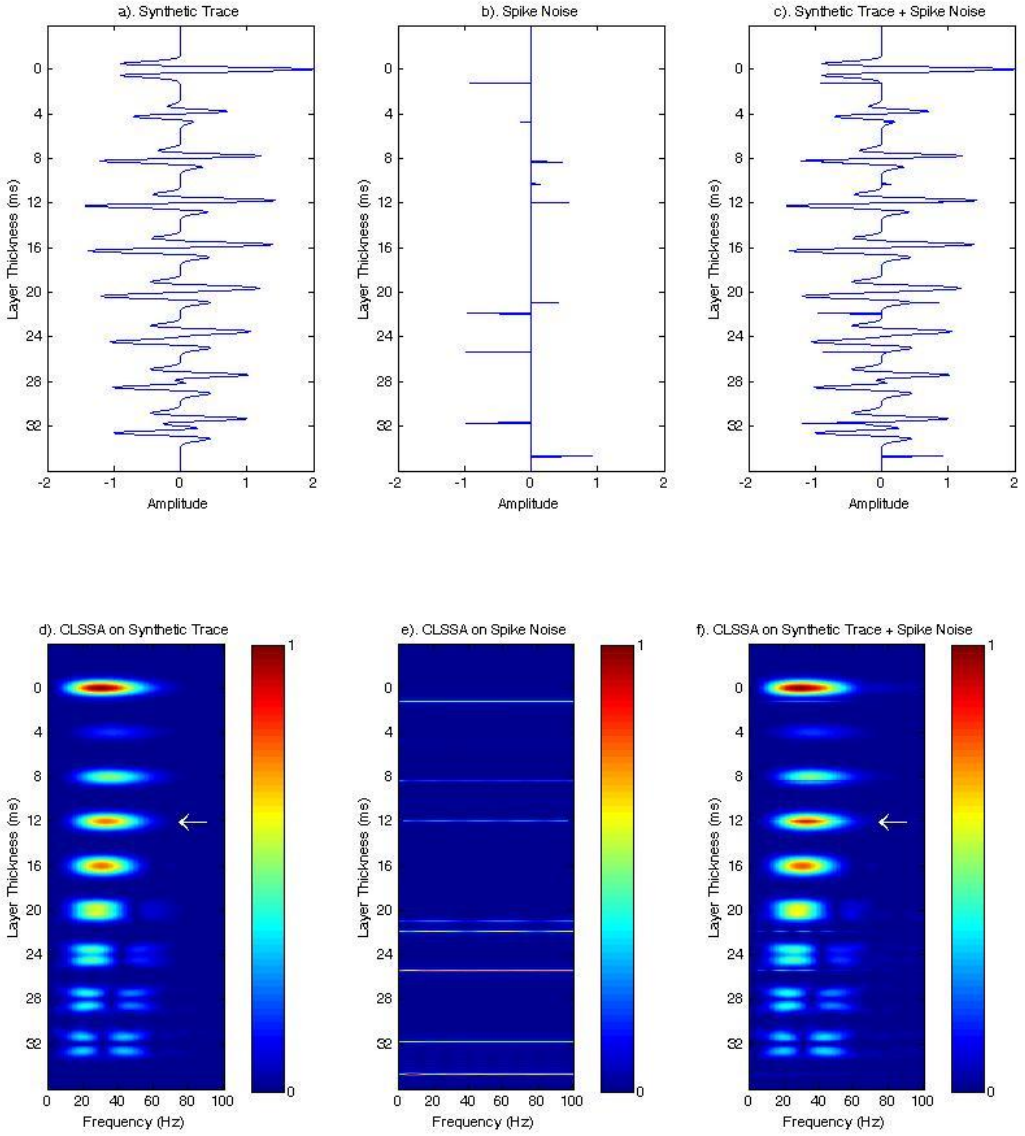

Figure C4). Odd dipole pair synthetic reflectivity model with increasing thickness as a function of time (see Figure 20). In order to demonstrate robustness in the presence of noise, we added a series of noise bursts to the signal. Plots show: (a) the signal, (b) noise burst series, (c) summation of signal and Gaussian noise, (d) the spectral decomposition of (a), (e) the spectral decomposition of (b), and (f) the spectral decomposition of (c).

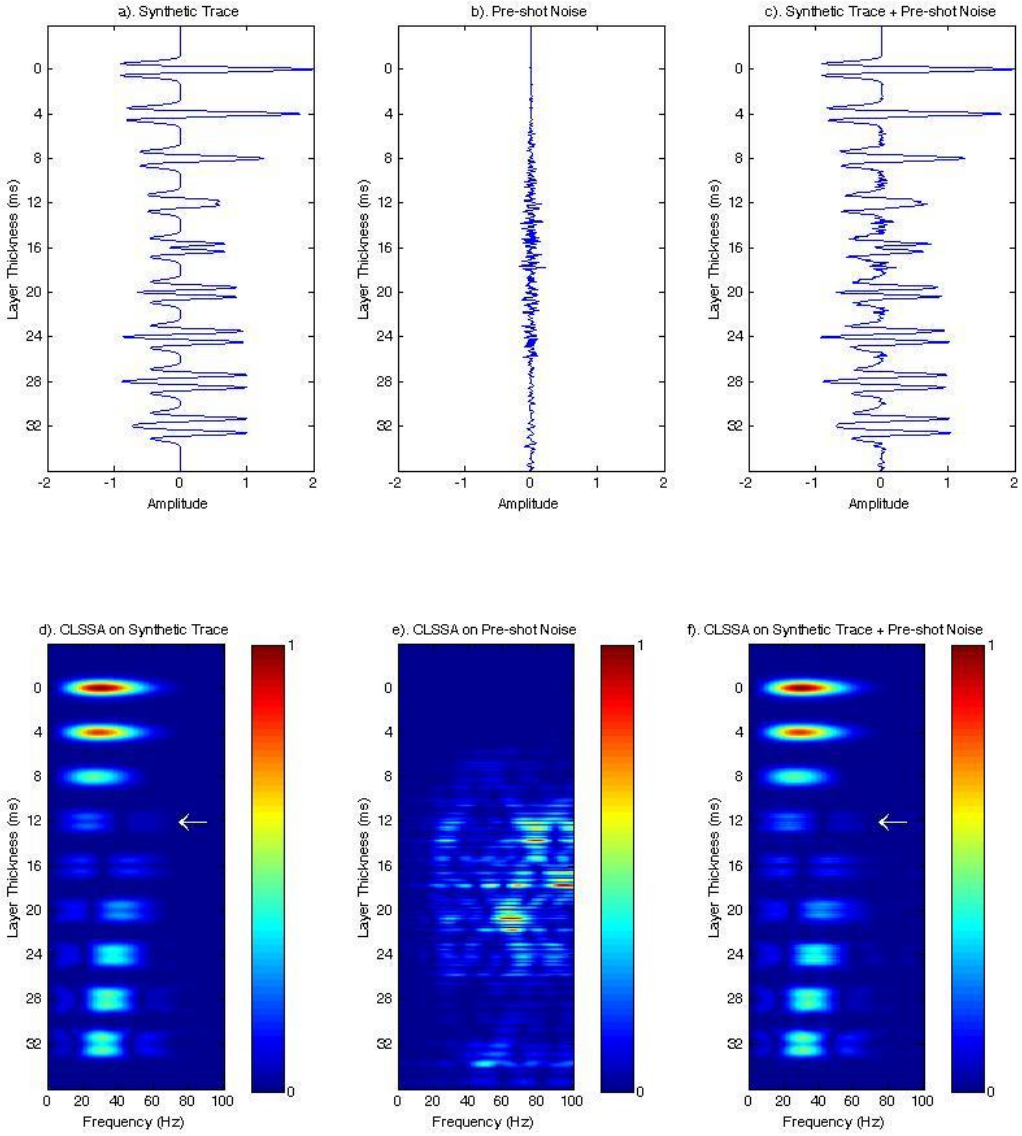

Figure C5). Even dipole pair synthetic reflectivity model with increasing thickness as a function of time (see Figure 19). In order to demonstrate robustness in the presence of noise, we added preshot gather noise from real data to the signal. Plots show: (a) the signal, (b) preshot gather noise, (c) summation of signal and Gaussian noise, (d) the spectral decomposition of (a), (e) the spectral decomposition of (b), and (f) the spectral decomposition of (c).

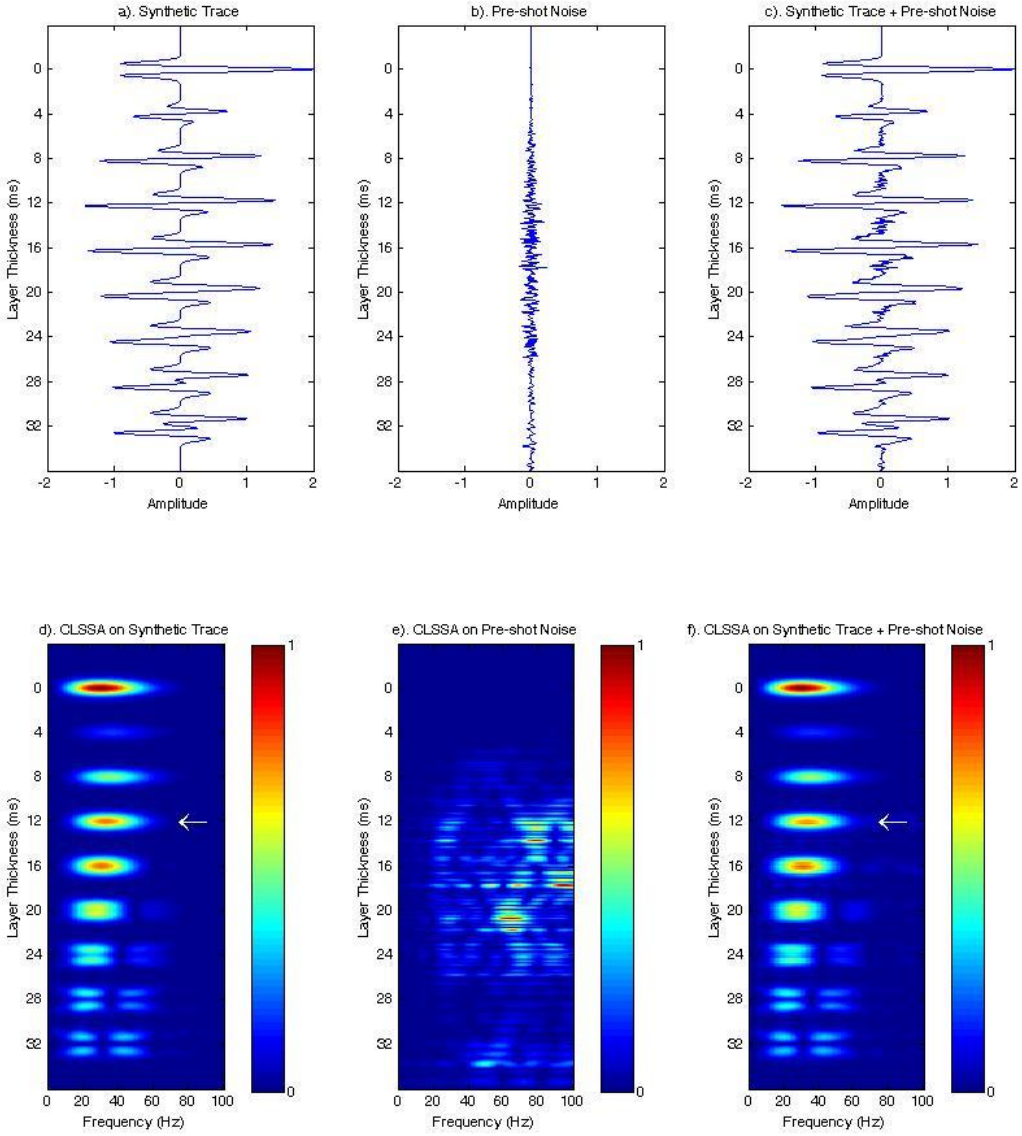

Figure C6). Odd dipole pair synthetic reflectivity model with increasing thickness as a function of time (see Figure 20). In order to demonstrate robustness in the presence of noise, we added preshot gather noise from real data to the signal. Plots show: (a) the signal, (b) preshot gather noise, (c) summation of signal and Gaussian noise, (d) the spectral decomposition of (a), (e) the spectral decomposition of (b), and (f) the spectral decomposition of (c).

APPENDIX D
MATLAB CODE TO PRODUCE FIGURE 19 c and f and 20 c and f

```
%APPENDIX D
%CODE TO PRODUCE FIGURES 19c and 19f

clear all
close all

[Nt,f,dt]=deal(1001,30,1);
ref=zeros(Nt,1);
c=(1:9)*100;
T=(0:8)*2;
ref([c+T c-T])=1;
ref(100)=2;
t=dt*((1:Nt)-ceil(Nt/2))';
x=-(pi*f*t*1e-3).^2;
dr=conv2(ref,(1+2*x).*exp(x),'same');
fhz=1:120;
Nwms=100;
nw2=ceil(Nwms/(2*dt));

s=fft(dr,[],1);
N=size(s,1);
N2=floor(N/2);
s(1:N2,:)=-1i*s(1:N2,:);
s(N2+1:end,:)=1i*s(N2+1:end,:);
d=dr-1i*real(ifft(s,[],1));

tt=dt*(-nw2:nw2)'*1e-3;
Wd=diag((1+cos(pi*(-nw2:nw2)/nw2))/2);
Fw=Wd*(cos(2*pi*tt*fhz)+1i*sin(2*pi*tt*fhz));
G=Fw*Fw';
G=G+eye(size(G))*max(diag(G))*0.001;
d0=flipud(conv2(eye(nw2*2+1),d)');
d0=Wd*d0(:,nw2+1:end-nw2)*diag(abs(d));
m1=(Fw'*(G\d0)).';

subplot(1,2,1);
plot(dr,t); title('Trace');
set(gca,'Ydir','reverse');
subplot(1,2,2);
imagesc(fhz,t,abs(m1));
title('CLSSA panel');
xlabel('Frequency, Hz');
ylabel('Time, ms');
```

```
APPENDIX D
%CODE TO PRODUCE FIGURES 20c and 20f

clear all
close all

[Nt,f,dt]=deal(1001,30,1);
ref=zeros(Nt,1);
c=(1:9)*100;
T=(0:8)*2;
ref([c-T])=1;
ref([c+T])=-1;
ref(100)=0;
t=dt*((1:Nt)-ceil(Nt/2))';
x=-(pi*f*t*1e-3).^2;
dr=conv2(ref,(1+2*x).*exp(x),'same');
fhz=1:100;
Nwms=100;
nw2=ceil(Nwms/(2*dt));

s=fft(dr,[],1);
N=size(s,1);
N2=floor(N/2);
s(1:N2,:)=-1i*s(1:N2,:);
s(N2+1:end,:)=1i*s(N2+1:end,:);
d=dr-1i*real(ifft(s,[],1));

tt=dt*(-nw2:nw2)'*1e-3;
Wd=diag((1+cos(pi*(-nw2:nw2)/nw2))/2);
Fw=Wd*(cos(2*pi*tt*fhz)+1i*sin(2*pi*tt*fhz));
G=Fw*Fw';
G=G+eye(size(G))*max(diag(G))*0.001;
d0=flipud(conv2(eye(nw2*2+1),d)');
d0=Wd*d0(:,nw2+1:end-nw2)*diag(abs(d));
m1=(Fw'*(G\d0)).';

subplot(1,2,1);
plot(dr,t); title('Trace');
xlim([-1.5 1.5]);
set(gca,'Ydir','reverse');
subplot(1,2,2);
imagesc(fhz,t,abs(m1));
title('CLSSA panel');
xlabel('Frequency, Hz');
ylabel('Time, ms');
```